Journal of Materials Chemistry A

REVIEW

View Article Online
View Journal | View Issue

Cite this: J. Mater. Chem. A, 2022, 10, 13589

The versatility of the dynamic hydrogen bubble template derived copper foam on the emerging energy applications: progress and future prospects

Manisha Das,† Ashmita Biswas,† Taniya Purkait,† Tribani Boruah,† Sakshi Bhardwaj, Sabuj Kanti Das and Ramendra Sundar Dey *

Received 18th February 2022
Accepted 31st May 2022

DOI: 10.1039/d2ta01355j

rsc.li/materials-a

The current review was conceptualised after realising the industrial relevance and enormous potential of nanostructured copper foams (Cuf) in the field of energy applications, as active electrode components, as a building block or even just as a dynamic current collector. Among the plethora of chemical and electrochemical synthesis approaches explored so far, the dynamic hydrogen bubble template (DHBT) technique has emerged as a promising, economical, and effective means of producing macroporous Cuf with nanostructured pore walls, integrated electrical conductivity and, most importantly, extensively accessible surface area. While a comprehensive repository on the versatility of the DHBT technique and its exploration in developing various monometallic or bimetallic films exists, very little attention has been paid to highlighting Cuf as an ambidextrous nanometal foam (NFM) model that has a potentially broad spectrum of applicability in all fields of energy applications, including energy storage and electrocatalysis. Herein, we review the current state of the art approaches on the synthesis of DHBT-derived Cuf and its suitable applications in various energy devices. We also highlight the technological bottleneck of realising the theoretical competence of DHBT-derived Cuf in a commercial setup, and attempt to address the issues for future relevance.

1. Introduction

Presenting a secure and sustainable portal of clean energy for future generations is one of the most difficult scientific and societal challenges of recent times.[17] The ever-growing fixation

Institute of Nano Science and Technology (INST), Sector-81, Mohali-140306, Punjab, India. E-mail: rsdey@inst.ac.in

† These authors contributed equally.

Manisha Das is currently pursuing her PhD in nanoscience and nanotechnology at the Institute of Nano Science and Technology (INST), Mohali, India. She completed her B. Tech degree in Electronics and Communication Engineering in 2013 from Sam Higginbottom University of Agriculture, Technology & Sciences (SHUATS), Allahabad, India, and M. Tech in Material Science and Nanotechnology from the National Institute of Technology (NIT), Kurukshetra, India in 2017. She has published two first-author articles and nine other publications in peer-reviewed journals and a book, 'Carbonaceous Material and Future Energy'. Her areas of interest are nanomaterials synthesis and electrocatalysis for energy generation and conversion.

Ashmita Biswas received her Bachelor's degree in Chemistry with Honours from the University of Calcutta in 2017. She completed her Master's degree from the Indian Institute of Engineering Science and Technology, Shibpur, India (2017–2019). She is currently pursuing her PhD under the supervision of Dr Ramendra Sundar Dey at the Institute of Nano Science and Technology, Mohali, India and the Indian Institute of Science Education and Research, Mohali, India. She has published five research papers in peer-reviewed journals and provisionally filed one patent. Her research interests include the development of noble-metal-free catalysts applicable for electrocatalytic reduction reactions in the field of sustainable energy.

with numerous electronic devices in our daily life has resulted in worldwide energy constraints due to the heavy exponential decay of the fossil fuel reserves.[22–25] Additionally, the potential environmental threats posed by greenhouse gas emissions associated with fossil fuel burning have forced us to adopt alternative and eco-friendly energy resources, such as solar, wind or tidal energies.[22–24] However, due to the intermittent nature of these sources, electrochemical energy storage and the generation and conversion of energy technologies have become inevitable and propelled scientists to look for abundant, low-cost yet high-performance electrode materials to be used in such systems.[25,30–42] Luckily, recent advancements in nanotechnology have emerged as a boon in the exploration of various noble electrode materials that can offer an effective and feasible solution towards the current energy crisis scenario.[34,44–48] Nanostructured materials are often known for their high active surface area, shape-selective effects and remarkable surface properties that are crucial for any electrochemical process.[50–55] The development of well-integrated hierarchical porous structures, such as porous foams has immensely influenced the direction of electrochemical energy research with the help of their opulent beneficial physical features that facilitate fast surface reaction kinetics due to rapid charge transfer between the open-pore hierarchical morphology, which in turns enhances the ionic as well as electronic conductivity.[56–60] Remarkable examples include ultraporous carbon electrodes and graphene aerogels, which are the sole commercial electrode materials in the supercapacitor industry.[62–64] Another leading instance of porous networks in material science is mesoscopically ordered materials, such as brightly coloured crystalline colloidal arrays of intelligent polymer hydrogel films with switchable periodicity and diffraction patterns that have huge application potential in sensors or supercapacitors.[65–67] However, the wettability of these hydrophobic electrodes in electrolytic solutions can be significantly improved by replacing them with high surface area porous metals that are not only more electrically conducting,[68] but also enhance the energy densities of the supercapacitors.[69–71] Interestingly, nanoporous

Tribani Boruah is currently pursuing her PhD at the Institute of Nano Science and Technology (INST), Mohali, India under the supervision of Dr Ramendra Sundar Dey. She has received her B.Sc. degree in Chemistry from Dibrugarh University, Assam, India in 2016 and completed her Master's degree in Organic Chemistry at the University of Delhi, New Delhi, India in the year 2019. Her current research interest includes the synthesis of non-precious metal-based air electrodes for rechargeable metal–air batteries.

Sakshi Bhardwaj is currently a PhD candidate under the supervision of Dr Ramendra Sudar Dey at the Institute of Nano Science and Technology (INST), Mohali, India and the Indian Institute of Science Education and Research, Mohali, India. She received her Master's degree in Chemistry from Guru Nanak Dev University, India in 2018. Her current research focuses on the engineering of defect sites of carbonaceous nanomaterials for electrocatalytic applications.

Dr Taniya Purkait completed her PhD in January 2021 under the supervision of Dr Ramendra Sundar Dey from the Institute of Nanoscience Science and Technology (INST), Mohali, India and the Centre for Nano Science and Nano Technology (CNSNT), Panjab University, India. She earned her B.Sc. Degree from the University of Calcutta (2012) and M.Sc. Degree from the Indian School of Mines (ISM), Dhanbad (2014). Her current research interests include the synthesis and fabrication of various carbonaceous materials for energy storage and conversion applications. She has published eighteen research articles in peer-reviewed journals and co-authored a book, 'Carbonaceous Materials and Future Energy'.

Dr Sabuj Kanti Das is currently a Research Associate at the Institute of Nano Science and Technology, Mohali, India. He received his PhD degree in Chemistry (2020) from the Indian Association for the Cultivation of Science (IACS) and Jadavpur University, India and completed his M.Sc. degree in Chemistry from the Indian Institute of Technology, Bombay, India. His research mostly encompasses the synthesis of new functionalized porous materials like Covalent Organic Frameworks (COFs), Metal–Organic Frameworks (MOFs), Porous Organic Polymers (POPs) and their applications in the fields of environment, catalysis, energy and biomedical research. He has published 21 research papers in peer-reviewed international journals.

metal foams (NMFs) have been late to develop in comparison with nanoporous foams of other substances, simply due to the unavailability of suitable bottom-up approaches or length-scale-dependant issues usually encountered in top-down syntheses.[57] The three-dimensional (3D) porous architecture of NMFs is an exclusive class of materials that possess fascinating structural advantages for consideration as a superior choice for energy storage devices.[72–76] The interconnected nano-ramified walls present more than 50% porosity, as well as wide distribution of pore sizes and increased surface area, which make them a very interesting host for electrochemical reactions with the easy diffusion of charged species.[77] Porosity also ensures the economical use of materials, especially when noble metals are required and the fine nanometric structures give access to abundant active/defect sites that are crucial in any surface-confined process, like electrocatalysis. The electrochemical approach of NMF synthesis, on the contrary, avoids this difficulty and significantly contributes to the production of scalable, time-saving, economical, as well as reproducible electrode materials, and has potential applications in myriad electrochemical energy systems, such as fuel cells, carbon dioxide reduction, water electrolysis,[78,79] Li-ion batteries, supercapacitors, hydrogen storage, catalysis, gas purification, drug delivery, sensors, *etc.*[80–83] A number of electrochemical approaches are available for NMF synthesis, including the dealloying technique, electrodeposition, dynamic hydrogen bubble template (DHBT) and the anodization process. Potential driven dealloying has been one of the leading electrochemical approaches to NMF synthesis for the past twenty years, following the notable experiments by Erlebacher *et al.*[84] Since there is an increased tendency for the surface diffusivity of the more noble atom after dealloying, it often results in the coarsening of the formed nanoporous structure to minimize the surface energy and makes the resultant 3D porous walls of the NMF architecture vulnerable to collapse outside the electrolytic solution.[85] It also requires the physical removal of the de-alloyed metal from the media, indicating the need for a more facile electrochemical approach for NMF synthesis. Electrochemical anodizing is a passivation technique used to protect the deposited metal with a thin oxide layer from areal corrosion. This method is often attributed to the clogging of the surface pores in NMFs due to non-porous metal oxide coating[86] and therefore, is not suitable for the fast transport kinetics usually required in electrochemical reactions, including charge storage and catalysis. Electrodeposition, on the other hand, is the most convenient and broadly used technique, nowadays, to grow nanostructured metals or metallic films from electrolytic solutions. While electrodeposition can lead to nanostructures of all dimensions including 2D metal films, DHBT,[87] a special type of electrodeposition technique, is particularly useful for producing 3D interconnected metal growth structures, such as dendrites and foams with high specific surface area and increased active sites. The DHBT technique is a very remarkable discovery in terms of an efficient and clean NMF synthesis method because of the following advantages. (1) It allows access to a porous morphology without the need for an external organic or inorganic template. (2) Here, the H_2 bubbles act as a dynamic template to bubble off the growing metal deposits to create macroporous 3D metallic foams in the micron size with nanostructured pore walls, maximising the surface area and, (3) there is an increased number of active sites at the pore walls or the grain boundaries as a direct consequence of both H_2 evolution and the high overpotential employed. Therefore, the DHBT method is the most practiced electrodeposition method for NMF synthesis that is capable of selectively producing the

Dr Ramendra Sundar Dey is a Scientist at the Institute of Nano Science and Technology, Mohali, India. He was a Hans Christian Ørsted postdoc fellow at the Technical University of Denmark (DTU), Denmark. He received his PhD in Chemistry in 2013 from the Indian Institute of Technology (IIT) Kharagpur, India. He is involved in research in the field of electrochemistry of nanomaterials. His research interests focus on the architecture and engineering of nanomaterials for advanced energy storage nano-technology and non-novel metal nanomaterials for electrocatalysis and hybrid energy technology. He has been honoured with several prestigious National and International recognition, such as the INSPIRE Faculty Award in 2015, the Journal of Materials Chemistry An Emerging Investigator under the theme highlighting 2019's rising stars of materials by RSC. Recently he became an Associate of the Indian Academy of Sciences (IASc), Bengaluru and a member of the Indian National Young Academy of Sciences (INYAS).

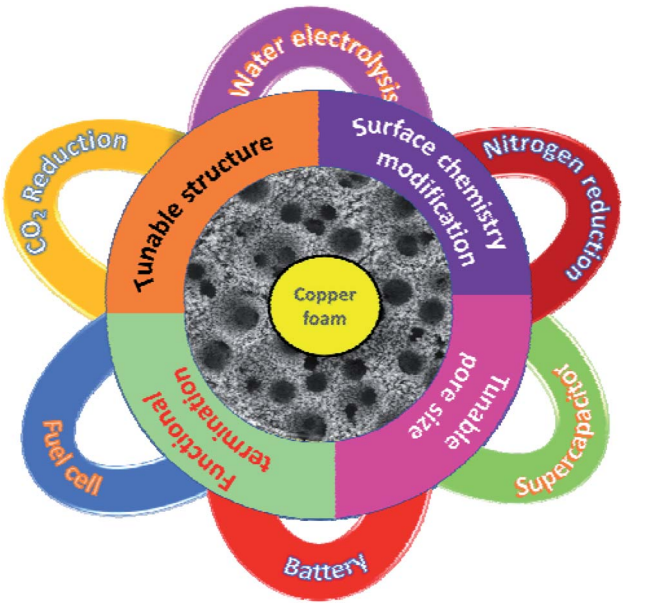

Scheme 1 The remarkable properties of the versatile electrodeposited Cuf in potential green energy applications.

desired shapes and morphologies of the porous foams at the atomic and molecular level, which is usually not afforded by other fabrication methods.[88] The hydrogen gas evolved in DHBT is cleanly removed from the electrode surface, thereby decreasing the possibility of media contamination as well. The highly interconnected porous networks of NMFs have several benefits such as mechanical robustness, lower interfacial barrier resistance with the current collector, the ability to anchor a versatile range of chemical functionalities over the surface and can also work as a template. Most importantly they possess a high effective surface area that provides additional stability to the electrodes during excruciating service hours while allowing for better use of expensive noble metals in a foamy architecture.[89] The unique DHBT method helps in producing a self-supported NMF by working as a negative template and deliberately suppressing the hydrogen evolution reaction[90] to control the dendritic ends, and the pores are size-selective and tunable to prevent the structure to collapse in the electrolyte due to the weight of the sub-branches. Although some earlier reports also suggested the fabrication of quasi-2D metal electrodeposits based on the DHBT method back in the 1960s,[91] more intense research in this particular field was conducted only after the discovery by Marozzi *et al.*[92,93] Using the DHBT model, NFMs of different single metals, such as copper,[94] tin,[95] nickel,[93] silver,[96,97] gold,[98] palladium,[99] platinum,[100] cobalt,[101] *etc.*, along with several bimetallic systems, such as NiCu,[102] PtRu,[103] CuAg,[104] CuAu,[105] AuPd,[106] AgPd, *etc.*, were reported by various research groups for diverse applications. Among the various NMFs, copper foams (Cuf) electrodeposited by DHBT are one of the frontrunners as electrodes for energy applications owing to the abundance, greater electro-migration resistance, lower electrical resistivity, low-cost and versatile nature of the Cu metal.[107–110] Due to a lower hydrogen overvoltage, dendritic Cufs are more synthetically facile and tuneable than any other NMFs. Additionally, the dependence of electrocatalysts on noble-metals (*e.g.*, Pt, Ir and Ru) in the hydrogen evolution reaction (HER)/oxygen evolution reaction (OER)/oxygen reduction reaction (ORR) limits their large-scale commercial applications, facilitating the scope for the use of porous copper in electrocatalysis and even in the energy storage systems as a cost-effective, stable and scalable alternative.[110–112] In earlier studies, copper foil was usually used as the active material, as well as supporting electrodes, exploiting metastable grain boundaries.[113,114] However, the flatness of the traditional foil current collectors reduces the physical and electrical contact area available for (1) adhesion of the electrode materials to and (2) electron transfer with the electrodes.[115] Inspired by the fact that maximum surface area and active sites will easily be accessible to the electrolyte ions on the metastable grain boundaries of a porous structure, researchers later focussed on the utilization of Cuf for electrochemical reactions for better control of reaction pathways and mass transport.[116–119] Scheme 1 reveals the remarkable surface properties of DHBT-derived Cuf that are crucial for their applications in energy systems. Although Bockris *et al.* first explained the mechanism of hydrogen evolution at Cu cathodes in aqueous solutions,[120] the exciting journey of electrodeposited Cuf for a wide variety of applications started only in the early 2000s when Shin *et al.* explained the wonder of DHBT in sculpting highly porous nanoramified deposits of Cu.[94] A roadmap highlighting the historical achievements in the field of Cuf synthesis *via* electrodeposition and its utilization in various energy storage and conversion systems is illustrated in Scheme 2.

The challenge of obtaining the desired feature of the 3D ramified structure of metal and preventing the overgrown branches from collapsing in the electrolyte encouraged us to go for a self-supported nano-ramified metal deposit using the electrochemical deposition technique accompanying hydrogen co-evolution. NMFs and their structural advantages have been well-documented in literature over the past few years, however,

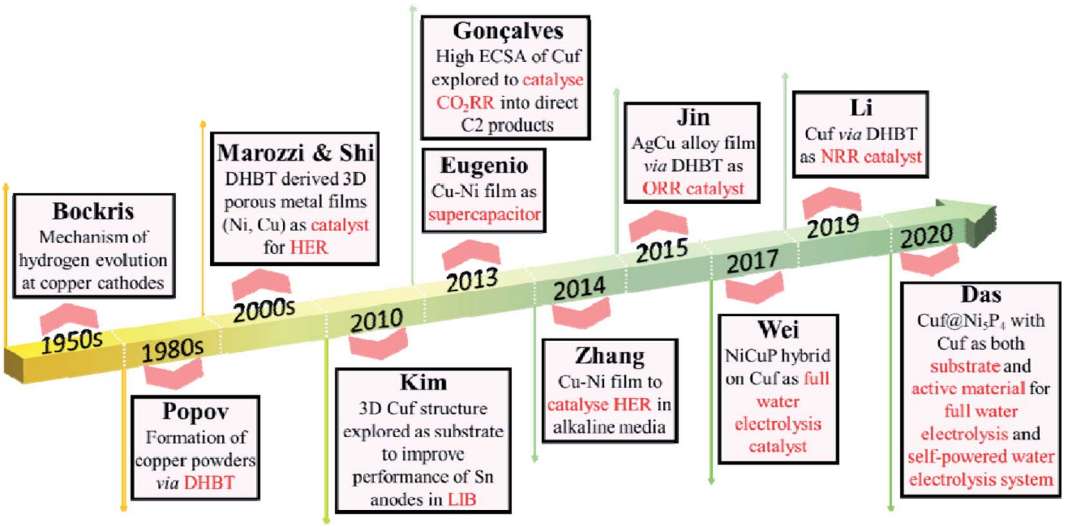

Scheme 2 A roadmap highlighting the history of significant developments in electrodeposited Cuf synthesis and their applications in electrocatalysis and energy storage systems.

the beauty of electrodeposited Cuf as self-supporting electrodes in energy applications is sparsely discussed, which we aim to provide in this review article. Recent significant progress and the rational design of DHBT-derived Cuf as customized electrodes for energy generation, storage and conversion systems over almost two decades, are provided in this review article. The present context highlights the role of Cuf in various aspects of renewable energy systems such as the hydrogen evolution reaction (HER), oxygen evolution reaction (OER), oxygen reduction reaction (ORR), nitrogen reduction reaction (NRR), electrochemical CO_2 reduction and energy storage systems (batteries/supercapacitors). To the best of our knowledge, this review provides overall insights/approaches including synthesis, modification and versatile applications of electrodeposited Cuf. However, the review would not be complete without discussing the various challenges that come with using electrodeposited Cuf as a custom electrode, or even as a substrate for these emerging energy technologies, in practical applications. Additionally, the need to understand the correlation between the growth mechanisms of the dendritic porous nanometric structure with its superior surface properties is also quite critical and has been diligently discussed. Most importantly, the review also presents a future research direction by suggesting possible further developments of the DHBT technique-derived Cuf for the extension to new clean energy applications.

2. Scope of this review

Copper is a 3d transition metal that possesses intriguing physical and chemical characteristics, including a wide range of accessible oxidation states (Cu^0, Cu^I, Cu^{II} and Cu^{III}). Therefore, Cu can easily promote high reactivity *via* both one and two-electron pathways. Since it is an earth-abundant and low-cost material, metallic copper in various forms has received significant attention for several decades.

Fig. 1 highlights various significant physical features of copper metal, which are crucial for its widespread applications. Due to its very high thermal and electrical conductivity, copper is an extremely high-demand material in various fields of application. Mechanically, copper is a soft, malleable and ductile material that has a pinkish-orange colour. Copper, in its nanoform, has significantly varied electrical, mechanical, physical and optical properties as compared to the bulk.[121] Micro- and nano-structures of copper have high electrical conductivity and high melting points, and are corrosion-resistant due to a reduction in the grain size.[122–124]

Electrodeposition *via* the DHBT technique, accompanying the hydrogen bubbling technique, appears to be the most exploitable feature in tailoring the growth of the 3D foamy copper foam (Cuf) architecture with controlled morphology and abundant surface properties in the fabricated nanometric structures. Due to the bubble formation and stirring of the bubble at the electrolyte–electrode interface, the surrounding hydrodynamics fluctuates vehemently, which in turn has a profound impact on the morphology of the nano-ramified structure or the surface properties of the Cuf. It is not our intent to review the DHBT technique in general, as several painstakingly detailed review articles have recorded the recent advances in the literature on this method, highlighting its applicability in the NMF synthesis of all kinds of metals.[87] Since there is almost no convenient assessment of DHBT-derived Cuf as a universal potential system for emerging energy applications, we have attempted to provide a wholesome picture of the current state of the art, especially with a thorough review of contemporary energy applications reported so far in the literature. In a nutshell, the scope of this article is to highlight the structural benefits and potential applicability of as-derived Cuf directed in the energy field. Hierarchically porous structures like DHBT-derived Cuf as active materials, scaffolds or electrocatalysts are fascinating electrode materials for electrochemical energy storage and conversion due to the short transportation

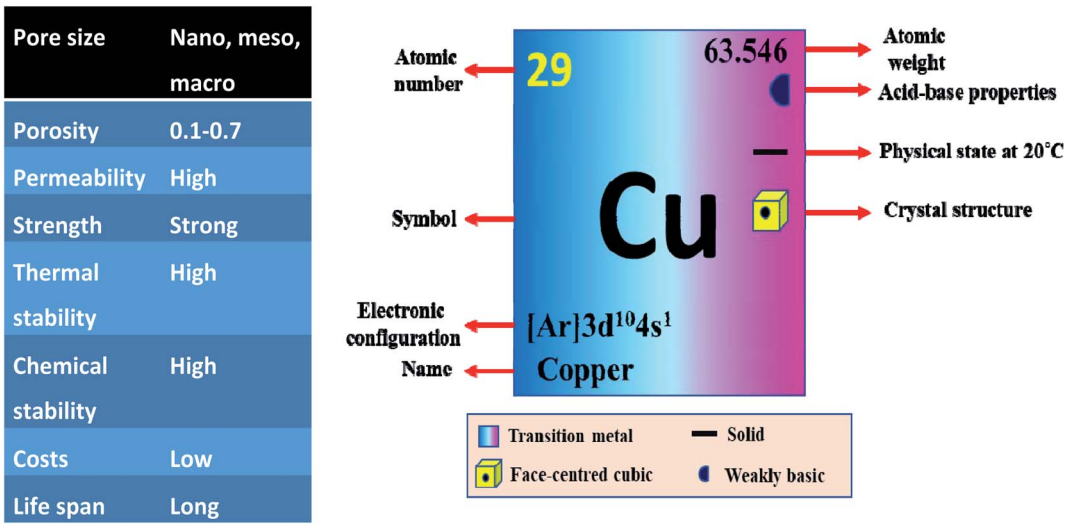

Fig. 1 Characteristic features of copper foam and various significant physical states of Cu.

paths of electrons and ions. It has been already reported that the porous 3D hollow architecture offers plentiful active sites. Since copper has several advantages as a metal in the design of multimetal materials, core–shell nanostructures, co-doping *etc.*, copper assists more than the other metals in triggering the active sites with the multifunctional activity of Cuf in the field of energy applications.[125,126] Finally, the current challenges and future perspectives about technology transfer are also outlined and the understanding of DHBT-derived Cuf in energy generation, conversion and storage will be furnished to benefit the researchers working in this particular field. This feature article will also focus on the mechanism and experimental considerations of this particular technique, its superiority over other conventional fabrication techniques of Cuf, the intrinsic physical and chemical properties of the as-derived Cuf along with the challenges of employing such nanometric structures in real applications and a methodical way to deal with those issues to establish a new direction in technology. The sheer simplicity and efficiency of this method in producing reliable 3D interconnected nanostructures open up new avenues for this technology to massively grow in the near future.

3. Various strategies for Cuf synthesis

It is important to discuss various strategies that have been widely in use for the synthesis of porous nanostructures of Cu in order to understand why the DHBT technique is crucial for the customized design of controlled dendritic growth, open porous morphology, ample defects and the potential for post-deposition treatments to improve activity. Several parameters of Cuf, such as high specific surface area, porosity, fluid permeability, composition, distribution of pore size, surface properties, thermal and chemical stability, electrical conductivity, as well as mechanical strength, are important from the application point of view. The ample need for Cuf as a current collector or substrate in energy applications, even in solid-state devices, encourages the development of a facile method for its synthesis.[127–129] Unfortunately, most of the synthesis methods for Cuf have been very expensive, tedious, multi-step processes. This section, therefore, will describe a few of the most conventional synthesis techniques for Cuf synthesis as listed schematically in Fig. 2a along with the SEM images depicting the morphological variation of Cuf formed from different routes. We have focused on demonstrating the benefit of the electrodeposition technique (DHBT) as it produces a tuneable hierarchical open pore system, which is suitable for electrocatalysis and other energy applications.

The powder-based dealloying technique can be employed to develop nanoscale copper foams having a pore size distribution in the range of a few hundred nanometers. It can also be considerably modified to produce multiscale copper foams. Jo *et al.* proposed an inexpensive yet multistep synthesis method for Cuf preparation based on a powder-metallurgy process that yields both micro and nanoporous Cuf.[6] On the other hand, Sharma *et al.* successfully fabricated Cuf with 74% interconnected porosity using a friction stir welding machine by a sintering and dissolution process using dendritic copper

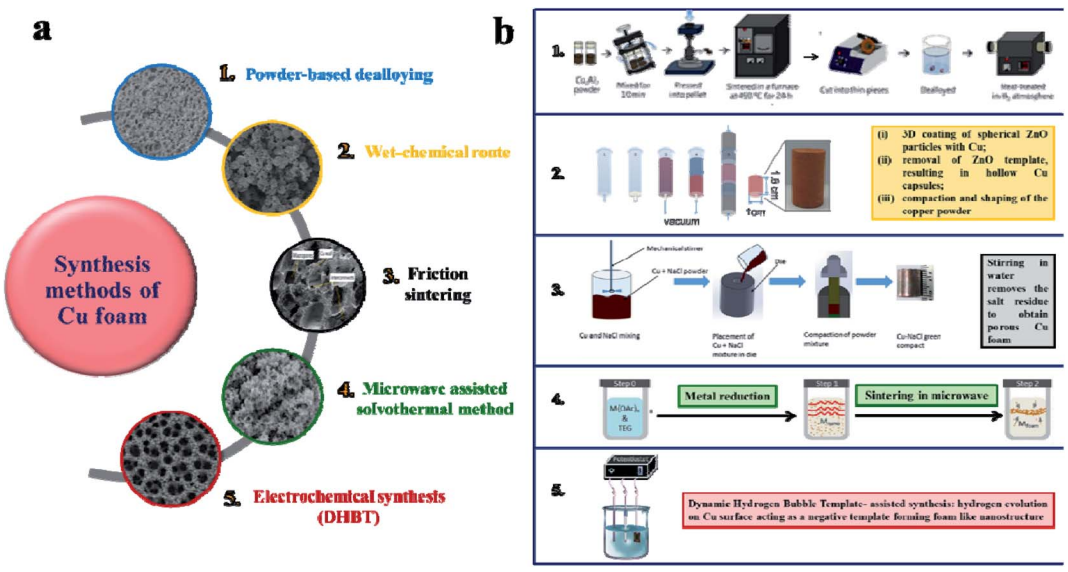

Fig. 2 Schematic representation of the different synthesis techniques of Cuf and the corresponding SEM images. (a and b) (1) Represents the powder-based dealloying method, where powdered Cu–Al is made into a pellet, sintered, and dealloyed to obtain only Cu and pyrolyzed to obtain Cu foam. Reproduced with permission from ref. 6, copyright 2014, Elsevier. (a and b) (2) Represents the wet chemical route, which is basically a template (ZnO)-assisted method. Reproduced with permission from ref. 15, copyright 2013, Wiley. (a and b) (3) Represents the friction sintering method where Cu along with NaCl salt is compacted, followed by water-etching of the salt to produce Cu foam. Reproduced with permission from ref. 29, copyright 2019, Springer Nature. (a and b) (4) Represents a simpler microwave-assisted solvothermal method where Cu is reduced and sintered in a suitable solvent to get the foam-like morphology. Reproduced with permission from ref. 61, copyright 2017, Royal Society of Chemistry. (a and b) (5) Represents the most convenient electrochemical synthesis route (DHBT), where H_2 evolution on Cu foil acts as a negative template forming Cu foam. Reproduced with permission from ref. 10 copyright 2019, Royal Society of Chemistry.

powder and cuboidal NaCl.[29] The obtained mixture was poured into a die and compacted in a hydraulic press as shown in Fig. 2b(3). The Cuf thus produced often suffers from the possibility of aerial oxidation during the synthesis process. Microwave-generated materials have received substantial theoretical as well as experimental interest. Microwave-assisted solvothermal processes enable the synthesis of distinct nanoparticles in loosely coupled nano-sized particles at significantly lower temperatures and pressures than commonly occur. Particularly, metal orthovanadates are utilized in microwave devices, photoluminescence, IR lasers, LEDs, and photocatalysts.

3.1 Electrochemical synthesis

Electrochemical deposition utilizing the dynamic hydrogen bubble template synthesis technique is a unique route for synthesizing a self-supported foam electrode (Fig. 2b(5)). Self-supported electrodes are usually more mechanically sturdy, devoid of any technical difficulties usually faced in a drop-casting (slurry cast on a current collector) method such as contact issues, increased thickness or producing a bulky rigid structure. Due to a well-integrated ionic diffusion pathway, these electrodes hardly face any interfacial resistance while participating in an electrochemical process and therefore, offer extensive long term cyclability. Additionally, the pore size of the developed foam can be extensively controlled using this method. The concept of electrodeposition originated with the synthesis of Ni foam by Marozzi and Chialvo,[92,93] which was later adopted by Shin *et al.* in 2003 (ref. 94) for the synthesis of Cuf for the very first time. Shin *et al.* deposited a self-supported nano-ramified Cuf accompanying hydrogen evolution. The process is very simple to produce an electrode with hierarchical porosity; even the surface of the foam obtained, happened to be very porous because the hydrogen gas continuously evolves from the surface as well as from the deposited dendrites. As demonstrated, the anode and the cathode electrodes of copper foil (5 cm^2) were placed at a typical distance of 2 cm inside the solution of 0.2 M copper sulphate and 1.5 M sulphuric acid (conventional baseline deposition bath for Cuf synthesis) and a constant current of 3 A cm^{-2} was applied by the potentiostat. The evolution of hydrogen gas is significant on the surface of the copper substrate at a high current density (>0.5 A cm^{-2}), which acts as a negative template to form a foam-like nanostructure. The reason behind this porous structure is that upon applying current, hydrogen bubbles are evolved at the cathode surface at the cost of the depletion of metal ions, due to which there is no deposition of Cu at those specific sites. Since these two processes (hydrogen gas evolution and Cu deposition) occur simultaneously, when the bubbles leave the substrate and travel the path to the air–electrolyte interface, a definite porous morphology is attained for the deposited Cu. Various experimental factors like deposition time, applied current, bath temperature, *etc.*, regulate the porosity and pore diameter of the Cuf, which are elaborated on in the later sections. The fine morphology of the Cuf is strictly determined by the nucleation and growth mechanism of Cu, which is, in turn, dependent on the hydrodynamic conditions and overpotential. The complex relationship between the interactions of the interfacial tensions between the 3-phase system-electrode/electrolyte/gas needs to be understood, which has been outlined in the subsections below.

3.1.1 Formation mechanism. The characteristics of the porous Cuf are reliant on many factors: (a) the state of the copper metal being deposited, (b) the current density and overpotential that is employed, (c) the concentration and the composition of the electrolyte, and (d) ambient conditions such as temperature. This method for the Cuf synthesis can be done using a two-electrode system (cathode/copper-working electrode and anode/copper-counter electrode) as well as a three-electrode system (cathode/copper, anode/copper and a reference electrode) in an acidic solution of copper salt. The three-electrode system is often preferred because it allows better precision of the overpotential. A schematic illustration of the three-electrode system is represented in Fig. 3. In the DHBT method, at a high current density and applied potential, the reduction of metal ions takes place simultaneously with hydrogen gas evolution from H^+ of the acidic electrolyte (Fig. 4). The possible reactions that occur are shown in eqn (1)–(3):

$$Cu^{2+}(aq) + 2e^- \rightleftarrows Cu(s);\ E^0 = 0.34\ V \quad (1)$$

$$2H^+(aq) + 2e^- \rightleftarrows H_2(g);\ E^0 = 0.0\ V \quad (2)$$

$$CuSO_4 + 2e^- \rightarrow Cu_{metal} + {SO_4}^{2-} \quad (3)$$

The hydrogen bubble formation on the Cuf electrode goes through three basic steps: nucleation, growth, and separation as depicted in Fig. 5. The coalescence of the small bubbles forms larger-sized bubbles on the surface, which get detached at the bubble break-off diameter, depending on the morphology of the electrode surface. The hydrogen bubbles block and insulate the surface sites of the electrode and thus the remaining accessible areas are preferred for Cu deposition. At the break-off state, the bubbles break, leaving behind void spaces that form the foam-like morphology of the metal. Thus, it is called a dynamic hydrogen bubble template (DHBT) process. By regulating the dynamics of the hydrogen evolution,

Fig. 3 Schematic of a three-electrode setup used in DHBT for Cuf synthesis.

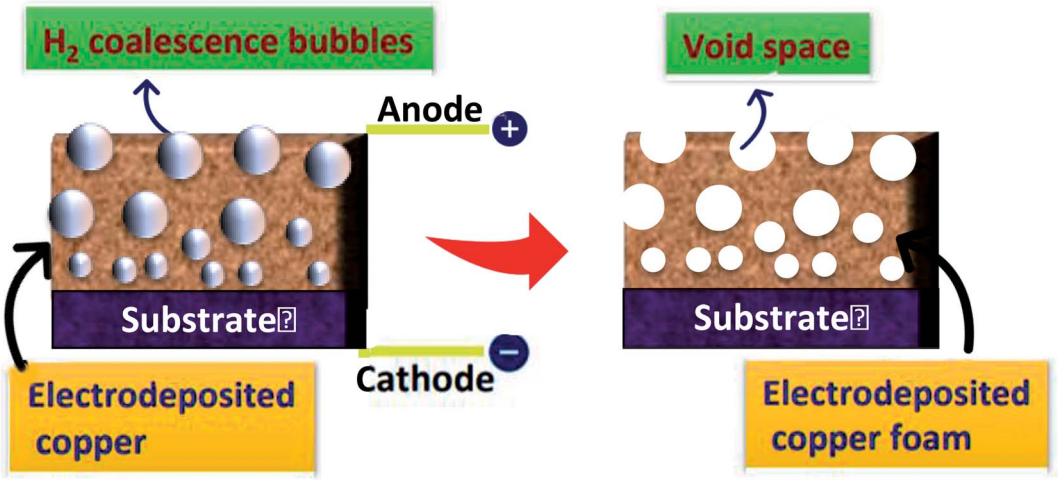

Fig. 4 Schematic representations depicting the formation mechanism of electrodeposited copper foam.

the physique of the template for the formation of pores can be modulated.

No traces of oxide formation of copper (CuO, Cu_2O) are usually observed in the X-ray diffraction (XRD) pattern obtained for DHBT-derived Cuf, although copper is supposed to be easily oxidized, once again revealing the superiority of the process.[10,130] The presence of abundant protons in the highly acidic aqueous environment of the electrolyte resists the oxide formation and promotes the reduction of copper ions into metallic copper, as expressed by eqn (4) and (5).

$$CuO + 2H^+ \rightarrow Cu^{2+} + H_2O \quad (4)$$

$$Cu_2O + 2H^+ \rightarrow Cu^{2+} + Cu + H_2O \quad (5)$$

3.1.2 Concept of dense branching. The dendritic electrodeposition of copper is crucial to attaining a highly porous hierarchical 3D network that not only helps in faster charge transport kinetics because of its porosity but also provides significant edge effects on the nanograin boundaries of the branches to enhance the reactivity of electrocatalysts. The Laplace field is a key factor for investigating the morphological characteristics of the ramified branches called dense-branching morphology (DBM). The fundamentals behind this finding are based on the dependence of electric potential on the Laplace equation and concentration gradient on the diffusion equation, which determines the envelope of DBM (eqn (6)). The current of the cell could be controlled by the Laplace field. The tip front of the dendritic needles and the agglomerates could be determined by surface tension and the diffusion field. Near the interface, the Laplace and the diffusion field decouple and by further varying the velocity, the global properties of the synthesized porous copper dendrites like shape, interface characteristics and stability can be analysed:

$$\frac{\partial c\pm}{\partial t} = -\nabla j\pm = \nabla(c \pm \mu \pm\ z \pm F\nabla\phi + D \pm \nabla c \pm) \quad (6)$$

where $j\pm$, $c\pm$, $\mu\pm$, $z\pm$, $D\pm$ are the flux, concentration, mobility, charge of the cation and anion, and diffusion constant, respectively. ϕ is the electrostatic potential and F is the Faraday constant.

3.1.3 The bubble nature. For the electrodeposition of Cuf from the DHBT method, a certain overpotential or current density must be imposed on the copper electrode for the development of gas–liquid–solid three-phase interfaces. As

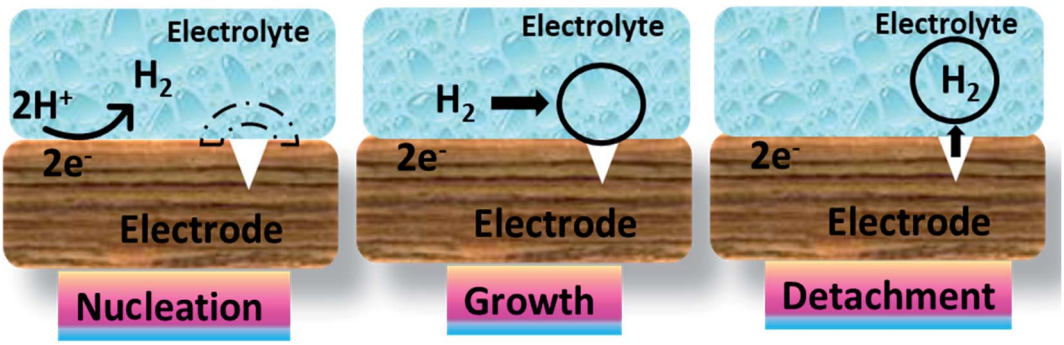

Fig. 5 Schematic representation of the bubble formation from nucleation to detachment on the copper foam.

discussed above, the electrodeposited Cuf only adopts the bubble as the template, and the bubble behaviour critically depends upon the various parameters like time, current density, analyte concentration, *etc.* The most important point here is that the pore size is finally dependent upon the break-off diameter of the bubble (d). The formula for the break-off diameter is expressed in eqn (7):

$$d = 0.02\theta(\gamma/g(\rho_1 - \rho_g))^{0.5}(1 + 0.2il/(Am^{(-2)}))^{0.45} \quad (7)$$

where q is the contact angle, g is the gravity of acceleration, γ is surface tension, i is current density, ρ_l is the liquid density and ρ_g is the gas density, θ is the surface wet ability.

4. The effects of various synthesis parameters on the physical properties of electrodeposited Cuf

The synthesis of Cu foam is directly modulated by various parameters such as current density, deposition time, electrolyte concentration, bath temperature, substrate effect and the introduction of additives, which in turn tune the morphology and mechanical strength of the porous metal.[131] The net effect of these parameters is the variation in the dendritic nature and grain size of the Cuf as appended briefly in the following sections.

4.1 The effect of current density

The change in the physical characteristics with the change in the current density during the process of electrodeposition gives insight into the versatility of Cuf. The rate and nature of dendrite formation are improvised by the applied current density and the overpotential of the process, in terms of how fast the hydrogen evolution reaction (HER) occurs and the hydrogen bubbles leave the electrode surface with a small break-off diameter resulting from reduced coalescence (Fig. 6). The nucleation rate "w" occurring during the electrodeposition is expressed in eqn (8):

$$w = k_1 e^{-\left[\frac{k_2}{\eta_k}\right]} \quad (8)$$

where k_1 and k_2 are constants and η_k is the overpotential. This overpotential in turn affects the nucleation radius (r_c) and grain size according to eqn (9):

$$r_c = \frac{\pi h^3 E}{6 Z_e \eta_k} \quad (9)$$

where Z_e is the electron number of discharge ions, E is the energy associated with the interface and h is the height formed by absorbent atoms. At a lower current density, few H_2 bubbles evolve on the surface of Cu foil with the abundant availability of deposition areas on the substrate, thereby producing the irregularly scattered morphology of Cu films. However, the structural aspects of Cuf, *i.e.*, pore size, grain refinement and

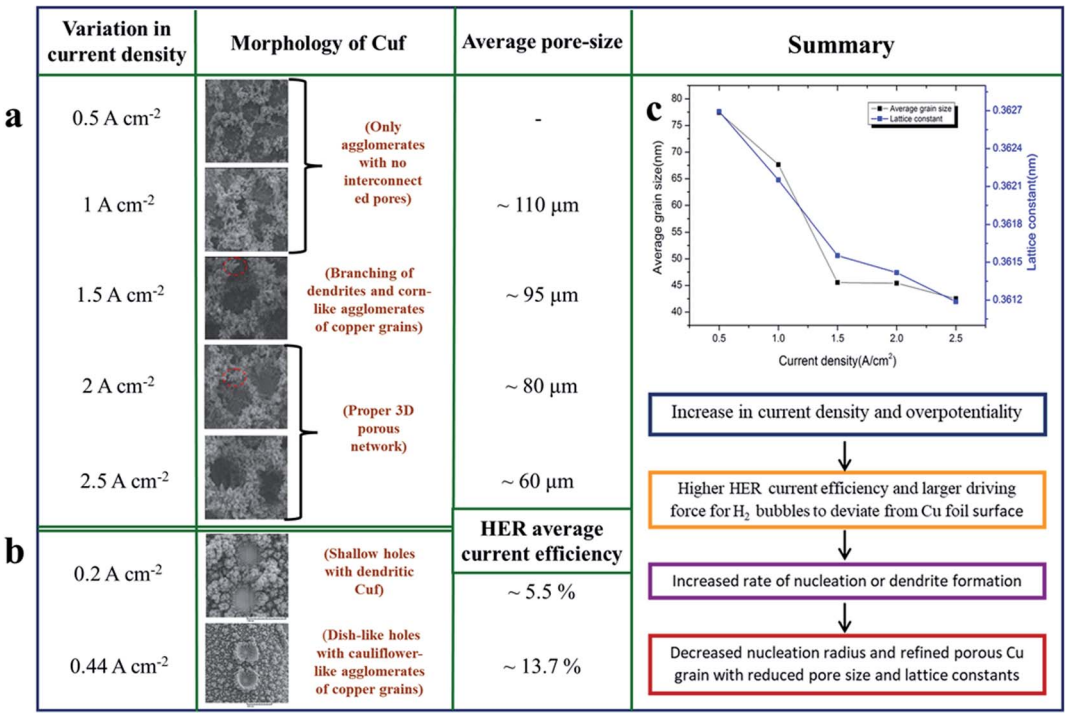

Fig. 6 (a) The effects of current density on the variation of the morphology and pore structure of the electrodeposited Cuf. The SEM images of Cu foam produced at different current densities from 0.5 to 2.5 A cm^{-2}. Reproduced with permission from ref. 3, copyright 2015, ESG. (b) SEM images of the Cuf deposited at 0.2 and 0.44 A cm^{-2},[14] copyright 2012, Springer. (c) The image depicting the dependence of grain size and lattice parameter on current density is reproduced with permission from ref. 27, copyright 2011, Springer Science + Business Media, LLC.

lattice constants, can be improved with an increase in the deposition current density[27] as summarized in Fig. 6.

The same relation is valid while applying a pulsating current, where an increment in the current density amplitude intensifies the HER and produces smaller H_2 bubbles, yielding a honeycomb-type Cuf structure with reduced pore size. The above-mentioned relation is elaborated on in the works presented by Niu *et al.*[3] and Nikolić *et al.*[14] However, the experimental exchange current density of the Cuf was reported as $10^{-5.37}$ A cm^{-2}, which is higher than that reported for gold foam.[132]

4.2 The effect of deposition time

The structure, porosity and thickness of the electrodeposited Cuf largely depend on the time of deposition. The duration of the deposition of Cuf is a critical parameter because the hydrogen bubble produced from the surface of the negative electrode in the electrolyte participates in collisions, deformation, coalescence, bubble break-off, and detachment affected by the surface tension and greatly varies with respect to the time of deposition. Dey *et al.*[1] and Zhang *et al.*[2] have shown that at a constant current density, with increasing the deposition time, the pore diameter of the Cuf increases. Fig. 7a shows the laser confocal scanning microscope (LCSM) images of the Cuf synthesized at different deposition times and it illustrates that besides the increase in pore size with the increase in deposition time, the pore thickness also increases significantly and as a consequence of the two increments, the number of pores per unit area or the pore density decreases. To elaborate on this point, as shown in Fig. 7a, with the increase in deposition time from 5 to 10 s, the average diameter of 25–30 μm small holes were generated, which was estimated to be the size of hydrogen gas evolved. As the duration was increased, the nesting of bubbles within the pores increased and thus resulted in the formation of a hierarchically porous network depending on the variation of the diameter of hydrogen gas bubbles. Accordingly, the thickness of the pore wall was also increased, leading to the increase in the pore diameter with the decrease in the pore density. However, for the potential deposition of Cuf, there must be a certain limitation on time because with time, the thickness of the pore wall also increased while causing the disordering of the structure. This disordering could lead to the collapse of the porous 3D network in the electrolyte itself or the filling of the copper pores with copper dendrites resulting in the disappearance of the porous structure.

4.3 The effect of bath temperature

Another crucial parameter is that the bath temperature hugely influences the surface properties of the electrodeposited Cuf as highlighted by Niu *et al.* With the increase in the deposition temperature, more hydrogen evolution occurs, resulting in a larger bubble template.[3] This leads to an increase in the interspacial distance between the bubbles, due to which the pore size of the electrodeposited Cuf increases. This can be well represented as shown in Fig. 7b; however, a bath temperature beyond 40 °C has a detrimental effect on the grain size refinement and dendrite consistency of the Cuf. It is worth noting that the variation of the deposition time or bath temperature hardly has any impact on the crystal structure of the face-centred cubic Cuf. However, the peak intensity seemed to be reduced with increasing deposition temperature since the lattice parameters are highly dependent on the temperature, unlike in the case of time-dependency as shown in Fig. 7c and d. One plausible explanation is that a rise in the bath temperature enhances the electrochemical reaction and diffusion rate of ions and thus the coarser crystal structure is adorned with defects that reduce the crystallinity of the deposited foam (Fig. 7d).

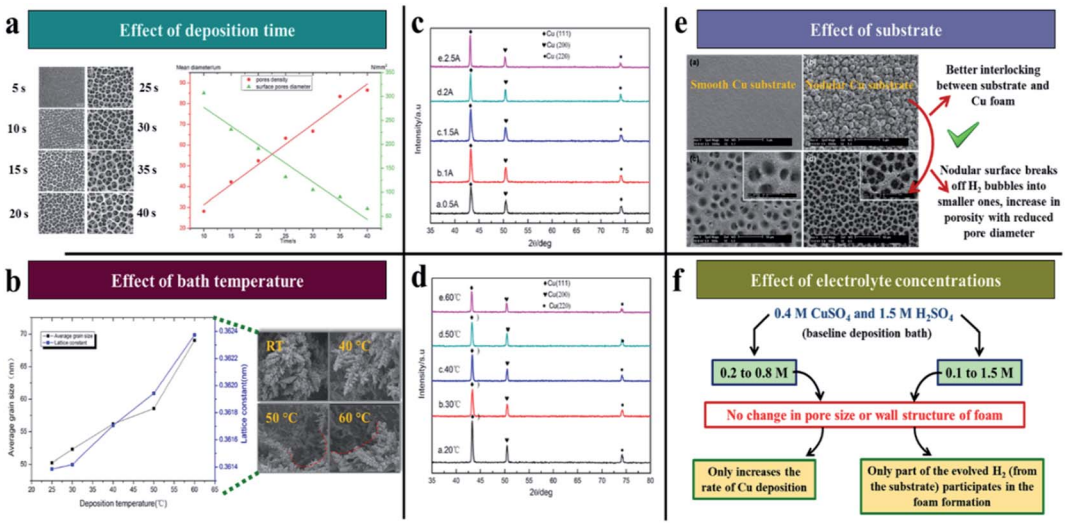

Fig. 7 Representation of the effects of different experimental conditions on Cuf synthesis and properties. (a) The effect of deposition time; reproduced with permission from ref. 2, copyright 2013, The Electrochemical Society. (b) The effect of bath temperature; the effects of (c) applied current and (d) bath temperature on the XRD pattern of deposited Cuf. Reproduced with permission from ref. 3, copyright 2015, ESG. (e) The effect of substrate. Reproduced with permission from ref. 43, copyright 2010, The Electrochemical Society. (f) The effect of electrolyte concentration.

4.4 The effect of the substrate

The morphology of the substrate plays a critical role in modulating the morphological architecture of the electrodeposited Cuf. The porous morphological structure and mechanical properties of Cuf are greatly dependent on the adhesion between the electrodeposits and the underlying substrates and vary significantly from nodule-type to smooth-type Cu substrates as demonstrated by Kim *et al.*[43] The nodule-type structure leads to better adhesion between the substrate and the Cuf because of the interlocking effect between them. Also, the behaviour of the H_2 bubbles generated on both substrates differed during the electrodeposition process; that is, on a nodule or rough-type substrate, the H_2 bubbles rapidly split into smaller ones resulting in highly porous structures with small pores of Cuf, unlike the Cuf electrodeposited on a smooth-type Cu substrate (Fig. 7e).

4.5 The effect of analyte and electrolyte concentration

In 2004, Shin *et al.* reported the tailoring of the porous morphology-like pore size and the size of the dendritic branches upon changing the concentration and the composition of the electrolyte (Fig. 7f).[133] With the concentration of the copper salt being varied from 0.2 M to 0.8 M $CuSO_4$, the deposition rate of copper increased while there was hardly any variation in the pore size and branch thickness. The acid concentration also hardly played any role in determining the porosity of Cuf because even if the concentration of the acid was varied, only the hydrogen bubbles evolved on the Cu substrate at a defined potential, current density, and deposition time regulated the morphology of the pores.[134]

4.6 The effects of additives

The electrolytes fed with additives showed a modulating range of porosity for the electrodeposited Cuf and thereby influenced the mechanical properties by altering the mechanical stiffness and strength of the deposited foam. The control of the branch size of the copper was carried out previously by researchers[135–137] and it has been suggested that alkaline sulphates, chlorides and bromides[138] play a role in reducing the branches. Similarly, additives like cetyltrimethylammonium bromide (CTAB)[139] and acetic acid act as a bubble-stabilizer by reducing the hydrophobic force of the bubbles and surpassing their coalescence. This leads to reduced pore size and dendritic branches of the Cuf from 50 μm to 25 μm.[133] Kim *et al.* demonstrated the effects of different ions like NH_4^+, Cl^-, polymers such as polyethylene glycol (PEG) and 3-mercapto-1-propane sulfonic acid (MPSA) as additives in the acidic cupric sulphate bath solution on the mechanical and structural properties of the deposited Cuf. Among all the additives, NH_4^+ is the most effective suppressant of the Cuf deposition, as well as the hydrogen evolution, as it gets adsorbed on the cathode surface and thus increases the cathodic overpotential.[140] As such, a larger pore diameter of the Cuf is attained with a less populated dense branching and hence, mechanically strong Cuf. However, for the reversal of surface porosity, the addition of Cl^-, PEG and MPSA resulted in the formation of a very dense porous structure with reduced pore size and wall thickness, despite the presence of NH_4^+. On the contrary, Nam *et al.* showed that benzotriazole (BTA, itself a suppressing agent) as well as $(NH_4)_2SO_4$ combined to result in the formation of a grape-like Cuf morphology with high ductility but less mechanical strength.[141] Tan *et al.* suggested that unlike the Cl^- ions, the morphology and the microstructure of the electrodeposited copper foam becomes less porous with boosted pore size, thickness and dense dendritic growth upon the addition of bromide ions.[142] This can again be overcome by the introduction of PEG along with Br^- ions. A combinatorial effect of the two results in the simultaneous formation of CuBr as well as a Cuf with a smaller surface pore size and thickness than that with only bromide but larger than that obtained from the PEG as an additive. In another work, Moffat *et al.* discussed the addition of $[Na_2@SO_3(CH_2)_3S]_2$ (SPS) with PEG–Cl into the acidic cupric solution, disclosing that competition took place between PEG and the surface active sites in Cuf deposition.[143] There happened to be a synergistic effect between PEG and chlorine ions/Cu ions, which resulted in the formation of passivated films that actually inhibited the film deposition by two orders of magnitude. Also, the addition of disulphide or the group ending with sulfonates (SPS) resulted in the disturbance and displacement of the passivated film from the surface and thus accelerated the metal deposition rate. The positive and negative effects of different additives on the electrodeposition technique of Cuf synthesis and hence on its properties are summarized in Table 1.

5. Significant inherent properties of electrodeposited Cuf

As discussed in the previous section, the morphology, pore diameter, pore density as well as thickness of the electrodeposited Cuf are majorly improvised by varying conditions of current density, deposition time, temperature, *etc.* Consequently, the inherent properties of the foamy structure such as hydrophobicity or hydrophilicity, surface porosity, mechanical and electrical properties also show drastic changes. This section mainly discusses the intrinsic properties of the nano-ramified dendritic structure and what kind of ideal morphology of Cuf is beneficial for its crucial role in various applications in energy devices.[144]

5.1 Hydrophobicity, hydrophilicity and aerophobicity of Cuf dendrites

The surface wettability of a material is always an interesting and crucial property to be analysed as it is directly related to the surface energy of the material, which in turn influences its contact with the physiological environment. The reason this is a topic worth mentioning for electrodeposited Cuf is that the surface property or wettability of 3D Cuf shows versatile behaviour from superhydrophobic (water contact angle (CA > 150°)) to superhydrophilic (CA close to 0°) as reported by Lin *et al.* For example, when Cuf is coated with *N*-dodecyltrimethoxysilane, it leads to the electrical switching of the

Table 1 The effects of additives on the preparation of copper foam

Additives			
Category	Examples	Effect on Cuf deposition	Extended effects on properties of Cuf
Cations	NH_4^+	Act as suppressant to Cuf deposition	Boosted pore size
Anions	Br^-		Large pore diameter with less populated pores Thick pore walls with dense dendrites Mechanically strong Cuf
	SO_4^-, Cl^-, $R–SO_3^-$	Bubble stabilizer	Reduced pore size and wall thickness
Polymers	Polyethyleneglycol (PEG)	Reduced H_2 bubble coalescence	Reduced branching
Others	3-Mercapto-1-propane sulfonic acid (MPSA), benzotriazole (BTA), cetyl trimethylammonium bromide (CTAB), acetic acid	Enhanced foam deposition	Very dense porous structure Ductile Cuf with less mechanical strength

surface property of the foam; *i.e.*, when connected as the anode, the electrode demonstrated superhydrophobic behavior and when connected as cathode, the electrode showed superhydrophilic behavior.[145] The wettability of solid surfaces is usually governed by both the chemical composition and the geometrical microstructure of the surface, which is tuned with the help of modifications and the roughening of the surface. Additionally, Li *et al.* beautifully demonstrated that the pore size and dense branching affect the wettability of the Cuf. The tunability of the pore size of Cuf from 10–150 μm with variable parameters precisely helps to switch its behaviour from superhydrophobic (lesser pore size) to superhydrophilic (higher pore size) for applications involving inhibiting phenomena, such as snow sticking, contamination, or oxidation and current conduction.[139] Interestingly, Cuf shows superhydrophilic behavior as it leaves the production line, which means it pulls into a water droplet immediately due to very high capillary forces. In electrocatalysis, for example, in the hydrogen evolution reaction (HER)[146] or the oxygen evolution reaction (OER), plenty of bubbles are generated from the electrode, blocking the surface of the catalyst and making it inaccessible to the electrolyte ions, thus gradually decreasing the ECSA and eventually degrading the catalytic property. Thus, it is crucial to design the surface of the electrocatalysts as hydrophilic and aerophobic in nature, so that the interface is always available for electrolyte contact. Das *et al.* reported that their as-prepared Cuf surface with all the optimized experimental parameters possessed both hydrophilicity and aerophobicity.[10] While the superhydrophilicity of the Cuf surface was observed with the water contact angle measurement, the aerophobicity was shown *via* analysing the bubble formation during and after the voltammetric scan, when an 'abrupt renewal of gas bubbles' was observed throughout the experiment. With constant exposure to ambient air, however, the surface of the Cuf may lose hydrophilicity due to surface oxidation.[147] The surface energy changes with the formation of copper oxides and makes the surface hydrophobic. Various deoxidising agents are often used to regain the wettability of hydrophilic Cuf. Alternatively, with controlled synthesis parameters inducing a highly porous Cuf formation, superhydrophobicity can also be introduced on the surface of electrodeposited Cuf, as has been highlighted in several articles.[148,149] Thus, depending on the applications, the wettability of DHBT-derived Cuf can be tuned.

5.2 Porosity tuning of Cuf

The beauty of foam-based electrodes lies in their porosity parameters (such as-pore volume, pore diameter *etc.*), which are eventually imparted to the active surface area of the electrodes and critically contribute to the superior activity of the material in electrochemical applications. The flexibility and tunability of the porosity of the Cuf, such as variation in pore size, branch size, pore wall thickness, *etc.*, can be controlled with the help of additives, variant current density, and deposition time, bath temperature, as already discussed in the previous section. However, it is worth noting that all of the above parameters are directly related to the rate of evolution of hydrogen bubbles, the hydrophobic forces between them and their coalescence behaviour, which regulate the morphological architecture of the Cuf. It is interesting to further note that the hydrogen bubbles that evolve from the base substrate (Cu) lead to the formation of large pores while subsequent bubbles released from the freshly formed porous deposits create nanopores, thus providing a wide window for tailoring them according to their desired electrochemical applications.[94,130] Interestingly, Chen *et al.* reported that when synthesized *via* electrodeposition, the experimental value for the maximum realizable porosity of Cuf is around 99%, while in the case of nickel foam, it is only around 89%, once again indicating the excellent suitability of electrodeposited Cuf for a plethora of applications.

5.3 Mechanical properties

The open porous framework of electrodeposited Cuf is often subjected to compressive stress–strain profiling to understand the mechanical robustness.[101] The mechanical strength of the Cu nanofoam is largely dependent on the porosity and thickness of the pore walls. Zhou *et al.* showed that with increased

porosity and decreasing thickness of the pore walls, the strength of the foam decreases at any fixed strain in a particular region.[150] Moreover, in a high strain region, the stress increases less rapidly with strain, indicating dominant plastic deformation. Therefore, to increase the sturdiness and flexibility of a DHBT-derived Cuf, it is important to take care of the experimental conditions that produce optimal porosity and surface homogeneity so that it can be further used as a self-supported electrode.

5.4 Electrical properties

The electrical conductivity of porous metals like Cuf is one of the most important properties for electrode applications, which is controlled by the overall pore structure, *i.e.*, porosity,[151] pore size,[152,153] pore shape,[154] and pore orientation.[155] The change in electrical conductivity of porous metals as a function of porosity can well be described based on the Maxwell approximation. The electrical conductivity of Cuf decreases with increasing porosity due to surface anisotropy in the grain boundaries of the pore walls.[156] In simpler words, the higher the frequency of pores on a Cuf surface, the more prominent the loss in connectivity, leading to a loss of electrical conductivity since it prevents the free movement of electrons on the surface. Interestingly, however, for a given porosity, a larger pore size yields a higher electrical conductivity. It is assumed that a smaller pore size presents a lot more tortuosity in the conducting path of the electron than larger pores. With smaller pores, the average pore numbers increase in a given porosity. Therefore, due to perturbation from the stronger interacting electrical fields of the neighbouring pores, a considerable drop in the conductivity is generally observed.[157,158] If the experimental exchange current density of Cu is at an intermediate position on the "volcano curve",[132] with controlled experimental electrodeposition conditions, the DHBT-derived Cuf can possess a suitable pore size that may aid in enhancing its electrical conductivity, which is important for its electrochemical applications.[108] Fig. 8 shows the optimum conditions in order to obtain hydrophobic Cuf, with high mechanical strength and electrical conductivity. However, based on the application, these properties can be tuned by applying convenient experimental conditions as already discussed in the previous section.

6. Multifunctional applications of Cuf for clean energy technologies

Tailored nano-structural porous morphologies are gaining popularity due to their unique effects on tuning the optical, electronic, electrochemical, catalytic and mechanical properties. Possessing well-defined pathways for electrolytes to access rapid movement of ions associated with high electrical conductivity as well as superior ductility and malleability, these materials are leading the prospects as active electrode materials for energy applications.[159] This section highlights some examples of DHBT-derived Cuf that are being employed in a variety of energy applications (Fig. 9). The ability to create macroporous surfaces with high specific area through bubble templating is ideal for such tailored surfaces for a wide-spread application spectrum in electrochemical energy generation, storage and conversion systems.

6.1 Use in energy generation

Electrocatalysis for applications in fuel cells has been well studied for years, predominantly for noble metals, with the morphological control of nanoparticles that leads to enhanced current density or stability. DHBT further improves the understanding of how morphological tuning can impact the various electrocatalytic parameters.[160] The nano-ramified walls of dendritic Cuf possess superficially disoriented metal atoms, a huge ECSA and abundant micropores that produce

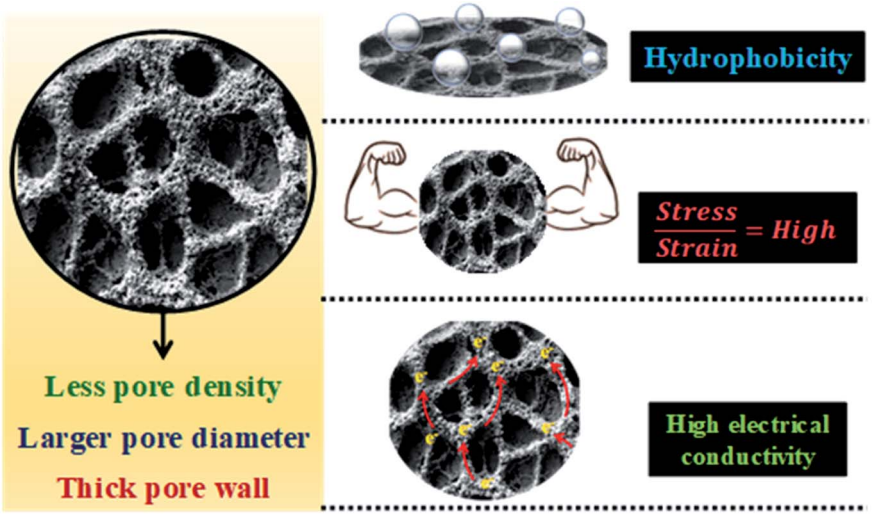

Fig. 8 Schematic representation relating to the nature of pore size and pore density with the inherent properties of Cuf. The SEM image of the Cuf has been reproduced with permission from ref. 1, copyright 2015, Royal Society of Chemistry.

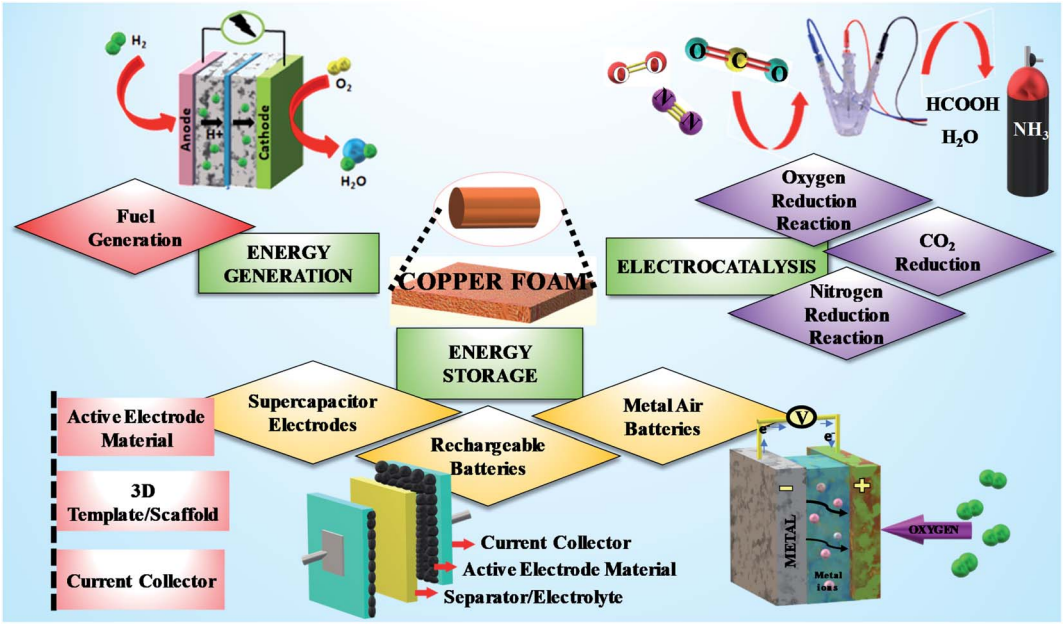

Fig. 9 Schematic diagram for multiple applications of copper foam.

a significant effect in the kinetics of water splitting[161] reactions involving adsorbed intermediates.[162]

6.1.1 Fuel generation. The growing requirements for hydrogen gas in industries for hydrogen economy and green energy have prompted interest in the characteristics of copper foam for electrochemical fuel generation. The hydrogen economy is the future of alternative sustainable energies since it produces only water when utilised in fuel cells, dramatically lowering pollution. One conventional means of hydrogen production is through methanol-reforming; however, the process has many serious environmental challenges and a carbon footprint. The production of H_2 gas *via* water splitting [$2H_2O(l) \rightarrow 2H_2(g) + O_2(g)$, $\Delta G^\circ = +237.2$ kJ mol^{-1}, $\Delta E^\circ = 1.23$ V ($T = 25$ °C, $P = 1$ atm) *vs.* the reversible hydrogen electrode (RHE)] has proven to be the easiest, most cost-effective and eco-friendly practise among all the other routes. Nevertheless, environmental issues can be overcome by adopting an electrochemical water electrolyser with a proton exchange membrane (PEM). The separating membrane is a significant portion of an electrolyser that only permits ions to pass through, rather than H_2 and O_2 molecules, and keeps both the gases distinct to evade the risk of flare-up due to unsolicited reaction.[163,164] Although noble metals such as Pt or RuO_2/IrO_2 have already been acknowledged to exhibit high activity in water splitting processes, new electrode materials have been designed in an attempt to reduce the cost and improve the efficiency of the electrocatalyst. However, among these potential candidates, Cuf-derived electrocatalysts are gaining much attention due to their versatility and affordability. In addition, a large ECSA is an important parameter for an electrocatalyst, which is accompanied by the foamy structure of the copper. By generating the porous 3D architecture electrochemically, the surface roughness increased, leading to greater activity. The alloy-like bimetallic materials-based electrocatalysts are known to be excellent candidates for water splitting applications. However, in order to split water more efficiently, researchers have utilised bimetallic alloy-based electrocatalysts integrated with the porous dendritic nanostructures with porous morphology. Liu *et al.* developed Cu–Ni core–shell nanostructures *via* electrodeposition, consisting of a nickel-rich shell and a copper-rich core.[165] Another study has been reported by Zhang and co-workers where the electrodeposition of two-phase Cu–Ni magnetic metallic foams (MMFs) with variable compositions was achieved by employing hydrogen co-evolution as a porosity source. A porous film exhibiting highly integrated nano-dendritic walls was developed when Cu and Ni were deposited within the hydrogen bubble interstices. In the films, the Cu/Ni ratio was controlled by altering the current density. Cu–Ni MMFs with Ni concentrations varying from 15% to 35% and customizable pore morphologies were developed. Additionally, these MMFs outperformed pure Cu and Ni porous films in terms of stability as well as composition-dependent electrochemical performance toward the HER. $Cu_{85}Ni_{15}$ MMF, in contrast, exhibited the highest appropriate efficiency.[166]

Hydrogen generation and storage adopting energy-efficient technologies continue to be a challenge, particularly hydrogen storage, which demonstrates peculiar issues. Chemical hydrogen storage materials, such as boron-based materials, have been examined since the early 2000s, for instance, $LiBH_4$, $NaBH_4$, ammonia borane NH_3BH_3 and hydrazine borane $N_2H_4BH_3$.[167,168] Sodium borohydride (SB) has been extensively explored as a liquid-phase hydrogen transport mechanism. It is indeed conceivable to generate pure hydrogen on-demand by hydrolysis in ambient environments by implementing stabilized SB solutions, as well as an acidic solution or a heterogeneous catalyst (eqn (10)).[169,170]

$$4H_2O/NaB(OH)_4 \rightarrow 4H_2 \quad (10)$$

This facilitates the control of H_2 release and enhances solution stability (at alkaline pH), allowing prolonged storage. Here, the key emphasis has been on identifying and developing metal-based SB hydrolysis catalysts.[171] Designing non-noble metal electro-catalysts, attaining significant hydrogen production rates with close to 100% conversion, and enhancing the long-term robustness of non-noble metal-based electrocatalysts by effectively addressing deactivation. The first objective has been accomplished with the development of cobalt-based catalysts which, under optimal conditions, seem to be as effective as noble metal catalysts.[170,172] The cobalt-based catalyst's stability is thus the most demanding feature.

Thus, the discovery of efficient catalysts based on non-noble metals like cobalt is essential to the advancement of sodium borohydride hydrolysis. Nevertheless, excessive deactivation reduces the stability of such catalysts. The electrodeposition of highly porous copper and cobalt-based bimetallic foams, Cu_x-Co_{100-x} was reported by Eugénio *et al.*, where copper-rich foams have a honeycomb-like morphology featuring open pores and pore walls with an open dendritic pattern Fig. 10(1).[5] Moreover, with increased Co content, the interconnectivity of the pores decreased and comparatively, Cu_{100} had low catalytic activity as compared to Co_{100}. However, a moderate amount of cobalt in the copper foams enhanced the catalyst's performance. $Cu_{85}Co_{15}$ catalysts were demonstrated to be significantly more active than Co_{100} due to electronic effects. The higher catalytic activity of $Cu_{85}Co_{15}$ was attributable to geometric effects related to modifications in the foam geometry. Consequently, copper-based catalysts could circumvent the limited stability of pure cobalt while maintaining significantly higher activity. Additionally, the fabrication of three-dimensional foam-like nanostructures utilising a dynamic hydrogen bubble template facilitates the fine-tuning of the catalytic performance of copper by adjusting the proportion of the second metal. Thus, in general, these analyses promote copper-based catalysts as a low-cost potential substitute to cobalt for boron hydride hydrolysis.

Platinum and palladium are the most active electrocatalysts. Due to the restricted supply of noble metals, it is imperative to prepare an electrocatalyst with sufficient mechanical strength and activity while using the minimum possible noble metals. The galvanic replacement reaction (GRR) is an efficient technique for the controlled fabrication of noble catalysts. Metal ions in aqueous solutions are reduced and replaced by metal on the substrate surface. Nanomaterials have been synthesized on metal or semiconductor substrates by this convenient and spontaneous technique. Additionally, the preparation of bimetallic particles has a favourable electrocatalytic effect owing to its electrocatalytic improvement. Bimetallic architecture with a second metal lowers the noble metal loading and enhances electrocatalytic activity through synergism. As a consequence, bimetallic catalysts possess superior catalytic abilities as compared to monometallic catalysts, which is attributable to their relatively high electrocatalytic activity, chemical stability, and increased surface area. In one of the recently reported works by Rezaei *et al.*, they demonstrated the synthesis of Pd/Pt-based bimetallic nanofoam fabricated on electrochemically

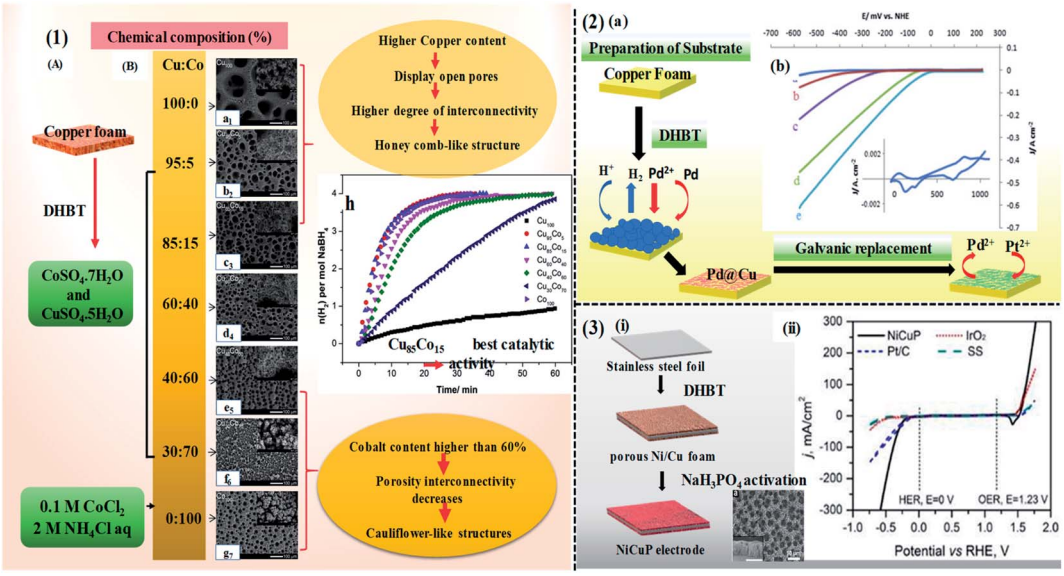

Fig. 10 (1) (a–g) SEM images of Cu_xCo_{100-x} (with x varying between 0 and 100). (h) Hydrogen evolution curves: hydrolysis of sodium borohydrate in the presence of Cu_xCo_{100-x}. Reproduced with permission from ref. 5, copyright 2016, Elsevier. (2) (a) Formation mechanism of $Pd_{65}Pt_{35}$ catalyst on Cu nanofoam. (b) HER activity analysed from the linear sweep voltammetry test, (a) bare Cu metal electrode, (b) Cu nanofoam-based electrode, (c) Pd on Cu nanofoam, (d) Pt on Cu nanofoam, (e) $Pd_{65}Pt_{35}$ on Cu nanofoam. Inset shows the cyclic voltammetry of $Pd_{65}Pt_{35}$ on Cu nanofoam scanned in 0.5 M H_2SO_4 electrolyte at a scan rate of 10 mV s^{-1}. Reproduced with permission from ref. 18, copyright 2015, Elsevier. (3). (i) Formation mechanism and SEM image of the NiCuP electrocatalyst; the inset shows the cross-sectional view of the electrocatalyst. (ii) HER and OER activity (LSV curves) of the catalyst NiCuP with all the control samples. Reproduced with permission from ref. 49, copyright 2017, Royal Society of Chemistry.

grown Cuf and tested for HER activity for different samples as illustrated in Fig. 10(2). Among the several compositions, $Pd_{65}Pt_{35}$ performed better than even the pure Pt on Cuf, which had an onset potential of only 5 mV at a current density of 276 mA cm^{-2}.[18] It has been confirmed that lower Pt/Pd loading leads to greater activity due to a better electronic effect.

The uniqueness of Cuf as a core architecture for the development of various core–shell nanostructures for electrocatalytic applications was also explored by various groups. Lu *et al.* used Cuf as the core, oxidised it to generate CuO, and then developed Ni–Co–S on it as a shell to serve as an effective electrocatalyst for the oxygen evolution reaction. To reduce charge transfer and series resistance, 3D Cuf with a core–shell architecture has many active sites and short diffusion paths, allowing for high-speed electron transport.[173] Yu *et al.* also discussed the design of the Cu@CoFe layered double hydroxide (LDH) core–shell nanostructure supported on Cuf, which facilitates the accessibility of active sites during the electrochemistry charge transport, thus boosting the reaction kinetics by decreasing the electron transfer barriers.[174] In prior research, metal phosphides, sulphides, and selenides were demonstrated to effectively catalyze the HER.[175–177] Such catalysts effectively stimulate both the HER and OER in the same environment, providing a competitive advantage in generating electrolysers with one adaptive catalyst for both cathodic and anodic responses, which would be a strategic attribute in the water electrolyser industry.[178,179] Such OER activity is primarily derived from metal oxides, metal hydroxides, or oxyhydroxides generated *via* catalytic synthesis or *in situ* conversion of phosphides or selenides.[180,181] Moreover, the catalyst architecture and physicochemical properties are significant for enhancing the water electrolyzer performance, which facilitates numerous active sites, resulting in quicker H_2 or O_2 production. This speeds up the mass transfer, allowing for faster electrolyte replenishment as well as the removal or disappearance of coalescent H_2/O_2 gas bubbles, respectively. Nevertheless, achieving high-efficiency electrodes for the electrolysis of water has been a challenge.[182,183] However, strong mechanical adaptability for the long-term electrolysis of water under high current densities could be provided by intrinsically linked metallic frameworks with multi-scale permeability. Such metal complexes should contain bifunctional HER and OER catalysts. Thus, Wei *et al.* developed a bi-functional water electrolysis catalyst, NiCuP, exhibiting exceptional activity, durability and relatively close faradaic performance *via* bubble-assisted electrodeposition to form NiCu on a steel substrate, followed by a low-temperature phosphidization process to convert NiCu into NiCuP.[49] Stainless steel foils were subsequently deposited over 40 m thick hierarchically porous NiCu nano-foams of 6.70 mg cm^{-2} density, which delivered remarkable HER and OER efficacy with overpotentials of −146 and 300 mV in 1 M KOH. These results outperformed Pt/C and IrO_2 catalysts. Moreover, the bifunctional catalyst remained active at 50 mA cm^{-2} for over 120 hours. It also displayed gas bubbles that would not impede electrode pathways or dislodge catalysts from electrodes while applying ultrahigh current density up to 500 mA cm^{-2}. In particular, they could be used as electro-catalysts for the electrolysis of water, although they also offer wide potentials in other electrochemical applications such as batteries or fuel cells, considering that their surfaces could be readily activated by diverse chemical techniques Fig. 10(3). In one of our recently published studies, we synthesized a core–shell-based nanostructure architecture, Cuf@Ni_5P_4, where Cuf represented the core, whereas single-phase Ni_5P_4 formed the shell.[10] A schematic of the synthesis is illustrated in Fig. 11a. The porous morphology was confirmed *via* SEM and TEM characterisation techniques as displayed in Fig. 11b–e. Further, the material was utilised for electrochemical applications. Interestingly, better performance was delivered for the HER in acidic media (90 mV, 10 mA cm^{-2}). The interfacial study has also been explored and it was concluded that the interface of the Cu (111) plane in Cuf@Ni_5P_4 efficiently played a significant role in accumulating the charges and was depleted through the Ni_5P_4 shell as shown in Fig. 11l. As a continuation to this study, we also reported that the desired synthesized material demonstrated full water splitting performance in basic media (1.66 V, 10 mA cm^{-2}) with commendable activity [Fig. 11f–k].[28] The study showed that the Cuf@Ni_5P_4 was compatible even when hybridized with an external device like the solar cell. The electrodeposited Cuf, therefore, displayed versatility in the field of energy as fuel generation.

Incorporating Cuf with various transition metal-based chalcogenides has also been widely practised for enhanced electrocatalytic performance. Zhau *et al.* designed a core–shell catalyst NRs@CoS/CF (full form) decorated on Cuf for water splitting, where Cu_2S acted as the core and CoS as the shell. Here, they demonstrated that the synergistic effect between the core and the shell and the strong electron exchange through sulphur to both the metals is responsible for superior electrocatalysis, which eventually resulted in the improvement of the electrocatalytic activity.[184] In order to validate the superiority of Cuf as an electrode active material, Liu *et al.* theoretically studied the role of Cuf in their as-developed samples, CoS_x and Cu@CoS_x using DFT calculations to analyse the role of Cuf by taking the (111) facet of Co_9S_8, which has the lowest surface energy to absorb water molecules, preferably over the facet. As shown in Fig. 12a–g, the redistribution of charge at the interface region increases the electron density in the Cu cluster by transferring electrons from Co atoms to Cu atoms by depleting the electrons at the interface of the Co atom and facilitating the dissociation of water molecules to boost activity. The hybridised Co and Cu species confirmed the interaction between Cu and Co atoms and differentiated the activity in Cu@CoS_x with and without Cuf. Thus, the Cuf clusters enhance the electronic properties, electronically interact with the interfaces, facilitate the adsorption energy for catalysis of the reaction and boost the drifting of electrons.[13] Conversely, constructing a thermodynamically stable multi-component electrodeposition catalyst is problematic. When employing an electrolyte containing Ni and P precursors to electrodeposit a Ni–P catalyst, metallic Ni is invariably formed along with the Ni–P catalyst. However, surface Ni seems to be more thermodynamically unstable than positively charged nickel linked to P, causing the corrosion of metallic Ni in an acidic medium.[185,186] Electrochemical leaching

at an adequate potential in an acidic medium can be employed to eliminate excess Ni and hence minimize corrosion.[187] The removal of metallic Ni may indeed influence the electrochemical characteristics of the catalyst by altering the atomic composition at the catalytic interface.[188] Recently, Yeon *et al.* also prepared electrodeposited Ni–P on electrochemically synthesized Cuf fabricated on carbon paper and demonstrated the electrocatalyst using a proton exchange membrane-based water electrolyzer for hydrogen production and utilized electrodeposition and post-treatment to generate Ni–P electrocatalysts for HER.[189] Initially, porous CF was electrodeposited on carbon paper (CP) to provide additional active sites and superior electrical conductivity. Subsequently, to achieve appropriate HER performance and stability, Ni–P was electrodeposited on the CF under optimized deposition conditions including anodic leaching. An anodic leaching process of the prepared Ni–P/CF/CP electrocatalyst was done at 0.17 V *vs.* RHE in acidic medium at various times to remove excess Ni for better electrochemical activity. It was observed that as the anodic leaching time increased, the size of the Ni–P particles decreased in the acidic medium. The change in the atomic composition of Ni was estimated from 89.6% to 75.6% as the leaching time increased from 0 to 300 s. With a 10 mA cm^2 HER overpotential, the enhanced Ni–P electrocatalyst functioned adequately. Additionally, a PEMWE single cell analysis showed that the improved Ni–P cathode performed efficiently. These findings demonstrate an effective approach for generating Ni–P cathodes that can be adapted to fabricate alternative transition metal-based cathodes.

6.2 Use in energy storage: supercapacitor and battery applications

Two crucial parameters that are indispensable for energy storage electrode materials are the abundant porosity and large specific surface area to ensure maximum exposure to electrolyte charges. DHBT provides an excellent pathway for deriving fluffy, high-surface-area Cuf that is suitable for holding the charge and also allowing the expansion of the foam structure during cycling, making it specifically suitable for increasing the shelf life of the electrode. The utilization of DHBT-derived 3D Cuf for various electrochemical energy storage applications is categorized here according to the specific roles in the fabrication of the storage electrode, such as (a) active electrode materials,[190–192] (b) 3D scaffolds or templates and (c) conductive substrates or current collectors.[193,194]

6.2.1 As supercapacitor electrodes

6.2.1.1 As an active electrode material. Exploiting Cu(II)/Cu(0) as a reversible redox centre in aqueous media for charge storage, dendritic Cuf has been utilised as an active electrode material to demonstrate pseudocapacitive behaviour. Mirzaee *et al.* reported thin nanostructured Cuf with different morphologies and grain sizes *via* DHBT and investigated the

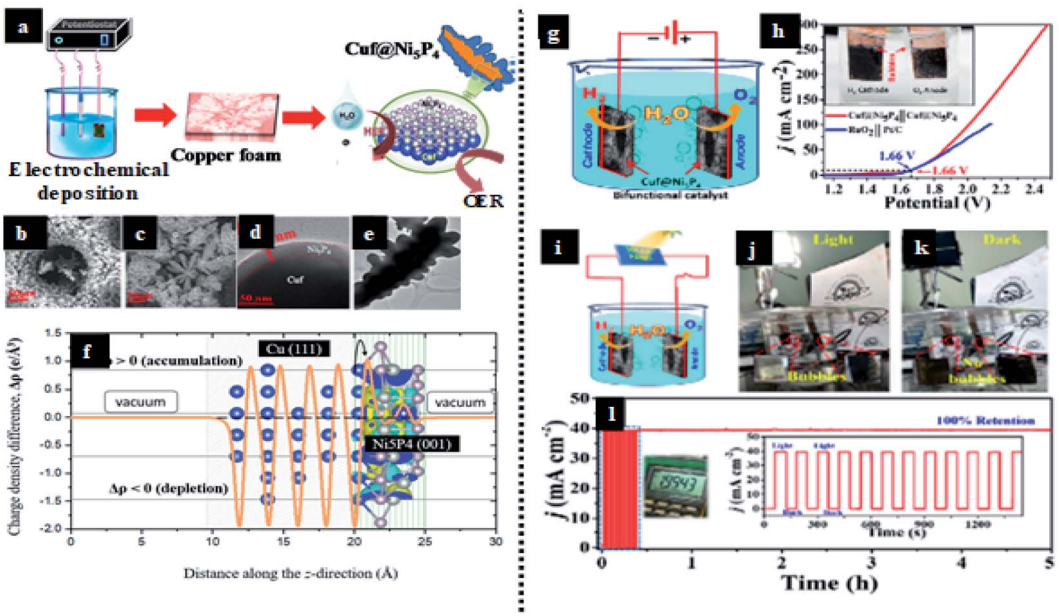

Fig. 11 (a) Schematic illustration of the synthesis of Cuf@Ni_5P_4. (b) SEM images of the prepared core–shell nanostructure of Cuf@Ni_5P_4 at different magnifications. (c and d) TEM image of Cuf@Ni_5P_4 showing the contrast for the formation of the core–shell nanostructure. (e) Illustration of the core–shell nanostructure of the sample. (f) Charge density difference and charge transfer at the interface between the Cu (111) and Ni_5P_4 (001) surface. Reproduced with permission from ref. 10. Copyright 2019, Royal Society of Chemistry publishing group. (g) Schematic representation of the assembly of Cuf@Ni_5P_4 in a two-electrode system. (h) LSV for Cuf@Ni_5P_4||Cuf@Ni_5P_4 and Pt/C||RuO_2 for HER and OER in a two-electrode system. The inset depicts the digital image of the assembly. (i) A schematic diagram of a two-electrode system of the catalyst generating H_2 and O_2 driven by solar cells. The formation of bubbles on the surface of the catalyst when the solar cell is (j) illuminated, (k) when the solar cell is de-illuminated. (l) The on–off response of the catalyst under the exposure, as well as non-exposure of the solar cell with light and *i–t* run for 5 h under continuous illumination of the solar cell. Reproduced with permission from ref. 28 and 180, copyright 2020, American Chemical Society.

crucial role of optimal packing density and specific surface area of the Cuf on its supercapacitive performance.[190] To tailor the dendritic deposits and to control the porosity of the thin foam, they used acetic acid as a hydrogen bubble stabilizer. The obtained Cuf was made up of multiple nanostructured dendritic walls, with sizes less than 1 μm and interconnected pore sizes in the range of 20–50 μm. The optimum Cuf architecture obtained in 0.4 M $CuSO_4$ and 0.1 M acetic acid at 3 A cm^{-2} for 20 s exhibited the highest specific capacitance (C_{SP}) of 102.7 F g^{-1} with a capacitance retention of 90% after 6000 cycles (20 mA cm^{-2}). The cycling stability was slightly improved when the solo Cuf was replaced with a bimetallic Ni–Cuf as the active material. Interestingly, in another reported analysis by Eugenio *et al.*, a porous Ni–Cu metallic foam with randomly distributed nearly circular pores and an open dendritic structure was deposited on stainless steel following a similar cathodic deposition technique. Here, the reversible redox reaction of Ni^{3+}/Ni^{2+} was responsible for the emergence of the pseudocapacitance. However, the overall capacitance included the capacitive contribution from the Cuf backbone and showed a C_{SP} of 105 F g^{-1}, with a cycling stability of 90% after 10 000 cycles for the active material obtained at 1.8 A cm^{-2} for 180 s.[195] Moreover, with the thermal conditioning of such bimetallic foams at 150 °C, Lange *et al.* showed remarkable improvement in the capacitive storage of an electrodeposited Cu–Fe foam.[196] The highest C_{SP} of 297 F g^{-1} and moderately good cycling stability of 66% after 8000 continuous cycles were achieved due to the synergistic impact of both Cu and Fe in nanostructured metallic foam. According to Abdelfatah *et al.*, with increasing current density, the polarization resistance can be further decreased, resulting in the improved capacitive response of the bimetallic foam.[192] A Ni–Cu electrodeposited layer obtained at 2 A cm^{-2} for 30 s exhibited pseudocapacitive behaviour with an acquired C_{SP} of 211.7 F g^{-1}. These examples demonstrate that DHBT-derived Cuf has the potential to be utilised as the active material for supercapacitors with sufficiently good performance. However, there is still scope for including more chemistry to precisely calibrate the nanostructure and redirect their applications in other fields of energy storage systems.

6.2.1.2 As a 3D template or scaffold. 3D Cuf scaffolds are used as templates for self-assembling or directly growing other nanostructured materials, such as metal-oxides, few-layer graphene or graphitized carbon, carbon nanotubes, *etc.*, *via* various techniques. As promising electrode materials with faradaic pseudo-capacitors based on aqueous electrolytes, a variety of transition metal oxides, particularly RuO_2, NiO, MnO_2, Co_3O_4, or CuO, have been explored.[197–201] CuO has recently attracted the interest of researchers owing to its minimal cost, abundant potency, lack of toxicity, and ease of production. The geometry and particle size of CuO significantly influence its specific capacity. As a consequence of its unique characteristics as well as a wide range of possible applications, a variety of techniques have been employed to synthesize nano-sized CuO powders exhibiting different morphologies. Typically, CuO powder is usually blended with conductive carbon substituents or polymer binders to develop a paste, which is then applied to current collectors, particularly as metal foils, to prepare electrodes for Li-ion batteries or supercapacitors. Owing to inaccessible regions to the electrolyte solution and inadequately governed porous architecture, those electrodes often have limited active material consumption. In contrast to powder electrodes, nanowire array electrodes possess a larger electrochemical active surface area and improved utilization of active materials with better diffusion capabilities. Li *et al.* developed a pseudocapacitive CuO/Cuf electrode by a simple anodization technique that delivers a C_{SP} of 212 F g^{-1} with 85% of the initial capacitance retention after 850 cycles.[202] Here, Cuf acts as both a template to grow the CuO nanostructure as well as the

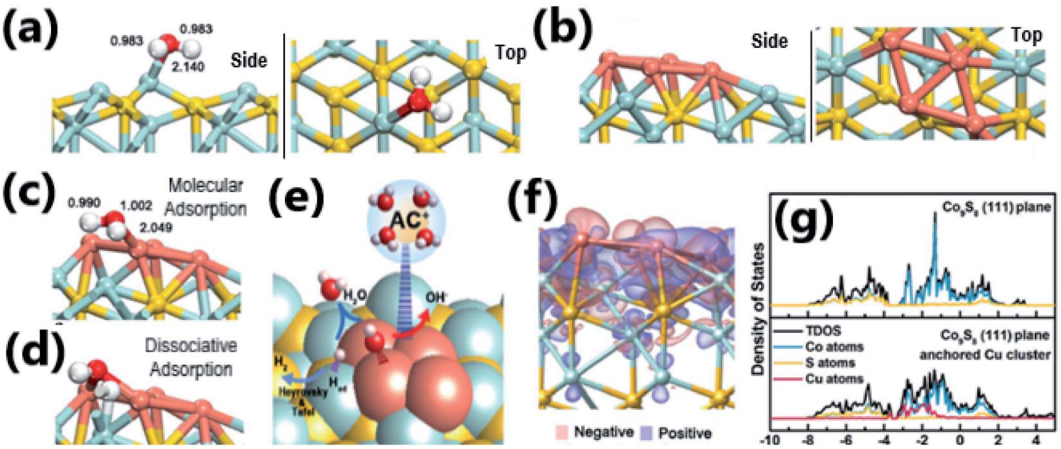

Fig. 12 (a) Augmented structure of water molecule adsorption on the Co_9S_8 (111) surface. (b) Optimized structure of a four-atom Cu cluster stabilized on the Co_9S_8 (111) surface. (c) The charge density difference in the heterogeneous interface of the Cu-cluster@Co_9S_8; red and blue regions represent electron accumulation and depletion, respectively. (d) Computed density of states (DOS) of the Co_9S_8 (111) plane with and without Cu cluster. (e) Optimized structure of water molecular adsorption on the Cu-cluster@Co_9S_8 (111) plane. (f) Optimized structure of water dissociative adsorption on the Cu-cluster@Co_9S_8 (111) plane. (g) Schematic illustration of water reorientation and dissociation on the Cu@CoS_x/CF surface. Reproduced with permission from ref. 13, copyright 2017, Wiley-VCH.

substrate for the active electrode material. Another easy and low-cost strategy was reported by Dey *et al.*, where the active material (graphene oxide, later reduced) was drop cast on the 3D Cuf template. Here, the honeycomb lattice of Cuf acted as a template for the three-dimensional self-assembly of rGO and later acted as a substrate for the fabrication of a binder-free, self-supported supercapacitor electrode in aqueous solution.[1] Fig. 13a–n highlights the remarkable changes in the surface morphology of the 3DrGO material at various positions of the 3D Cuf nanopore walls, which support the self-assembly of the active material wrapped around the template. However, the mechanical adherence of the self-assembled rGO film to the Cuf honeycomb lattice was deemed not very suitable for long cycling hours. Therefore, in a later work, they utilised these porous films as a support structure for further modifications by electrodeposition. Purkait *et al.*[130] reported a conformal deposition of electrochemically reduced GO thin films on top of the DHBT-derived Cuf networks on a Cu wire. The technique helped to improve the mechanical coherence and decrease the contact resistance between the two electrodeposited films while maintaining the structural integrity and enhancing the high surface area of the underlying honeycomb lattice. The advantage of the developed deposition technique was reflected in the excellent flexibility of the wire-based supercapacitor, which was demonstrated by assembling it in different geometries and bending angles with/without a flexible substrate for applications in smart textiles and wearable devices.

Moving forward to more sophisticated techniques, researchers have preferred to use the 3D Cuf scaffold only as a template for developing 3D active electrode materials for supercapacitor applications and not use it as a substrate as well. Jeong *et al.* synthesized a porous hydrous RuO_2 on a Cuf template, which exhibited a specific capacitance of 809 F g^{-1} and good stability of 98% retention during the 3000th cycle.[203] For the technological relevance of the proposed synthesis technique at the industrial scale, the authors highlighted that along with the simplicity of the DHBT technique, the electrochemical dealloying of the Cuf scaffold also allows for the fabrication of a clean and durable nanoporous film, which gives a competitive performance when compared to sol–gel or hydrothermal processes. To avoid the continuous exposure of Cuf to the aqueous electrolytic solution and minimize the effect of metallic corrosion on the long-term stability of the supercapacitor, Kamboj *et al.* fabricated a metal-free planar supercapacitor on the Cuf scaffold and later chemically etched it out after electrochemically growing the 3DrGO electrode material.[26] The interconnected porous graphene, obtained *via* the electrochemical deposition and simultaneous reduction process followed by template etching and a unique technique of laser irradiation, possesses a very high electrical conductivity and therefore plays a crucial role as both the active material and the current collector, suitable for the fabrication of a metal-free supercapacitor. An unprecedented cycling stability of 100% retention even after 100 000 continuous charge–discharge cycle

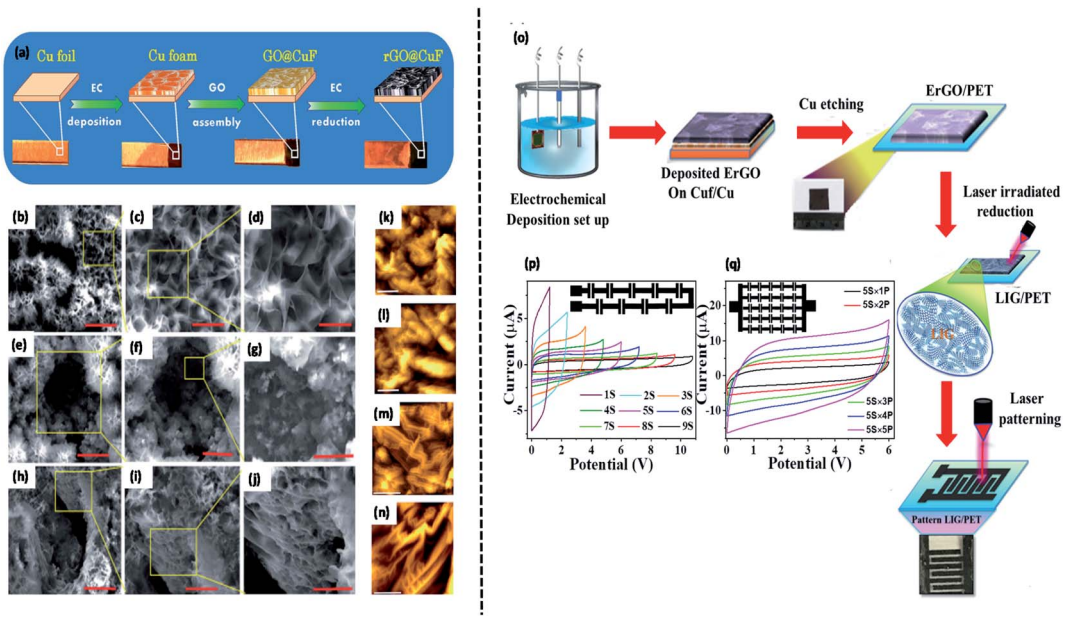

Fig. 13 (a) Schematic illustration of the formation of rGO@CuF; microscopic characterization of three types of structures. SEM images of (b–d) 3DrGO at the boundary of Cuf, (e–g) 3DrGO inside the pore of Cuf and (h–j) 3DrGO on the wall of Cuf. Scale bar: (b) 50 μm, (c) 10 μm, (d) 5 μm, (e) 50 μm, (f) 20 μm, (g) 10 μm, (h) 50 μm, (i) 20 μm and (j) 10 μm, high-resolution microscopic structures. AFM (k and l) images of 3DrGO-CuF on Cu supports. (m and n) High-resolution images. Scale bar: (k) 5 mm, (l) 5 mm, (m) 2 mm and (n) 0.5 mm. Adapted with permission from ref. 1, copyright 2015, Royal Society of Chemistry. (o) Schematic representation of the electrochemical synthesis followed by laser-irradiated reduction used for the preparation of LIG-MSC. CV response of the electrode arrays of the linear MSCs (p) connected in series (1S to 9S) and (q) arranged in $mS \times nP$ ($m = 5$ and $n = 1$ to 5) conFig.d module, where m = number of cells in series and n = number of cells in parallel, at a scan rate of 100 mV s^{-1}; the inset shows the schematic for the cell arrangements. Reproduced with permission from ref. 26, copyright 2019, Royal Society of Chemistry.

was the highlight of the current study, which was achievable not only because of the improved conductivity of the LIG film, but also because of the removal of the 3D metallic Cuf template as shown in Fig. 13o–q.

6.2.1.3 As a current collector. The *in situ* growth of various nanostructures, for example, metal oxides on the conductive core of electrodeposited Cuf, is a significant step towards increasing the overall electrical conductivity of the storage system, consequently increasing the charge storage performance. In this regard, Kang *et al.* reported the deposition of ultrathin nickel hydroxide on carbon-coated 3D electrodeposited Cuf structures for high-performance supercapacitors.[193] The 3D-Ni$(OH)_2$/C/Cuf exhibited a high specific capacitance of 1860 F g^{-1} at 1 A g^{-1}, approaching the theoretical capacitance of Ni$(OH)_2$ material. It also exhibited superior cycling performance, with 86.5% capacitance retention after 10 000 cycles revealing the importance of using the electrodeposited Cuf base as a substrate.

6.2.2 As anode material for rechargeable batteries. LIBs have the greatest potential of the high-energy battery materials currently available on the market. However, the high activity of Li metal, large volume changes and consequent Li dendrite formation have severely impacted its performance in the recent past. Therefore, finding an alternative host to improve the performance of the Li-metal anode has become a key challenge. The utilization of DHBT-derived Cuf as a reticulate 3D substrate with uniform porosity has been explored by several research groups for the following reasons: (1) it can reduce the local current density, (2) suppress the mossy growth of Li and, most importantly, (3) buffer the volume change in Li-metal anode. Additionally, the low specific capacity of the conventional graphite-based anodes, or the poor electrical conductivity of typical metal-oxide based anodes, limits their applications in rechargeable lithium-ion batteries (LIB) and therefore honeycomb-like Cuf were used in some applications for the LIB anodes as an alternative to graphite anodes. Porous Cuf, deposited *via* DHBT has been used as an active material or as a substrate along with Sn or Sn-based intermetallic materials.

Electrodeposited Cu–Sn alloy foams (Cu_6Sn_5) were designed by Shin *et al.* to be used as a negative electrode for LIBs, which delivered a reversible capacity of about 400 mA h g $\pm$ 1 up to 30 cycles as well as a superior rate capability; even at a rate of 20C, the electrode was successfully able to retain 50% of its capacity at 1C.[204] Later on, Tan *et al.* developed similar material, for application as an anode in LIBs, that showed a significant improvement in the cycling stability, with ~50% retention after 50 cycles. They were characterized by fast mass transports and rapid surface reactions.[205]

The DHBT-derived Cuf was also used as a substrate along with Sn-based intermetallic materials, as compared to a simple Cu foil, in some examples. Kwon and co-workers explored the effects of Cu substrate morphology and post-electrodeposition treatments on the porosity and mechanical strength of the Cuf electrodeposits and studied its applications in LIBs in several research findings.[206] They have shown that with the adjustment of the Cu electrodeposition conditions, the morphology can be controlled and both grape-like and dendritic Cuf substrates can be obtained, with the grape-like deposits being more structurally sound during cycling. In another work, Si was first deposited onto porous Cuf to demonstrate the importance of a porous substrate in battery anodes. Suk *et al.* reported a unique 3D porous Si/Cuf, by means of a two-step electrodeposition process, for direct application as anodes in LIBs without adding other conductive additives and binders.[207] They demonstrated superior improvement of the cycling lifetimes and rate performance of the fabricated LIB. This method was also later adopted by Dogan *et al.* who explored electrodeposited Cuf as a substrate for a thin-film silicon electrode as a novel anode material for LIBs.[128] The binder-free electrode exhibited a highly reversible and stable specific capacity of 1000 mA h g^{-1} at a current density of 0.08 A g^{-1}. Another unique example was highlighted by Nam *et al.*, where improved electrochemical performance was observed for an electrodeposited Sn–Cu anode for LIB due to an *in situ* phase transition of Sn, leading to Sn–Cu_6Sn_5/Cuf at the interface and countering the volume expansion of the electrode materials, resulting in improved stability.[206] Umh *et al.* designed a Cu dendritic superstructure with macropores as an anode-free 3D current collector, which can significantly improve the electrochemical plating/stripping behaviour of Li.[194] The anode can operate for more than 600 h without a short-circuit and exhibits a low level of voltage hysteresis (~20 mV), promoting the superiority of the Cu dendritic superstructure that helps to achieve an anode area without any uncontrollable Li dendrites. Qiu *et al.* similarly used a DHBT-derived 3D porous Cuf architecture as the current collector for the Li-metal anode to curb its dendritic overgrowth and buffer its irreversible volume change.[208] A very highly stable coulombic efficiency was achieved with this arrangement at different specific current densities (0.5, 1 and 2 mA cm^{-2}) with a capacity of 1 mA h cm^{-2}, even after 250 cycles. Interestingly, the symmetric battery cells exhibited enhanced cycling performance, up to 700 h with low and stable voltage hysteresis, at the current density of 1 mA cm^{-2} with a higher capacity of 3 mA h cm^{-2}, supporting its potential for practical applications. It was observed that with thicker deposition walls of Cuf, less Li was deposited on the surface, leading to the superior performance of the LIB. These examples demonstrate that utilising DHBT-derived Cuf is possibly the most efficient way to create substantial Cu current collectors for LIB technology with increased surface area (3 times greater capacity as compared to smooth Cu foil)[209] and for mitigating the issue of Li dendrite formation.

In addition to LIBs, Cufs are also explored as substrates for application as Na-ion battery anodes as well. Using electrodeposited Cuf as the substrate, a 3D porous Sb/Cu_2Sb electrode was prepared by Nam *et al.* to improve the cycle stability and rate capability of the anode material. The charge capacity was sustained at 485.64 mA h g^{-1} over 120 cycles with a high coulombic efficiency of 97%, and the charge capacity retention was approximately 70% of the capacity at 0.1C rate, even at a high 3C rate.[210]

6.2.3 As an electrode material for metal–air batteries. The honeycomb network of the dendritic Cuf makes them particularly sensitive in order to overcome the sluggish reaction

kinetics of both the above-mentioned surface-confined processes with desired morphology, ample active sites and, therefore, lower overpotential, high electrochemically active surface area and higher limiting current density. Kim *et al.* fabricated a metal–carbide (Cu–C_x) layer on electrodeposited Cuf in order to provide efficient catalytic active sites and lower the binding energies for electron transfer in both the ORR and OER.[211] They argued that the dendritic base of the Cuf provides an enriched catalytic surface and the protective metal–carbide layer offers an appropriate O binding energy and durability of Zn–air batteries. In some cases, the metal anodes of the metal–air batteries also call for modifications to improve the stability of the battery device as a whole. Recently, Mutlu *et al.* came up with an innovative solution of using dendritic Cu as an efficient and economical solution to improve the anode efficiency of the Al–air batteries by protecting them from severe corrosion and without hampering the anode reactions.[212] They concluded that the alloy/electrodeposited Cu-anode had a finer microstructure than the pure Al itself, which resulted in better activity. Table 2 summarizes the contemporary literature reports on the applications of electrodeposited Cuf in electrochemical energy storage systems, as discussed above. It can be concluded from the above discussion that DHBT-derived Cuf has multifaceted application potential in the field of electrochemical energy storage. From an industrial point of view, smooth Cu foils or commercial 3D Cu foam are abundantly used as a current collector for battery materials. However, DHBT-derived Cuf has the added advantage of key structural and electronic properties that significantly enhance the storage performances (capacity, cycling stability, *etc.*) of these devices.

6.3 Use in electrocatalysis

Since the concept of electrocatalysis was established, it was believed that only a handful of expensive and scarce noble metals, like Pt, Ir, Ru, *etc.*, could effectively lower the overpotential of many important electrochemical reactions. It was assumed that their reactivity could not be replaced *via* base metals.[213] However, recent progress in nanomaterial design has successfully addressed this issue and among a myriad of contemporary novel materials, DHBT-derived Cuf has stood out as an excellent and flexible catalyst for a wide variety of applications, as discussed below.

6.3.1 Oxygen reduction reaction (ORR). The oxygen reduction reaction acts as an operational backbone for various fuel cells and metal–air batteries. Cu is one of the leading transition metals, essential for its bifunctional use in metal–air batteries.[214,215] Cu in its various forms can be used as both a substrate (Cuf) and active site for oxygen reduction and oxygen evolution processes. Owing to the ease of electrodeposition technique, commercial Cuf can be used to galvanically deposit dendritic Cuf as an essential material for the ORR. The high conductivity, high surface-area and reasonable porosity induced within the structures have been proven to be effective for proper intercalation between the substrate and the reactants facilitating the ORR. However, Cu is often amalgamed with some secondary metals to improve the catalytic activity further. Electrochemically-obtained Ag–Cu dendritic alloy is one of the very first materials to be investigated as an electrocatalyst for the ORR and its subsequent application as a bifunctional air cathode in Zn–air batteries.[216] Here, the focus is particularly on material development for ORR electrocatalysis, instead of metal–air batteries. Cuf was even used as a template in some studies for fabricating other noble metal foams. For instance, an attempt was made by Xiong *et al.* where a nano Pd–Cu catalyst was prepared with Pd on porous Cu by the galvanic replacement technique.[9] The surface morphological characterization of electrodeposited copper foam has been depicted in the SEM and TEM images in Fig. 14a–c, where the pore size of the foam is 20 μm and the Cu nano-dendrites have a wall thickness of 5–10 μm. When a galvanic replacement method was carried out between Pd^{2+} and superficial copper, the sharp outline of the Cu dendrites became gentle and the surface roughness increased with numerous nano-lands of Pd particles as evident from the SEM and TEM images of the coral-like Pd–Cu bimetallic porous structure (Fig. 14d–f). The Pd nanoparticles exposed on the copper surface provided the active sites for oxygen reduction. This 3D catalyst exhibited an impressive oxygen reduction peak current of 17.4 mA cm^{-2} and the oxygen reduction amount (ORA) was 17.1 mC as compared to 1.2 mC for commercial Pt/C, indicating a 14-fold increase in electrocatalytic activity. Since the electrochemical redox potential for Cu^{2+}/Cu is +0.337 V, any other noble metal salts other than Pd having a more positive reduction potential than Cu could be used for this technique. The choice of the metals would decide the potent application of the copper foam galvanostatically replaced with noble-metal foam electrocatalyst. More impressively, as per the reports by Jin *et al.*, surface-roughened Ag–Cu (1 : 1) nanoplatelets, synthesized by the electrodeposition technique exhibited high performance towards the ORR and hence potent usefulness in primary and secondary Zn–air batteries.[20] The surface micrographs of the nanostructures are depicted in Fig. 14g–i. A very distinct ORR peak at −0.3 V (*vs.* saturated calomel electrode) was observed, corresponding to the developed material, as shown in Fig. 14j. Although the catalyst have shown not very satisfactory performance for ORR with an over potential of 0.68 V *vs.* RHE in 0.1 M KOH, but exceeded pure Ag and Cu catalysts shown in Fig. 14k and l. The highlight of the work is that by this synthesis technique, highly crystalline Ag–Cu alloyed particles were formed where both Cu and Ag remained in the metallic state, being resistant to oxidation. With alloying, the ligand effect between Ag and Cu and d-band shifting near the Fermi level benefitted the ORR with an effective electron transfer number of 3.9 from the catalyst surface towards oxygen. This synthetic technique can be explored widely by the amalgamation of Cu with cheaper transition metals for even better performance towards the ORR with improved catalytic stability. This would thereby prevent the chances of catalyst degradation or demetallation during the continuous hours of the ORR.

6.3.2 Nitrogen reduction reaction (NRR). Cu is among the late transition metals having a significant number of d-electrons that facilitate reduction reactions involving greater electron transfer numbers. However, the 6-electron-proton

Table 2 Summarized key electrochemical performance parameters of various contemporary Cuf-based materials for energy storage applications

Material	Storage application	Electrolyte	Cell voltage	C_{SP}/specific capacity	Energy density	Power density	% retention/% coulombic efficiency (cycle number)	Ref.
Active electrode material								
Cuf	Supercapacitor electrode	6 M KOH	0.6 V	95 F g^{-1} @ 1 mA cm^{-2}	—	—	90% @ 20 mA cm^{-2} (6000)	190
Ni–Cuf	Supercapacitor electrode	1 M KOH	1 V	105 F g^{-1} @ 1 mA cm^{-2}	—	—	90% @ 10 mA cm^{-2} (10 000)	195
Ni–Cuf	Supercapacitor electrode	1 M H_2SO_4	0.7 V	212 F g^{-1} @ 2 mA cm^{-2}	29.4 W h kg^{-1}	52 kW kg^{-1}	—	192
Si/Cuf	LIB anode	1 M $LiPF_6$	1.6 V	2824 mA h g^{-1} @ 0.1C	—	—	99% @ 0.1C (100)	207
Ni–Cu	Supercapacitor electrode	1 M KOH		11.73 F g^{-1} at 2 mA cm^{-2}	29.4 W h kg^{-1}	52 920 W kg^{-1}		272
As three-dimensional template								
rGO@Cuf	Supercapacitor electrode	1 M PBS	0.6 V	623 ± 7 F g^{-1} @ 1 A g^{-1}	31 W h kg^{-1}	0.3 kW kg^{-1}	99% @ 10 A g^{-1} (2000)	1
pErGO@Cuf	Symmetric supercapacitor	1 M PVA/H_3PO_4	1 V	81 ± 3 F g^{-1} @ 0.5 A g^{-1} 283.5 mF cm^{-2}	11.25 W h kg^{-1} 39.3 μW h cm^{-2}	5 kW kg^{-1} 17.6 mW cm^{-2}	94.5% @ 5 A g^{-1} (5000)	130
LIG-MSC	Symmetric supercapacitor	1 M PVA/H_3PO_4	1.2 V	2.32 mF cm^{-2} @ 10 μA cm^{-2} 3.3 F cm^{-3} @ 40 mA cm^{-3}	459 μW h cm^{-2} 0.65 W h cm^{-3}	0.57 W cm^{-2} 822 W cm^{-3}	100% @ 0.17 mA cm^{-2} (100 000)	26
Ni–Co–Cu-sulfide	Asymmetric supercapacitor	6 M NaOH	1.6 V	1203.75 F g^{-1} @ 1.0 mA	64.3 μW h cm^{-2}	16 mW cm^{-2}	84% (1000)	273
TRAB-P	Ammonia-based batteries	2 M NH_4OH	0.211 V *vs.* SHE			102 W m^{-2}		274
As substrate or current collector								
3D-$Ni(OH)_2$/C/Cuf	Supercapacitor electrode	1 M NaOH	0.8 V	1860 F g^{-1} @ 1 A g^{-1}	147.9 W h kg^{-1}	37 kW kg^{-1}	86.5% @ 200 A g^{-1} (10 000)	193
Li/Cuf	LIB anode	1 M LiTFSi	1 V	1 mA h cm^{-2} @ 0.5 mA cm^{-2}	—	—	95% @ 0.5 mA cm^{-2} (140)	194
Sn/Cuf	LIB anode	—	1.5 V	567 mA h g^{-1}	—	—	90% (30)	43
Li/Cuf	Li anode	1 M LiTFSi					98% (250) @ 0.5 mA cm^{-2}	208

transfer reaction (nitrogen reduction reaction) is more sluggish, both kinetically and thermodynamically, as compared to its competitive counterpart, that is the hydrogen evolution reaction. Mostly within the voltage window of the NRR, the HER gets preference due to the greater adsorption tendency of protons over N_2 on the catalyst active site. However, having a local electron sufficiency on the electrode surface renders better charge transfer kinetics of the NRR. This concept was adopted by Li *et al.*, where they have shown that the abundantly oriented nano-spikes of dendritic Cu on carbon paper (Cu/CP) are extremely responsive to nitrogen reduction.[11] The crystal lattice present in Cu/CP is highlighted in the XRD pattern in Fig. 15(a), while the surface micrographs are revealed in Fig. 15(b and c). The architecture enhanced the interaction between the electrocatalyst surface and the reactant and hence in 0.1 M HCl, they have achieved a high FE of 15.12% and a large NH_3 yield rate (V_{NH_3}) of 25.63 mg h^{-1} mg_{cat}^{-1} at −0.40 V *vs.* the RHE with their designed electrocatalyst, as exhibited in Fig. 15(d–g). Nevertheless, this DHBT-derived Cuf is extremely prone to superhydrophilicity, which facilitates the HER on its surface owing to almost zero contact resistance with the electrolyte. Therefore, it is better to modulate the surface of Cuf catalyst with coatings or functionalizations, which would be beneficial for inducing N_2 into the solid–liquid–gas three-phase interphase. It is a very controversial issue to date regarding whether one should develop catalysts with hydrophilic or hydrophobic properties and there have been enormous reports for both methods. For example, the surface functionalization of Cuf with hydrophilic groups like –NH_2 or –OH could provoke hydrophilicity, while surface coating with polymers or long-chain hydrophobic thiols could induce hydrophobicity. This issue needs to be thoroughly resolved and thus, there is still ample room for exploration in this direction of the electrodeposited Cuf as an active material or a self-standing support for the active material to effectively yield ammonia at a much lower overpotential.

6.3.3 Carbon dioxide (CO_2) reduction (CO_2RR). The accelerating rate of increase in global CO_2 emissions since the age of industrialization has led to an increase in the average temperature and unpredictable climatic changes.[217,218] The utilization of excess of CO_2 for value-added fuels and chemicals has evolved as a promising and emergent field for research that will help to establish a sustainable environment. The electrochemical reduction of CO_2 (ECR)[219–221] to various essential compounds is considered as the best method as compared to other available catalysis processes, such as biochemical,[222] photochemical,[4,223,224] thermochemical processes,[225,226] *etc.* Since the ECR can be carried out at ambient temperature and pressure, the energy required for the process can be obtained from renewable energy sources (solar, wind, tide, *etc.*).[227] The ECR being a multiple electron-proton transfer process is quite complex and it goes along with the competitive hydrogen evolution reaction (HER). CO_2 is a non-polar molecule with a double bond so enormous energy is required to break this bond. Therefore, an electrocatalyst is needed that has low overpotential for the ECR and can adsorb gaseous reactants and then easily desorb the reaction products. Studies have shown that several metals like Au,[228,229] Ag,[230,231] Pt,[232] Pd,[233] Zn,[234] Cu,[235–239] Sn,[240] *etc.*, in the form of single metallic foam or their nanostructures supported on conducting materials like graphene, *etc.*, have been used as homogeneous catalysts for CO_2 reduction.[221] Of these metals, Cu stands out as a star performer since it is the only metal that can reduce CO_2 to hydrocarbons.[241] Interestingly, Bagger *et al.* proposed that transition metals in electrocatalysts could be classified into four general categories based on the binding energy of intermediates to the metal surface in the ECR and HER. Copper, on the other hand, has a tendency to develop products even beyond CO[242] since it is the only metal with a negative adsorption energy for CO* (ΔE_{CO*}) but a positive adsorption energy for H* (ΔE_H). Copper can thus reduce CO_2 to products other than CO while suppressing H_2 generation. As a consequence, the morphology and structural variation of Cu and its compounds have been extensively studied. Several nanostructures of Cu, including nanoparticles,[237,243] nanowires,[238] nanocubes,[244] overlayers, foams,[245–247] *etc.*, are under investigation for the reduction process. Owing to porous material properties and defects, three-dimensional Cuf containing dendrites branching out through the walls appears incredibly beneficial in the ECR. However, Cuf roughness is governed by dendritic architectures that promote CO_2 reduction active sites. These 3D nanoporous networks exhibit strong intrinsic conductivity and accelerate electron transport.[248] As a consequence, metal plays a crucial role in the ECR not only because of its chemistry-directing properties but primarily because of its architecture. In an electrochemical cell, CO_2 is reduced at the cathode by utilizing the electrons produced by counter anodic water oxidation. The adsorption of CO_2 molecules on the electrode surface, electron-proton transfer reactions to create C–H bonds, and desorption of the generated products are the three basic steps involved in the mechanism.[249] The first step involves an electron transfer to CO_2 to generate the rate-limiting intermediate CO_2^-. As shown in Fig. 16, this CO_2^- intermediate proceeds through several proton-electron transfer (PET) processes to generate various products including CO, HCOOH, HCHO, CH_4, C_2H_6, *etc.* It is conceivable to have two PET; however, more valuable products are obtained when PET > 2 (ref. 250) but becomes potentially unfavourable. Interestingly, many research has been carried out based on the surface roughening in order to introduce surface defects such as steps and vacancies, to favour the ECR.[251,252] Copper electrocatalysts prepared by electrodeposition with different surface morphologies have shown a huge impact on the ECR activity and its product distribution. Klingan *et al.* did a study to find the reactivity determinants for ECR on Cuf.[253] It was demonstrated that adsorbed CO* precursors on the Cuf surface blocked the sites for H_2 and CH_4 generation. Also, pronounced alkalization near the Cuf catalyst caused limited H^+ supply and therefore, H_2 and CH_4 production became suppressed. This change in pH was shown by the HCO_3^-/CO_3^{2-} equilibrium through *operando* Raman spectroscopy and favoured CO and C_2H_4 formation as they followed pH-independent paths. Owing to the substantial performance losses and decomposition of homogeneous catalysts, heterogeneous catalysts are now being studied in detail but they also render

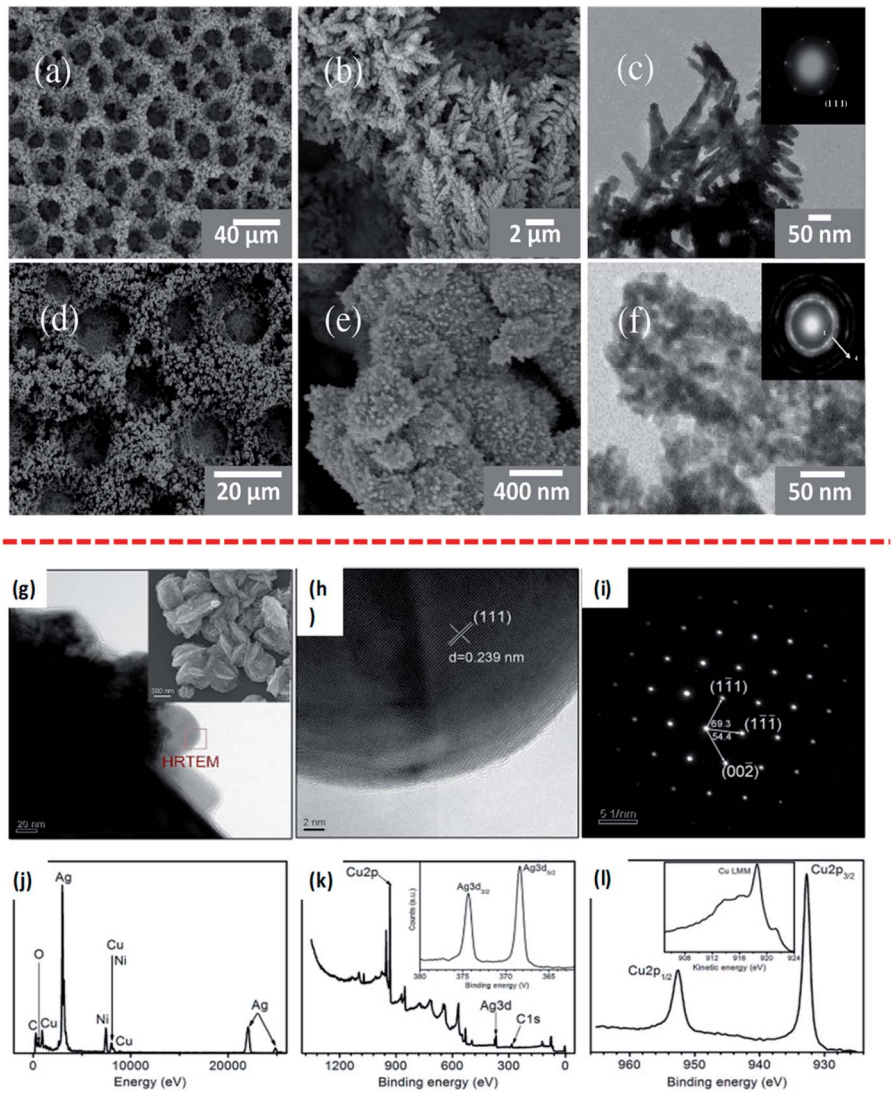

Fig. 14 (a and b) SEM images of the 3D copper foam structure with different scales. (c) TEM images of copper branches, (d and e) the coral-like Pd–Cu bimetallic porous structure after the galvanic replacement, and (f) the Pd–Cu sample after 3 h replacement, with the corresponding SAED patterns (inset). Reproduced with permission from ref. 9, copyright 2013, Elsevier. (g) TEM (inset: SEM), (h) HRTEM, (i) selected area electron diffraction of the $Ag_{50}Cu_{50}$ catalyst. (j) Cyclic voltammograms of the Ag–Cu catalyst in O_2 and N_2-saturated 0.1 M KOH solutions at a scan rate of 10 mV s^{-1}. (k) Mass activity of Ni foam, pure Cu, pure Ag, Pt/C, and $Ag_{50}Cu_{50}$ catalysts in the ORR from RDE polarization curves at 1600 rpm in O_2-saturated 0.1 M KOH solution. (l) Relationship between the catalytic activity and the Cu content in Ag–Cu alloys based on RDE polarization curves at 1600 rpm in O_2-saturated 0.1 M KOH solution. Reproduced with permission from ref. 20, copyright 2015, Wiley-VCH.

determining reaction pathways more challenging. Nevertheless, product activity and selectivity could be improved by modifying Cuf with secondary metals (Sn, Bi, Ag, In). Due to the low cost and significant overpotential of the H_2 evolution, Sn has attracted tremendous interest in this domain. It has been observed that the impregnation of Sn in Cuf has achieved good results and is highly selective for C_1 products. Electrodeposited Sn on Cuf attained FE of ~83.5% for $HCOO^-$ at −1.8 V *vs.* Ag/AgCl,[254] whereas in an optimum electrolyte, the catalyst was stable for 10 hours at −1.1 V with spiky Cu@Sn nanocones over the Cuf surface (Fig. 17a–c) and displayed a maximal FE of 90.4% for formate as shown in Fig. 17d and e.[7] Thus, the high curvature of the nanotips of cones increased the generation of the COO^- intermediate and electron transfer became easy due to the large ECSA. Another Cuf with Sn modification was synthesized by electrodeposition. For the coral-like foam, FE above 90% was produced in the −0.6 to −1.0 V range *vs.* the RHE, with each dendrite possessing both a Cu-core and a CuO_x/SnO_x shell.[255] Palmore *et al.* demonstrated that the hierarchical porosity and surface roughness of Cuf increased the faradaic efficiency (FE) of HCOOH to 26% at −1.1 V *vs.* Ag/AgCl as compared to smooth Cu (<1% at −1.1 V) and propylene was generated for the first on the Cu electrodes reflected in Fig. 17f–j.[16] This may be due to the reaction species being trapped in Cuf pores for a longer time. In order to determine the impact of electrodeposition parameters, a research investigation was carried out. However, the CTAB additive controlled the pore size of the foam. Subsequently, employing Cuf with an additive

enhanced the CO production rate to 11.91 mol h^{-1} cm^{-2} and sustained it above 8.95 mol h^{-1} cm^{-2} for 1 hour.[256] Consequent; *y*, ECR potentially produced specific products by altering the pore diameter, depth, and electrolyte concentration.

On the other hand, a honeycomb-like structure and 3D foam were electrodeposited by Goncalves *et al.* at −1.9 V *versus* Ag/AgCl in 0.1 M $KHCO_3$ and the selective production of C_2 hydrocarbons (C_2H_4 and C_2H_6) was obtained. For CO_2 conversion to C_2 products, electrodeposited Cu with a large active surface area seems preferred.[256] Dutta *et al.* illustrated the high selectivity of Cuf for C_2 production (C_2H_4, C_2H_6) with FE of ∼55% at −0.8 V due to the availability of specific surface sites on Cuf, favouring C–C coupling (dominant 100), which became active by the *in situ* reduction of Cu_2O.[247]

Furthermore, oxide derived (OD) Cuf showed an extremely high current density of ∼9 mA cm^{-2} at −0.45 V *vs.* RHE with FE of ∼39% for CO and 23% for HCOOH due to the synergistic effect between the enhanced surface area of the foam and the preferable reconstruction of low-index Cu facets (100) and (111) that increased the number of metastable active sites.[245] Recently, Cuf accompanied by ionic liquid, 1-butyl-3-methylimidazolium bromide (BMIMB) in the electrolyte accounted for ethanol formation with FE of ∼49%. The stabilization of the intermediates by the aromatic imidazolium ring, *i.e.*, a synergistic effect between Cuf and the utilized BMIMB, favoured C_2 product formation.[257] Thus, apart from the enhanced surface areas, during reconstruction, the preferable formation of low-index Cu facets such as (111) strongly affected the activity and selectivity of the nano-structural Cuf electrode towards CO_2 conversion. However, the selectivity for C_2 products of Cuf grown over the Cu skeleton was observed by the same group in a comparison study between electropolished, annealed and electrodeposited Cu catalyst. Due to the longer mean residence time of intermediates in μm sized pores on Cuf, the electrodeposited Cu electrode achieved the highest FE but this was less than that obtained on Cuf over plane Cu wafers.[258] Likewise, copper oxides have been found to selectively produce C_2 and C_3 products like ethanol, ethylene and *n*-propanol. In a recent study by Dutta *et al.*, advanced *operando* X-ray absorption spectroscopy (XAS), X-ray diffraction (XRD) and Raman spectroscopy studies were conducted to detect the potential-dependent changes that occur in the chemical states of Cu

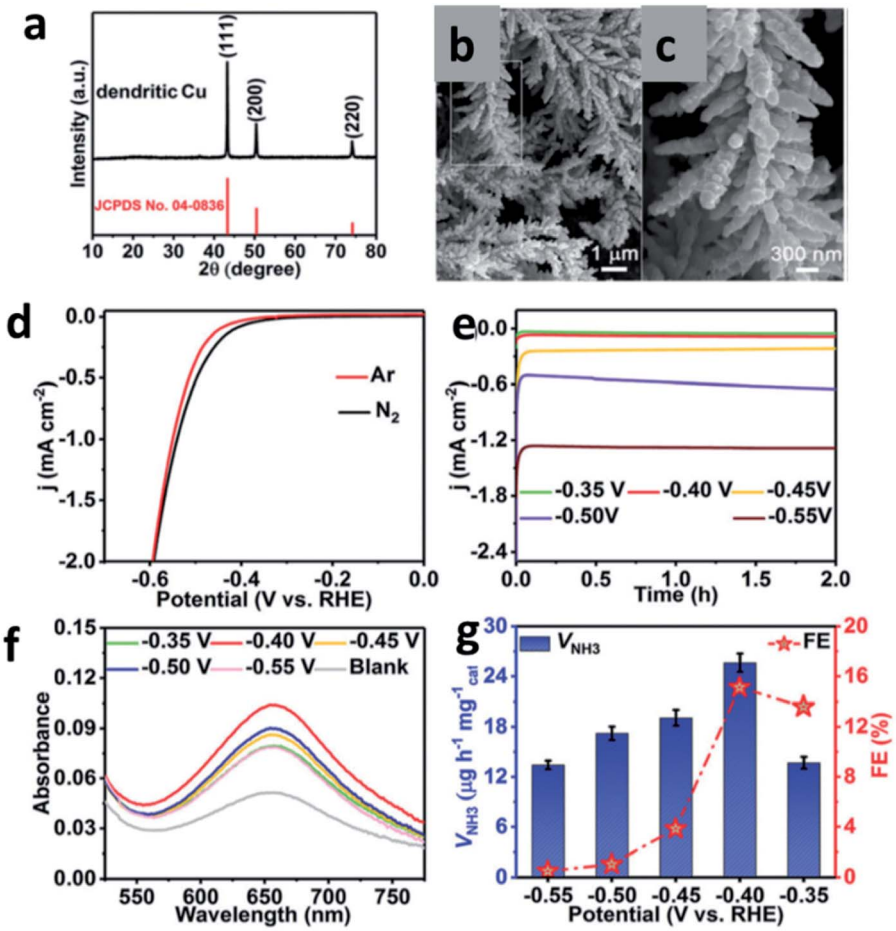

Fig. 15 (a) XRD pattern, (b and c) SEM images of dendritic Cu. (d) LSV curves of Cu/CP in Ar- and N_2-saturated 0.1 M HCl with a scan rate of 5 mV s^{-1}. (e) Time-dependent current density curves of Cu/CP at a series of potentials for 2 h in N_2-saturated 0.1 M HCl. (f) UV-Vis absorption spectra of the electrolytes were obtained after staining with the indophenol indicator after NRR electrolysis at different potentials for 2 h. (g) V_{NH_3} and FEs of Cu/CP for the NRR at different potentials. Reproduced with permission from ref. 11, copyright 2019, Royal Society of Chemistry.

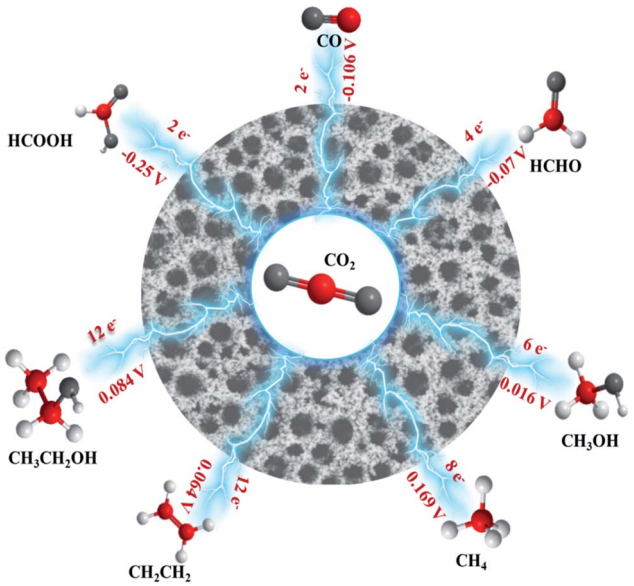

Fig. 16 Schematic illustration representing the various products formed by the change in PET in ECR.

species in the Cu-oxides foams (CuO_x). The bulk-sensitive XAS, XRD, and surface-sensitive Raman spectroscopy revealed that CuO_x foams turned into metallic Cu before hydrocarbon (ethylene, ethane) and alcohol production (ethanol–propanol).[259] This study demonstrates that for alcohol formation on the Cuf surface, a complementary approach to *operando* investigations is needed to obtain a complete view on the potential-induced metal-oxide transition required to activate the Cu catalyst. The substrate and Cuf deposition time have a significant impact on product activity and selectivity. Marepally *et al.* investigated this by using different substrates such as (Cu, Ti, Al, Fe, Fe–Cr–Ni) and carbon-based gas diffusion layer (GDL).[260] Cu–CF_2 seemed to have the highest current density and maximum yield for HCOOH as compared to Cu–CF_1 and Cu–CF_4 due to the existence of a dendritic architecture (related with the fractal dimension), which was absent in the case of Cu–CF_1 and Cu–CF_4. By providing more active sites for CO and CH_4 generation, such as smooth edges and dense surfaces, this improved the overall carbon production rate. For Cu electrodeposited on GDL, the best onset potential (−0.3 V) was obtained with over 80% total carbon FE and close to 60% FE to formic acid. This implies that the nano-morphology and fractal dimensions of the electrocatalyst play a crucial role in electrocatalysis, rather than the chemical nature or presence of certain crystalline planes of the catalyst alone. During CO_2 electrolysis, a change in morphology may occur that causes the deactivation of the electrocatalyst. Such conditions were obtained in the case of pristine and urea-modified Cuf.[246] The addition of urea to Cuf increased the FE of *n*-propanol from 3% to 5% at −0.83 V *vs.* RHE. However, during electrolysis, the cuboctahedral structure of Cuf changed to a dendritic morphology, which led to the deactivation of Cuf. Therefore, more research is needed in this direction to improve the reduction process.

On the other hand, hetero-structured intermetallic Cu_3Sn/Cu_3Sn_5 on Cuf delivered the FE of ~82% for formate at 18.9 mA cm^{-2} for 42 hours,[261] which concluded that the selectivity for formate was obtained due to the stabilization of the HCOO* intermediate as compared to COOH* on the heterogeneous intermetallic surface and the free energy showed that the moderate binding of H* reduced the selectivity of H_2. Recently,

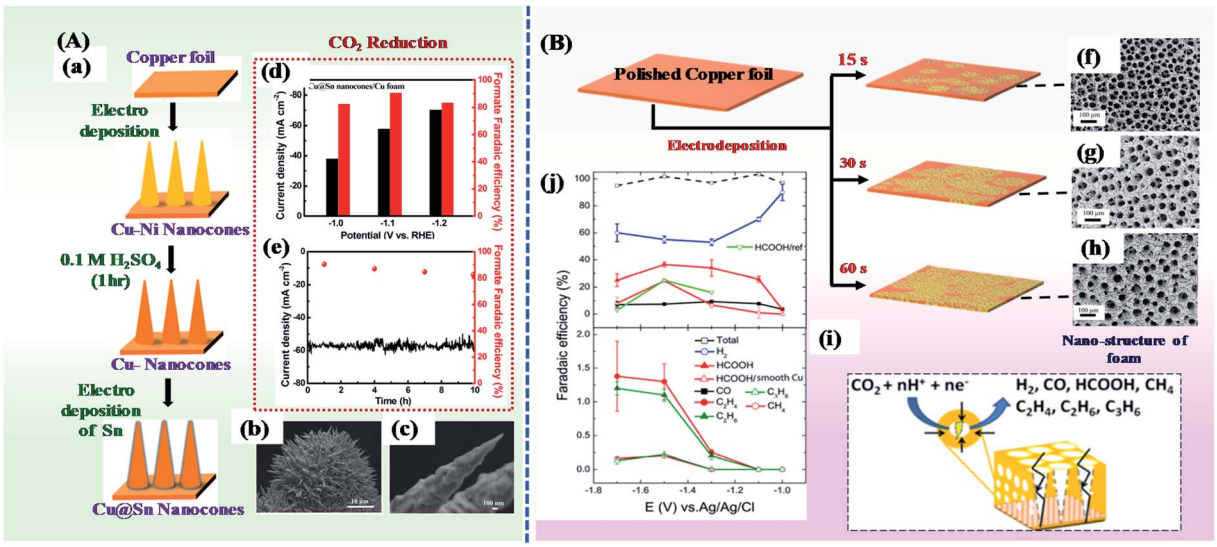

Fig. 17 A (a) Illustration of the steps involved in preparing Cu@Sn nanocones. (b and c) SEM images of Cu@Sn nanocones/Cuf. (d) Current density and formate faradaic efficiency, (e) stability testing of Cu@Sn nanocones/Cuf for catalysing CO_2 reduction at −1.1 V. Reprinted with permission from ref. 7, copyright 2018, Royal Society of Chemistry. (B) SEM images of Cuf on a Cu foil electrodeposited for (f) 15 s, (g) 30 s, (h) 60 s. (i) Scheme presenting the production of different products using Cuf as a catalyst. (j) Product distribution as a function of applied potential during the ECR of CO_2. The working electrode was a Cu nanofoam electrodeposited for 15 s. Reprinted with permission from ref. 16, copyright 2014, American Chemical Society.

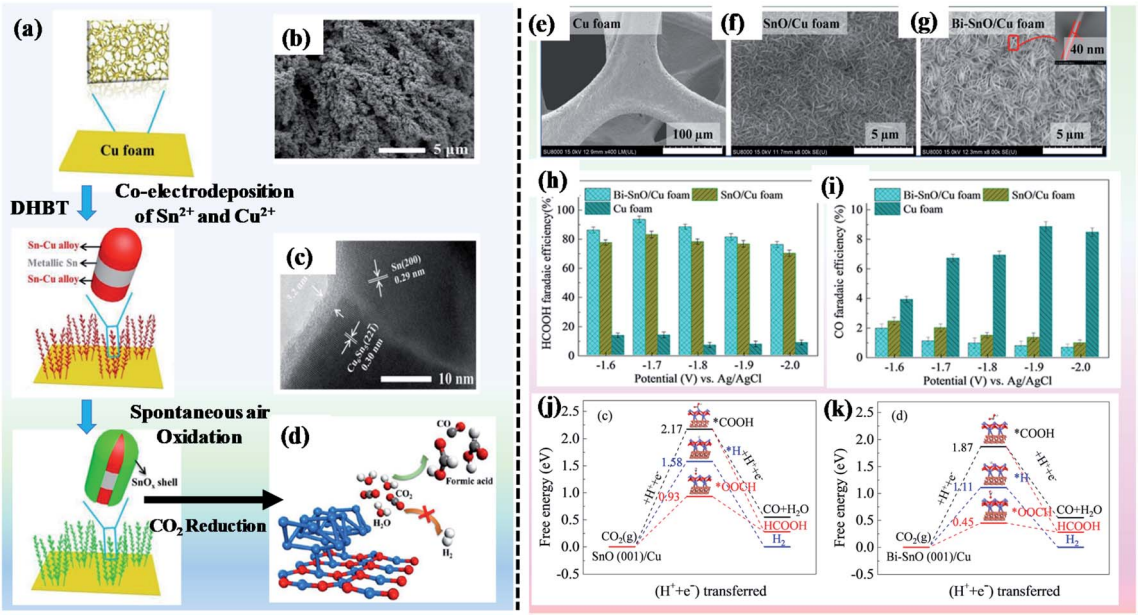

Fig. 18 (a) Schematic diagram of the formation of 3D hierarchical Sn–Cu catalysts on Cuf. (b) SEM image, (c) HRTEM image of $Sn_{2.7}Cu$ catalyst. (d) *In situ* reconstructed Sn/SnO_x interface facilitating formic acid formation. Reprinted with permission from ref. 8, copyright 2020, Wiley-VCH. SEM images of (e) Cuf, (f) SnO/Cuf and (g) Bi–SnO/Cuf electrodes. FE for (h) HCOOH and (i) CO at different potentials for all the catalysts. Free energy diagrams of the conversion of CO_2 into HCOOH, CO and H_2 on (j) SnO (001)/Cu and (k) Bi–SnO (001). Reprinted with permission from ref. 19, copyright 2019, American Chemical Society.

100% FE was achieved by the 3D core–shell porous Cu@Sn hybrid electrode with Cuf as core.[262] By controlling the grain size of Sn on the Cuf surface as the core, the mass activity was increased, which accounted for such high selectivity and FE. Another core–shell model of Cu and Sn, *i.e.*, wheat-like structures of $Sn_{2.7}Cu$ spread uniformly on the Cuf (Fig. 18a–d), showed exceptional behaviour with 406.7 ± 14.4 mA cm^{-2} current density and 98% FE for C_1 products.[8] The *in situ* reconstructions of interface Sn/SnO_x on the Cuf were responsible for the enhanced activity and thus inhibited the HER. The change in the surface composition by tuning Cu and Sn brought the effect of metal on ECR. However, Liu *et al.* demonstrated that the compositions of Cu/SnO_2 and annealed Cu/SnO_2 on the Cuf surface were substantially different.[263] During annealing, the SnO_2 coating broke and atoms on the surface drifted towards the foam holes. As a result of Sn–Cu synergistic actions, it mostly produced CO (70–75%) while HCOOH was created at a low level (5%). Consequently, the amount of metal on the surface influenced the product's selectivity. These findings may help bring 3D-structured electrodes and intermetallic synergy closer to reality. In another work, Guan *et al.* doped Bi into SnO sheets and stabilised HCOO* by lowering its free energy as compared to other catalysts, and also Bi interrupted Sn^{2+} reduction and H_2 and CO generation on the Cuf surface (Fig. 18e–k).[19] Moreover, Zhang *et al.* synthesized Bi NWs on the Cuf, which offered a number of lattice dislocations on the surface and decreased the energy barrier for the intermediates that raised the FE to 95% for formate with a current density of 15 mA cm^{-2} at −0.69 V.[264] This suggested that crystal defect engineering can also be helpful in improving the efficiency of the ECR.

The selectivity for CO is usually shown by noble metals like Au, Ag, because they bind the CO* intermediate loosely so it can be released as gas. In a reported work, Urbain *et al.* demonstrated the enhanced selectivity of Cuf tailored with Ag for CO.[265] The amplified surface area due to Cuf and high selectivity of Ag for CO production raised FE to 95.7% at −0.8 V *vs.* RHE. A novel PtCu alloy foam was proven to be highly selective for *n*-propanol formation with FE ∼ 13.7% and current density = −1.15 mA cm^{-2}, which presented that the selectivity for C_3 alcohol was two times more than C_2 alcohol and the exceptional behaviour was the complete suppression of methanol with the stability of 102 h. The segregated Pd-rich domain played the role of *CO, *H-producer and Cu-rich domain as C–C coupler, which led to the production of alcohol.[266] Interestingly, taking the morphological advantage of Cuf, which provided high ECSA and suppression of parasitic HER by indium (In) along with the selectivity of Ag for the production of CO from CO_2, a nanostructured Ag/In/Cuf was prepared by an electrochemical method. This catalyst exhibited notable performance in CO FE and current density in the low overpotential region.[12] Likewise, a bimetallic Cuf alloy with dendritic foam morphology was used for the reduction of CO_2 to CO at an onset potential of −0.3 V *vs.* RHE with >70% selectivity. The weak binding of CO* on the $Cu_{96}In_4$ foam surface supported the immediate release of CO as the gaseous product (Fig. 19a–m).[12] Likewise, the electrodeposited Ag on the Cuf is highly selective for CO production and the HER was suppressed due to low H* surface coverage.[267] The high Raman adsorption band area showed improved CO selectivity due to the synergistic effect between Ag and Cuf. For comparison, Ahn *et al.* electrodeposited Ag/Cu and Au/Cufs on a Ti substrate for CO production from CO_2. The porous

Table 3 Contemporary literature reports on electrodeposited Cuf and its various derivatives as CO_2 electroreduction electrocatalysts

Catalyst	Electrolyte	Major product	Potential (V)	FE (%)	Current density (mA cm^{-2})	Stability (h)	Ref.
$In_{55}Cu_{45}$@Cu	0.5 M $KHCO_3$	Formate	−0.8 to −1.2 V *vs.* RHE	94.2 ± 2.1%	−8.2 ± 0.4	30 h at −1.0 V *vs.* RHE	275
Cuf	0.1 M $KHCO_3$	C_2H_6, C_2H_4	−1.9 V *vs.* Ag/AgCl	—	—	—	265
Cuf	0.1 M $KHCO_3$	HCOOH	−1.5 V *vs.* Ag/AgCl	37	—	—	16
OD-Cuf	0.1 M $KHCO_3$	CO	−0.45 V *vs.* RHE	39	∼9.4	—	245
		HCOOH		23			
OD-Cuf	0.5 M $NaHCO_3$	C_2 (C_2H_4, C_2H_6)	−0.8 V *vs.* RHE	55	—	—	247
Cuf on Cu-skeleton	0.5 M $NaHCO_3$	C_2 (C_2H_4, C_2H_6)	−1.1 V *vs.* RHE	29.1	—	—	258
Cuf on GDL	0.5 M $KHCO_3$	HCOOH	−0.3 V *vs.* Ag/AgCl	60	—	—	260
Cu_xO foam	0.5 M $NaHCO_3$	C_2H_5OH	−0.77 V *vs.* RHE	6.7	−1.61	—	259
		C_3H_7OH	−0.87 V *vs.* RHE	7.1	−1.72		
Cuf	C_3H_7OH	*n*-Propanol	−0.87 V *vs.* RHE	7.1	−1.72	2	246
Cuf + BMIMB (IL)	0.1 M $KHCO_3$ + 0.04 M IL	C_2H_5OH	−1.6 V *vs.* Ag/AgCl	49	20	—	257
Cuf with CTAB	0.5 M $KHCO_3$	CO	2.5 V	8.6	—	—	256
Sn/f-Cu	0.1 M $KHCO_3$	Formic acid	−1.8 V *vs.* Ag/AgCl	83.5	8	—	254
Cu@Sn nanocones on Cuf	0.1 M $KHCO_3$	Formate	−1.1 V *vs.* RHE	90.4	57.7	10	7
Cu–Sn foam	0.1 M $KHCO_3$	CO	−0.6 V *vs.* RHE	90	7.9	—	255
Heterostructured Cu_3Sn/Cu_3Sn_5 on Cuf	0.1 M $NaHCO_3$	Formate	−0.1 V *vs.* RHE	82	18.9	42	261
	1 M KOH		−0.98 V *vs.* RHE	87	148 (GDE)	—	
3D-core–shell porous Cu@Sn hybrid electrode	0.5 M $KHCO_3$	Formate	−0.93 V *vs.* RHE	100	16.52	15	262
Hierarchical Sn–Cu/SnO_x core/shell catalyst	1 M KOH	C_1	−0.55 V *vs.* RHE	99.0 ± 0.5	243.1 ± 19.2	40	8
Annealed-Cu/SnO_2	0.1 M $KHCO_3$	CO	−1.0 V *vs.* RHE	70–75	8.5	10	263
Bi-doped SnO nanosheets grown over Cuf	0.1 M $KHCO_3$	HCOOH	−1.7 V *vs.* Ag/AgCl	93	12	30	19
Bismuth NWs on Cuf	0.5 M $NaHCO_3$	Formate	−0.69 V *vs.* RHE	>93	16	12	264
Ag–Cuf	0.1 M $KHCO_3$	CO	−0.6 V *vs.* RHE	58.4	1	5	267
Ag–Cuf	0.5 M $KHCO_3$	CO	−0.8 V *vs.* RHE	95.7	10	15	265
Ag–Cuf	0.5 M $KHCO_3$	CO	−0.53 V *vs.* RHE	29.4	—	—	268
Ag/In/Cuf	0.5 M $KHCO_3$	CO	−0.53 V *vs.* RHE	77.4	—	—	12
$Cu_{96}In_4$	0.5 M $KHCO_3$	CO	−0.3 V *vs.* RHE	>70	—	—	276
PtCu alloy foam	0.5 M $KHCO_3$	Propanol	−0.65 V *vs.* RHE	13.7	1.15	102	266
Polyamide modified Cuf	0.1 M $NaHCO_3$	C_2H_4	−0.96 V *vs.* RHE	26	21.2	—	269

structure and low Ag loading mass in Ag/Cuf accounted for the better performance and cost-effectiveness.[268] Another bimetallic AgCu metal foam with segregated Ag and Cu domains was synthesized by an additive-assisted electrodeposition process and activated by thermal annealing for ethanol production.[21] This OD-$Ag_{15}Cu_{85}$ foam presented FE of 33.7% for ethanol and 6.9% for propanol at −1.0 V and −0.9 V *vs.* RHE, respectively, with a stability of 100 h (Fig. 19n–p). The metallic Ag acting as CO producer and Cu as C–C coupler allowed the facile transport of the CO intermediate to those Cu surface sites that were particularly active for C–C coupling and consequently, for ethanol formation.

Other than metals, Cuf can also be modified with polymer-like acrylamide, acrylic acid, allylamine, *etc.*, which particularly give industrial feedstocks like C_2H_4, CH_4 as major products.[269] Among these, poly(acrylamide) was effective in raising the FE for C_2H_4 to 26% at −0.96 V as the key intermediate for C_2 products, *i.e.*, the CO dimer is chemically stabilized by hydrogen bond interactions with the $-NH_2$ group of poly(acrylamide), which is connected to the Cuf surface by its carbonyl group. Although poly(acrylic acid) was also selective for C_2H_4, it was less stable and the poly(allylamine) was particularly involved in the HER. Therefore, Cuf modified with polymer provided a multi-point binding catalytic system that can interplay between the activation and stabilization of intermediates to give a selective product. Cuf has shown great results in terms of homogeneous and heterogeneous electrocatalysis, but for the commercialization of ECR, a lot of work has to be done regarding uncertain reaction pathways, the low solubility of CO_2 in the electrolyte, the stability of the electrocatalyst, *etc.*, and then, we can hope for green energy and a sustainable society.

Table 3 summarizes various electrodeposited Cuf-based electrocatalysts for CO_2RR reported to date.

7. Summary, challenges and future perspectives

In this featured review, we aim to provide the readers with a comparative discussion from different points of view such as synthetic, modifications, structural diversity, and potential electrochemical applications of DHBT-derived Cuf. By careful selection of the appropriate deposition parameters, like bath chemical composition, applied current density, deposition time or temperature, it was shown how the hierarchical open porous morphology of Cuf can be fine-tuned with the desired porosity and thickness of the pore walls. For example, to effectively increase the accessible surface area and enhance the activity of the nanostructured pore walls, it is desirable to have reduced pore size, increased pore density and thinner branches in the foam wall. It has been observed that by adding an optimized concentration of additives, like acetic acid, the hydrophobic forces of the bubbles (template) can be decreased, thus suppressing bubble coalescence and stabilizing the bubble without significantly impacting the morphology of the foam. The one-step, rapid and versatile DHBT technique has proven to be advantageous in terms of material development since it dispenses the most crucial structural and electronic properties that are considered essential in catalysis, energy storage, *etc.* This process has a significant impact on the tuning properties of the nanostructure, which has allowed this field to flourish from a technological point of view. Electrodeposited Cuf is mostly used as an electrocatalyst due to its enhanced surface

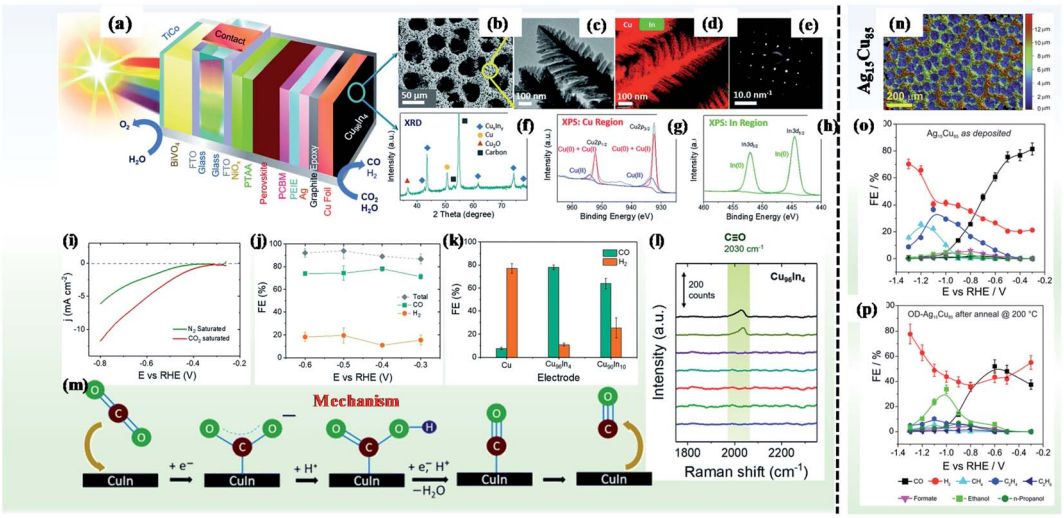

Fig. 19 (a) Literature comparison, (b) low-resolution SEM, (c) high-resolution TEM, (d) STEM mapping and (e) SAED pattern, (f) XRD and (g and h) high-resolution deconvoluted Cu and In XPS spectra of the CuIn catalyst. (i) LSV polarization curve of the catalyst in N_2 and CO_2 saturated electrolyte conditions, (j and k) FE of CO and H_2 produced by Cu_xIn_y alloys carried out in CO_2 saturated aqueous 0.5 M $KHCO_3$. (l) The ν(CO) peak at −0.4 V *vs.* RHE was deconvoluted into a higher frequency band (HFB) and a lower frequency band (LFB) for the $Cu_{96}In_4$ alloy surface. (m) Schematic representation of the proposed mechanism of CO formation on the CuIn surface. Reprinted with permission from ref. 12, copyright 2019, Elsevier. (n) SEM images of the as-prepared $Ag_{15}Cu_{85}$ foam; FE of the different products formed by the catalyst, (o) $Ag_{15}Cu_{85}$ foam and (p) OD-$Ag_{15}Cu_{85}$ foam after annealing, at different applied potentials *vs.* RHE. Reprinted with permission from ref. 21, copyright 2020, Elsevier.

properties that give further scope for modifications. In CO_2RR, the electrocatalyst needs to be selective for the intermediate CO adsorption so that it can successfully compete with the HER and selectively reduce CO_2 to valuable chemicals and fuels with high FE. It has been observed that disoriented surface atoms and superficial crystal lattices are present in the nano structural architectures, which provide an edge effect for the selective confinement of crucial reaction intermediates that are usually unavailable on an open surface like a Cu foil. Cuf has an extensive history of successful applications in the CO_2RR, for the synthesis of C–C or C–N bonds that can produce very useful chemicals such as ethanol, propanol, formic acid, *etc.* The superhydrophilicity and aerophobicity of a freshly deposited Cuf surface have been proven, which are useful in applications like electrochemical water splitting or fuel generation. Additionally, the enormous ECSA of the Cuf surface also helps to achieve higher limiting current density and lower Tafel slope in water splitting, thus enhancing the catalytic performance for the HER or OER. This in a way limits the usage of Cuf in the NRR, as the HER becomes strikingly competitive here. Thus, in the NRR application, Cuf structures are not yet much explored probably because of the selectivity issue. However, surface improvisations could improve the utility of Cuf in this field by favouring the faradaic efficiency for NH_3 production, which would eventually help to attain a better current density for the NRR at a much lower overpotential. In ORR applications, however, Cuf has been reported to have very limited applications, most probably because of the very high overpotential of this catalytic process. Moreover, it was found to be not very selective for oxygen reduction *via* the 4-electron pathway. However, *via* surface modifications with other nanostructured materials, the selectivity for the ORR intermediate can be improved. The contribution of Cuf in the ORR mainly comes from its use as a scaffold or template for other metal (Au, Ag, Pd, *etc.*) foam deposition *via* galvanic displacement, as already discussed in this review article. However, with surface modifications, the faradaic efficiencies for electrochemical ammonia production can be improved in the near future. The versatile Cuf has significant contributions to the electrochemical energy storage applications as well. Here, it is not only used as an active material, but also as a scaffold or template, or sometimes even as a substrate because of its superior electrical conductivity. The porous network also helps in reducing the volume change during cycling experiments, thus improving the stability of the storage devices. In LIB applications, using the electrodeposited dendritic superstructure of Cuf in the anode chamber helps in achieving an anode area without any uncontrollable Li dendrites, therefore nullifying the chances of short circuits. In many supercapacitor applications, the reversible surface redox reactions of Cu^{2+}/Cu^{+} are employed for use as active material. However, the ease of oxidation of the Cuf structure often gets in the way of their commercialization, affecting their rate capacity and stability. Therefore, they are preferably used as templates or scaffolds to produce 3D architectures of carbonaceous active materials that are usually sustainable for capacitive storage purposes.

No progressive technology is interesting enough if not faced with due technological challenges. With all the benefits that a simplified DHBT-derived Cuf provides, it still faces some challenges while deployed in actual practical applications.

(1) One of the major concerns limiting the industrial-scale energy application of the DHBT-derived Cuf is the high cathodic current density required for the deposition itself. In general, the requisite geometrical current density is around 1–10 A cm^{-2}, which indicates that even at a lab scale setup, the conventional instrumentation (potentiostat/galvanostat) needs

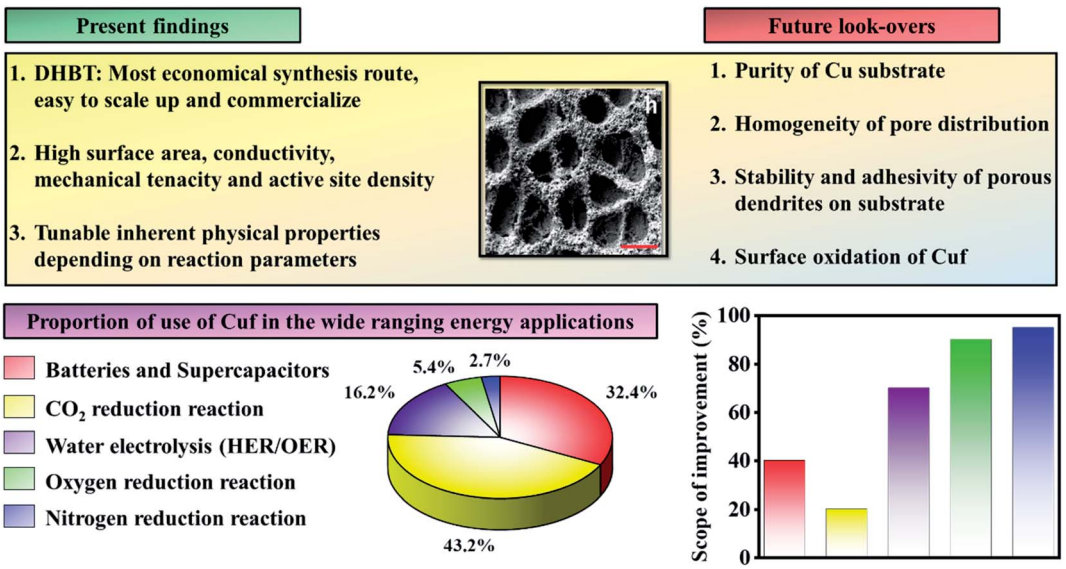

Fig. 20 A potential route for the realisation of the multidimensionality of Cuf and future perspectives to be adopted for the enhanced exploration of the use of this versatile material. The SEM image of the Cuf has been reproduced with permission from ref. 4. Copyright 2014, Royal Society of Chemistry.

to be equipped with a current booster. Since a typical commercial booster allows the modulation of current delivery up to 20 A only, upscaling the process at industrial plants may need specialised equipment. Besides, the implementation of such a high current often involves the side risk of overheating (Joule effect), IR drop and electrical shock, which cannot be ignored. Therefore, the geometrical area optimization of the substrate and suitable additional safety protocols, like electric shock protection or training of handling personnel need to be considered.

(2) Variation in the purity of the Cu substrate used during synthesis can hugely impact the key physical properties of the Cuf produced, such as mechanical (adhesion, hardness, ductility *etc.*) or electrical (resistivity, conductivity, *etc.*). The dependence of the degree of porosity and the thickness of Cuf on the Cu foil substrate is almost a non-redundant issue.

(3) It has been observed that electrodeposited materials have a very high internal stress that can sometimes lead to cracks on the substrate. The porous structure is responsible for the large surface area of the Cuf, however the lack of homogeneity of the pore structure, when the deposition is scaled up, is majorly encountered.[270] The good stability and adhesion of porous dendrites to the substrate for high thickness Cuf deposits is still a challenge.

(4) Apart from the high demand and material design, Cuf still faces the major problem of oxidation with the ambient atmosphere.[27]

At this point, genuinely new applications of DHBT-derived Cuf, especially in commercial energy generation (water electrolysers, fuel cells), storage (supercapacitors, LIBs) and conversion (metal–air batteries) devices, are still in their infancy. It is safe to say that the current understanding of bubble behaviour, the mechanisms of coalescence and the growth of a porous Cuf morphology are on a mature enough level that constructing a range of highly useful structures with reasonable control of morphology and adorning with key structural properties can be progressed to the next level. An increasing understanding of the experimental conditions, quality of the substrate used, surface modifications and precautions taken during post treatment can significantly improve the stability and performance of the as-synthesized Cuf. For instance, the problem of unstable and overgrown nano-ramification in electrodeposition can be highly controlled *via* surface conduction above the diffusion-limited current, *i.e.*, by modifying the surface with the layer-by-layer assembly of positively or negatively charged polyelectrolytes, which is simply known as shock electrodeposition. It has been observed that shock electrodeposition can be exploited to improve the cycle life or recharging rate of LIBs.[271] A logical first step towards scaling up attempts can be accomplished by replicating the deposition on gas diffusion electrodes (GDEs) instead of simple Cu foils because that would effectively improve the limited mass transport and increase the activity. Therefore, it is expected that with the multidimensionality and emerging features of 3D Cuf, it can emerge as a viable alternative to nanoparticle-based active electrode components and enhanced performance is feasible in all of the emerging energy applications that we have identified, followed by new applications in the near future (Fig. 20).

Author contributions

MD, AB and TP: resources, literature survey, writing-original draft, MD: literature review and writing on Cuf synthesis, properties and energy generation, TP: literature review and writing introduction, Cuf properties and energy storage, AB: literature review, writing on electrocatalysis (ORR and NRR) and figure arrangements TB: figure arrangements, manuscript formatting and revising the whole manuscript SB: literature review and writing on electrocatalysis (CO_2RR), SKD: writing the properties of Cuf and gone through the review for overall corrections, RSD: conceptualization, supervision and writing, review & editing the final version of manuscript. All the authors checked the final version of the manuscript and approved the submission.

Conflicts of interest

There are no conflicts to declare.

Acknowledgements

MD, AB, SB and SKD acknowledge INST Mohali for providing fellowship. TP acknowledges DST INSPIRE and CSIR SRF for providing fellowship. TB acknowledges DST SERB for providing fellowship. This work was financially supported by DST INSPIRE (DST/INSPIRE/04/2015/000337) and DST SERB (CRG/2020/005683).

References

1 R. S. Dey, H. A. Hjuler and Q. Chi, *J. Mater. Chem. A*, 2015, **3**, 6324–6329.
2 H. Zhang, Y. Ye, R. Shen, C. Ru and Y. Hu, *J. Electrochem. Soc.*, 2013, **160**, D441.
3 J. Niu, X. Liu, K. Xia, L. Xu, Y. Xu, X. Fang and W. Lu, *Int. J. Electrochem. Sci.*, 2015, **10**, 7331–7340.
4 G. Sandrini, H. C. Matthijs, J. M. Verspagen, G. Muyzer and J. Huisman, *ISME J.*, 2014, **8**, 589–600.
5 S. Eugénio, U. B. Demirci, T. M. Silva, M. J. Carmezim and M. F. Montemor, *Int. J. Hydrogen Energy*, 2016, **41**, 8438–8448.
6 H. Jo, Y.-H. Cho, M. Choi, J. Cho, J. H. Um, Y.-E. Sung and H. Choe, *Mater. Chem. Phys.*, 2014, **145**, 6–11.
7 C. Chen, Y. Pang, F. Zhang, J. Zhong, B. Zhang and Z. Cheng, *J. Mater. Chem. A*, 2018, **6**, 19621–19630.
8 K. Ye, Z. Zhou, J. Shao, L. Lin, D. Gao, N. Ta, R. Si, G. Wang and X. Bao, *Angew. Chem., Int. Ed.*, 2020, **59**, 4814–4821.
9 L. Xiong, Y.-X. Huang, X.-W. Liu, G.-P. Sheng, W.-W. Li and H.-Q. Yu, *Electrochim. Acta*, 2013, **89**, 24–28.
10 M. Das, N. Jena, T. Purkait, N. Kamboj, A. De Sarkar and R. S. Dey, *J. Mater. Chem. A*, 2019, **7**, 23989–23999.
11 C. Li, S. Mou, X. Zhu, F. Wang, Y. Wang, Y. Qiao, X. Shi, Y. Luo, B. Zheng and Q. Li, *Chem. Commun.*, 2019, **55**, 14474–14477.

12 H. Lee, J. Kim, I. Choi and S. H. Ahn, *Electrochim. Acta*, 2019, **323**, 133102.
13 Y. Liu, Q. Li, R. Si, G. D. Li, W. Li, D. P. Liu, D. Wang, L. Sun, Y. Zhang and X. Zou, *Adv. Mater.*, 2017, **29**, 1606200.
14 N. D. Nikolić, G. Branković and V. M. Maksimović, *J. Solid State Electrochem.*, 2012, **16**, 321–328.
15 N. Kränzlin and M. Niederberger, *Adv. Mater.*, 2013, **25**, 5599–5604.
16 S. Sen, D. Liu and G. T. R. Palmore, *ACS Catal.*, 2014, **4**, 3091–3095.
17 R. E. Smalley, *MRS Bull.*, 2005, **30**, 412–417.
18 B. Rezaei, M. Mokhtarianpour and A. A. Ensafi, *Int. J. Hydrogen Energy*, 2015, **40**, 6754–6762.
19 X. An, S. Li, A. Yoshida, T. Yu, Z. Wang, X. Hao, A. Abudula and G. Guan, *ACS Appl. Mater. Interfaces*, 2019, **11**, 42114–42122.
20 Y. Jin, F. Chen, Y. Lei and X. Wu, *ChemCatChem*, 2015, **7**, 2377–2383.
21 A. Dutta, I. Z. Montiel, R. Erni, K. Kiran, M. Rahaman, J. Drnec and P. Broekmann, *Nano Energy*, 2020, **68**, 104331.
22 D. A. Lashof and D. R. Ahuja, *Nature*, 1990, **344**, 529–531.
23 J. Lelieveld and P. J. Crutzen, *Nature*, 1992, **355**, 339–342.
24 D. G. Nocera, *Chem. Soc. Rev.*, 2009, **38**, 13–15.
25 Y. Shao, M. F. El-Kady, J. Sun, Y. Li, Q. Zhang, M. Zhu, H. Wang, B. Dunn and R. B. Kaner, *Chem. Rev.*, 2018, **118**, 9233–9280.
26 N. Kamboj, T. Purkait, M. Das, S. Sarkar, K. S. Hazra and R. S. Dey, *Energy Environ. Sci.*, 2019, **12**, 2507–2517.
27 Y. D. Gamburg and G. Zangari, *Theory and Practice of Metal Electrodeposition*, Springer Science & Business Media, 2011.
28 M. Das, N. Kamboj, T. Purkait, S. Sarkar and R. S. Dey, *J. Phys. Chem. C*, 2020, **124**, 13525–13534.
29 V. Sharma, V. Racherla and S. Pal, *Int. J. Adv. Des. Manuf. Technol.*, 2019, **103**, 3163–3174.
30 B. Wolter, M. G. Pullen, M. Baudisch, M. Sclafani, M. Hemmer, A. Senftleben, C. D. Schröter, J. Ullrich, R. Moshammer and J. Biegert, *Phys. Rev. X*, 2015, **5**, 021034.
31 C. Ramirez-Castro, C. Schütter, S. Passerini and A. Balducci, *Electrochim. Acta*, 2016, **206**, 452–457.
32 S. Chu and A. Majumdar, *Nature*, 2012, **488**, 294–303.
33 F. M. Sapountzi, J. M. Gracia, H. O. Fredriksson and J. H. Niemantsverdriet, *Prog. Energy Combust. Sci.*, 2017, **58**, 1–35.
34 S. S. Mao and X. Chen, *Int. J. Energy Res.*, 2007, **31**, 619–636.
35 S. Almosni, A. Delamarre, Z. Jehl, D. Suchet, L. Cojocaru, M. Giteau, B. Behaghel, A. Julian, C. Ibrahim and L. Tatry, *Sci. Technol. Adv. Mater.*, 2018, **19**, 336–369.
36 J. Cabana, L. Monconduit, D. Larcher and M. R. Palacin, *Adv. Mater.*, 2010, **22**, E170–E192.
37 L. Zhang, L. Harnefors and H.-P. Nee, *IEEE Trans. Power Syst.*, 2009, **25**, 809–820.
38 K. R. Coelho, *Depression Research and Treatment*, 2012, 2012.
39 K. Eid, H. Wang, V. Malgras, S. M. Alshehri, T. Ahamad, Y. Yamauchi and L. Wang, *J. Electroanal. Chem.*, 2016, **779**, 250–255.
40 H. Ibrahim, A. Ilinca and J. Perron, *Renew. Sustain. Energy Rev.*, 2008, **12**, 1221–1250.
41 H. L. Tuller, *Mater. Renew. Sustain. Energy*, 2017, **6**, 3.
42 J. B. Goodenough, H. D. Abruna and M. V. Buchanan, *Basic Research Needs for Electrical Energy Storage. Report of the Basic Energy Sciences Workshop on Electrical Energy Storage, April 2-4, 2007*, DOESC (USDOE Office of Science (SC)), 2007.
43 R. Kim, D. Han, D. Nam, J. Kim and H. Kwon, *J. Electrochem. Soc.*, 2010, **157**, D269.
44 S. Ganguly, D. Banerjee and K. Kargupta, *Proceedings of the International Conference Nanomaterials: Applications and Properties*, 2012, vol. 1, p. 04NEA09-04NEA09.
45 P. K. Rai, V. Kumar, S. Lee, N. Raza, K.-H. Kim, Y. S. Ok and D. C. Tsang, *Environ. Int.*, 2018, **119**, 1–19.
46 Y. Liu, G. Zhou, K. Liu and Y. Cui, *Acc. Chem. Res.*, 2017, **50**, 2895–2905.
47 E. Fabbri, A. Habereder, K. Waltar, R. Kötz and T. J. Schmidt, *Catal. Sci. Technol.*, 2014, **4**, 3800–3821.
48 S. Ghosh and R. N. Basu, *Nanoscale*, 2018, **10**, 11241–11280.
49 L. Wei, K. Goh, Ö. Birer, H. E. Karahan, J. Chang, S. Zhai, X. Chen and Y. Chen, *Nanoscale*, 2017, **9**, 4401–4408.
50 R. Abdel-Karim, M. Ramadan and S. M. El-Raghy, *J. Nanomater.*, 2018, 9870732.
51 J. Biener, A. Wittstock, T. F. Baumann, J. Weissmüller, M. Bäumer and A. V. Hamza, *Materials*, 2009, **2**, 2404–2428.
52 J. Jeevanandam, A. Barhoum, Y. S. Chan, A. Dufresne and M. K. Danquah, *Beilstein J. Nanotechnol.*, 2018, **9**, 1050–1074.
53 M. A. Gatoo, S. Naseem, M. Y. Arfat, A. M. Dar, K. Qasim and S. Zubair, *BioMed Res. Int.*, 2014, **2014**, 8.
54 N. K. Chaudhari, H. Jin, B. Kim and K. Lee, *Nanoscale*, 2017, **9**, 12231–12247.
55 K. Neyerlin, G. Bugosh, R. Forgie, Z. Liu and P. Strasser, *J. Electrochem. Soc.*, 2009, **156**, B363.
56 Y. K. Kim, S. I. Cha and S. H. Hong, *J. Mater. Chem. A*, 2013, **1**, 9802–9808.
57 B. C. Tappan, S. A. Steiner III and E. P. Luther, *Angew. Chem., Int. Ed.*, 2010, **49**, 4544–4565.
58 Z. Hua, Y. Deng, K. Li and S. Yang, *Nanoscale Res. Lett.*, 2012, **7**, 1–7.
59 P. Liu, G. Chen, P. Liu and G. Chen, *Porous Mater.*, 2014, 113–188.
60 K. I. Popov, S. S. Djokić, N. D. Nikolić and V. D. Jović, in *Morphology of Electrochemically and Chemically Deposited Metals*, Springer, 2016, pp. 111–139.
61 K. Kreder and A. Manthiram, *Chem. Commun.*, 2017, **53**, 865–868.
62 N. Frese, S. T. Mitchell, C. Neumann, A. Bowers, A. Gölzhäuser and K. Sattler, *Beilstein J. Nanotechnol.*, 2016, **7**, 2065–2073.
63 S. Korkmaz and İ. A. Kariper, *J. Energy Storage*, 2020, **27**, 101038.
64 C. Hu, Y. Xiao, Y. Zou and L. Dai, *Electrochem. Energy Rev.*, 2018, **1**, 238.
65 J. H. Holtz, J. S. Holtz, C. H. Munro and S. A. Asher, *Anal. Chem.*, 1998, **70**, 780–791.

66 J. M. Weissman, H. B. Sunkara, S. T. Albert and S. A. Asher, *Science*, 1996, **274**, 959–963.
67 S. Ghosh and O. Inganäs, *Adv. Mater.*, 1999, **11**, 1214–1218.
68 D. R. Rolison and B. Dunn, *J. Mater. Chem.*, 2001, **11**, 963–980.
69 J. Wang, S. Zhang, Y. Guo, J. Shen, S. Attia, B. Zhou, G. Zheng and Y. Gui, *J. Electrochem. Soc.*, 2001, **148**, D75.
70 M. R. Shirazy, S. Blais and L. G. Fréchette, *Appl. Surf. Sci.*, 2012, **258**, 6416–6424.
71 D. Zang, C. Wu, R. Zhu, W. Zhang, X. Yu and Y. Zhang, *Chem. Commun.*, 2013, **49**, 8410–8412.
72 D. Mott, J. Luo and J. Zhong, Synergistic activity of gold-platinum alloy nanoparticle catalysts, *Catal. Today*, 2007, **122**, 378–385.
73 C. Shum, G. Rosengarten and Y. Zhu, *Microfluid. Nanofluid.*, 2017, **21**, 177.
74 C. Hou, X.-Y. Lang, Z. Wen, Y.-F. Zhu, M. Zhao, J.-C. Li, W.-T. Zheng, J.-S. Lian and Q. Jiang, *J. Mater. Chem. A*, 2015, **3**, 23412–23419.
75 M. R. Shirazy and L. G. Fréchette, *Int. J. Heat Mass Transfer*, 2013, **58**, 282–291.
76 R. Abdel-Karim, in *Handbook of Nanomaterials and Nanocomposites for Energy and Environmental Applications*, ed. O. V. Kharissova, L. M. Torres-Martínez and B. I. Kharisov, Springer International Publishing, Cham, 2021, pp. 489–511, DOI: 10.1007/978-3-030-36268-3_8.
77 R. Abdel-Karim, *Handbook of Nanomaterials and Nanocomposites for Energy and Environmental Applications*, 2021, pp. 489–511.
78 H. Sun, H. Kim, S. Song and W. Jung, *Materials Reports: Energy*, 2022, 100092.
79 S. Feng, J. Wang, W. Wang, X. Wang, Y. Zhang, A. Ju, J. Pan and R. Xu, *Adv. Mater. Interfaces*, 2021, **8**, 2100500.
80 T. Jibowu, *Front. Nanosci. Nanotechnol.*, 2016, **2**, 165–168.
81 G. A. El-Nagar, I. Derr, T. Kottakkat and C. Roth, *ECS Trans.*, 2017, **80**, 1013.
82 M. Hirscher, V. A. Yartys, M. Baricco, J. B. von Colbe, D. Blanchard, R. C. Bowman Jr, D. P. Broom, C. E. Buckley, F. Chang and P. Chen, *J. Alloys Compd.*, 2020, **827**, 153548.
83 M. Guden, E. Celik, S. Cetiner and A. Aydin, in *Biomaterials*, Springer, 2004, pp. 257–266.
84 J. Erlebacher, M. J. Aziz, A. Karma, N. Dimitrov and K. Sieradzki, *Nature*, 2001, **410**, 450–453.
85 J. Erlebacher and K. Sieradzki, *Scr. Mater.*, 2003, **49**, 991–996.
86 L. Zaraska, N. Czopik, M. Bobruk, G. D. Sulka, J. Mech and M. Jaskuła, *Electrochim. Acta*, 2013, **104**, 549–557.
87 B. J. Plowman, L. A. Jones and S. K. Bhargava, *Chem. Commun.*, 2015, **51**, 4331–4346.
88 M. T. Reetz and W. Helbig, *J. Am. Chem. Soc.*, 1994, **116**, 7401–7402.
89 M. Wang, X. Yu, Z. Wang, X. Gong, Z. Guo and L. Dai, *J. Mater. Chem. A*, 2017, **5**, 9488–9513.
90 Y. S. Park, W.-S. Choi, M. J. Jang, J. H. Lee, S. Park, H. Jin, M. H. Seo, K.-H. Lee, Y. Yin, Y. Kim, J. Yang and S. M. Choi, *ACS Sustainable Chem. Eng.*, 2019, **7**, 10734–10741.
91 F. Urbach, *Phys. Rev.*, 1953, **92**, 1324.
92 C. Marozzi and A. Chialvo, *Electrochim. Acta*, 2000, **45**, 2111–2120.
93 C. Marozzi and A. Chialvo, *Electrochim. Acta*, 2001, **46**, 861–866.
94 H. C. Shin, J. Dong and M. Liu, *Adv. Mater.*, 2003, **15**, 1610–1614.
95 X. Zhu, R. N. Ali, Y. Yang, Z. Zheng, B. Xiang and X. Cui, *J. Porous Mater.*, 2019, **26**, 1363–1368.
96 S. Cherevko, X. Xing and C.-H. Chung, *Electrochem. Commun.*, 2010, **12**, 467–470.
97 S. Cherevko and C.-H. Chung, *Electrochim. Acta*, 2010, **55**, 6383–6390.
98 B. J. Plowman, S. K. Bhargava and A. P. O'Mullane, *Analyst*, 2011, **136**, 5107–5119.
99 G.-M. Yang, X. Chen, J. Li, Z. Guo, J.-H. Liu and X.-J. Huang, *Electrochim. Acta*, 2011, **56**, 6771–6778.
100 A. Ott, L. A. Jones and S. K. Bhargava, *Electrochem. Commun.*, 2011, **13**, 1248–1251.
101 P. Arévalo-Cid, A. Adán-Más, T. M. Silva, J. A. Rodrigues, E. Maçôas, M. F. Vaz and M. F. Montemor, *Mater. Charact.*, 2020, **169**, 110598.
102 J. Yin and J. Y. Park, *Int. J. Hydrog. Energy*, 2014, **39**, 16562–16568.
103 K.-Y. Chan, J. Ding, J. Ren, S. Cheng and K. Y. Tsang, *J. Mater. Chem.*, 2004, **14**, 505–516.
104 I. Najdovski, P. Selvakannan and A. P. O'Mullane, *RSC Adv.*, 2014, **4**, 7207–7215.
105 I. Najdovski, P. Selvakannan, S. K. Bhargava and A. P. O'Mullane, *Nanoscale*, 2012, **4**, 6298–6306.
106 J. Liu, L. Cao, Y. Xia, W. Huang and Z. Li, *Int. J. Electrochem. Sci.*, 2013, **8**, 9435–9441.
107 Y. N. Raikov, G. Ashikhmin, A. Nikolaev, N. Revina and S. Kostin, *Metallurgist*, 2007, **51**, 408–416.
108 M. B. Gawande, A. Goswami, F.-X. Felpin, T. Asefa, X. Huang, R. Silva, X. Zou, R. Zboril and R. S. Varma, *Chem. Rev.*, 2016, **116**, 3722–3811.
109 B. Camacho-Flores, O. Martínez-Álvarez, M. Arenas-Arrocena, R. Garcia-Contreras, L. Argueta-Figueroa, J. De La Fuente-Hernández and L. Acosta-Torres, *J. Nanomater.*, 2015, **2015**, 415238.
110 N. U. A. Babar, K. S. Joya, M. A. Ehsan, M. Khan and M. Sharif, *ChemCatChem*, 2019, **11**, 1002.
111 C. Du, X. Gao and W. Chen, *Chin. J. Catal.*, 2016, **37**, 1049–1061.
112 L. Zhou, Y. He, C. Jia, V. Pavlinek, P. Saha and Q. Cheng, *Nanomaterials*, 2017, **7**, 273.
113 R. Niu, K. Han, Y.-f. Su, T. Besara, T. M. Siegrist and X. Zuo, *Sci. Rep.*, 2016, **6**, 1–13.
114 M. A. Tschopp, S. P. Coleman and D. L. McDowell, *Integr. Mater. Manuf. Innov.*, 2015, **4**, 176–189.
115 L. Chen, X. Xie, J. Xie, K. Wang and J. Yang, *J. Appl. Electrochem.*, 2006, **36**, 1099–1104.
116 J. Han, V. Vitek and D. J. Srolovitz, *Acta Mater.*, 2016, **104**, 259–273.
117 E. Rabkin, *Nature*, 2020, **579**, 350–351.
118 T. Frolov, D. L. Olmsted, M. Asta and Y. Mishin, *Nat. Commun.*, 2013, **4**, 1–7.

119 B. Luo, X. Li, X. Li and W. Feng, *Asian J. Chem.*, 2013, **25**, 17.
120 J. M. Bockris and N. Pentland, *Trans. Faraday Soc.*, 1952, **48**, 833–839.
121 J. C. Huang and Y. J. Weng, *Appl. Mech. Mater.*, 2012, **117**, 394–397.
122 M. Saremi and M. Yeganeh, *Int. J. Mod. Phys.: Conf. Ser.*, 2012, **5**, 687–695.
123 H. Miyamoto, K. Harada, T. Mimaki, A. Vinogradov and S. Hashimoto, *Corros. Sci.*, 2008, **50**, 1215–1220.
124 N. A. Ogolo, O. G. Akinboro, J. E. Inam, F. E. Akpokere and M. O. Onyekonwu, *SPE Nigeria Annual International Conference and Exhibition*, 2015, p. 178296–MS.
125 Y. Zhang, J. Huang and Y. Ding, *Appl. Catal., B*, 2016, **198**, 447–456.
126 X. Wang, X. Hou, H. Lee, L. Lu, X. Wu and L. Sun, *Energy Technol.*, 2020, **8**, 2000142.
127 A. Etiemble, J. Adrien, E. Maire, H. Idrissi, D. Reyter and L. Roué, *Mater. Sci. Eng., B*, 2014, **187**, 1–8.
128 F. Dogan, L. D. Sanjeewa, S.-J. Hwu and J. Vaughey, *Solid State Ionics*, 2016, **288**, 204–206.
129 J. Yu, Y. Dang, M. Bai, J. Peng, D. Zheng, J. Zhao, L. Li and Z. Fang, *Front. Chem.*, 2019, **7**, 748.
130 T. Purkait, G. Singh, D. Kumar, M. Singh and R. S. Dey, *Sci. Rep.*, 2018, **8**, 1–13.
131 J. Niu, X. Liu, K. Xia, L. Xu, Y. Xu, X. Fang and W. Lu, *Int. J. Electrochem. Sci.*, 2015, **10**, 7331–7340.
132 J. K. Nørskov, T. Bligaard, A. Logadottir, J. Kitchin, J. G. Chen, S. Pandelov and U. Stimming, *J. Electrochem. Soc.*, 2005, **152**, J23.
133 H.-C. Shin and M. Liu, *Chem. Mater.*, 2004, **16**, 5460–5464.
134 J. A. Rudd, S. Hernandez-Aldave, E. Kazimierska, L. B. Hamdy, O. J. E. Bain, A. R. Barron and E. Andreoli, *Chemistry*, 2021, **3**, 687–703.
135 P. P. Trigueros, F. Sagués and J. Claret, *Phys. Rev. E: Stat. Phys., Plasmas, Fluids, Relat. Interdiscip. Top.*, 1994, **49**, 4328.
136 S. N. Atchison, R. P. Burford, C. P. Whitby and D. B. Hibbert, *J. Electroanal. Chem.*, 1995, **399**, 71–77.
137 M.-Q. Lopez-Salvans, F. Sagues, J. Claret and J. Bassas, *J. Electroanal. Chem.*, 1997, **421**, 205–212.
138 M. D. L. Balela, R. E. Masirag, F. O. Pacariem Jr and J. M. D. Taguinod, *Key Eng. Mater.*, 2021, **880**, 83–88.
139 Y. Li, W.-Z. Jia, Y.-Y. Song and X.-H. Xia, *Chem. Mater.*, 2007, **19**, 5758–5764.
140 J.-H. Kim, R.-H. Kim and H.-S. Kwon, *Electrochem. Commun.*, 2008, **10**, 1148–1151.
141 D. Nam, R. Kim, D. Han, J. Kim and H. Kwon, *Electrochim. Acta*, 2011, **56**, 9397–9405.
142 K. Tan, M.-B. Tian and Q. Cai, *Thin Solid Films*, 2010, **518**, 5159–5163.
143 T. P. Moffat, D. Wheeler and D. Josell, *J. Electrochem. Soc.*, 2004, **151**, C262.
144 H. Yang, X. Hao, J. Tang, W. Jin, C. Liu, H. Hou, X. Ji and J. Hu, *Appl. Surf. Sci.*, 2019, **494**, 731–739.
145 X. Lin, F. Lu, Y. Chen, N. Liu, Y. Cao, L. Xu, W. Zhang and L. Feng, *Chem. Commun.*, 2015, **51**, 16237–16240.
146 M. Asnavandi, B. H. R. Suryanto, W. Yang, X. Bo and C. Zhao, *ACS Sustainable Chem. Eng.*, 2018, **6**, 2866–2871.
147 S.-C. Wong and Y.-C. Lin, *Int. J. Heat Mass Transfer*, 2011, **54**, 3921–3926.
148 J. A. Weibel, S. V. Garimella and M. T. North, *Int. J. Heat Mass Transfer*, 2010, **53**, 4204–4215.
149 B. D. Iverson, T. W. Davis, S. V. Garimella, M. T. North and S. S. Kang, *J. Thermophys. Heat Transfer*, 2007, **21**, 392–404.
150 Y. Zhou, Z. C. Hong, X. P. Ai and X. Q. Zuo, *Adv. Mater. Res.*, 2013, 1163–1166.
151 R. Goodall, L. Weber and A. Mortensen, *J. Appl. Phys.*, 2006, **100**, 044912.
152 L. I. Chernyshev and V. V. Skorokhod, *Powder Metall. Met. Ceram.*, 2003, **42**, 88–93.
153 R. Ewing and A. Hunt, *Vadose Zone J.*, 2006, **5**, 731–741.
154 L. Weber, J. Dorn and A. Mortensen, *Acta Mater.*, 2003, **51**, 3199–3211.
155 M. Tane, S. Hyun and H. Nakajima, *J. Appl. Phys.*, 2005, **97**, 103701.
156 B. Li and X. Lu, *Transp. Porous Media*, 2011, **87**, 179–189.
157 Z. Ke, L. Cheng-Feng and Z. Zhen-Gang, *Chin. Phys. Lett.*, 2007, **24**, 187.
158 B. Shklovskiĭ and A. L. v. Éfros, *Sov. Phys., Usp.*, 1975, **18**, 845.
159 M. Mirzaee, C. Dehghanian and K. S. Bokati, *J. Electroanal. Chem.*, 2018, **813**, 152–162.
160 Y. Reda, R. Abdel-Karim, K. M. Zohdy and S. El-Raghy, *Ain Shams Eng. J.*, 2022, **13**, 101532.
161 M. R. Rizk, M. G. Abd El-Moghny, A. Mazhar, M. S. El-Deab and B. E. El-Anadouli, *Sustainable Energy Fuels*, 2021, **5**, 986–994.
162 I. A. Mudunkotuwa, J. M. Pettibone and V. H. Grassian, *Environ. Sci. Technol.*, 2012, **46**, 7001–7010.
163 A. R. Zeradjanin, G. Polymeros, C. Toparli, M. Ledendecker, N. Hodnik, A. Erbe, M. Rohwerder and F. La Mantia, *Phys. Chem. Chem. Phys.*, 2020, **22**, 8768–8780.
164 J.-W. Yu, G.-b. Jung, Y.-J. Su, C.-C. Yeh, M.-Y. Kan, C.-Y. Lee and C.-J. Lai, *Int. J. Hydrogen Energy*, 2019, **44**, 15721–15726.
165 Z. Liu, L. Guo, C.-L. Chien and P. C. Searson, *J. Electrochem. Soc.*, 2008, **155**, D569.
166 J. Zhang, M. Baró, E. Pellicer and J. Sort, *Nanoscale*, 2014, **6**, 12490–12499.
167 L. H. Jepsen, M. B. Ley, Y.-S. Lee, Y. W. Cho, M. Dornheim, J. O. Jensen, Y. Filinchuk, J. E. Jørgensen, F. Besenbacher and T. R. Jensen, *Mater. Today*, 2014, **17**, 129–135.
168 M. Yadav and Q. Xu, *Energy Environ. Sci.*, 2012, **5**, 9698–9725.
169 N. Patel and A. Miotello, *Int. J. Hydrogen Energy*, 2015, **40**, 1429–1464.
170 W. S. Abdul-Majeed, M. T. Arslan and W. B. Zimmerman, *Int. J. Ind. Chem.*, 2014, **5**, 1–9.
171 U. B. Demirci, *Int. J. Hydrogen Energy*, 2015, **40**, 2673–2691.
172 U. B. Demirci and P. Miele, *Phys. Chem. Chem. Phys.*, 2010, **12**, 14651–14665.
173 M. Lu, D. Chen, R. Li, B. Wang, D. Cai, L. Li and W. Han, *Sustainable Energy Fuels*, 2020, **4**, 4039–4045.
174 L. Yu, H. Zhou, J. Sun, F. Qin, D. Luo, L. Xie, F. Yu, J. Bao, Y. Li and Y. Yu, *Nano Energy*, 2017, **41**, 327–336.

175 Y. Sun, C. Liu, D. C. Grauer, J. Yano, J. R. Long, P. Yang and C. J. Chang, *J. Am. Chem. Soc.*, 2013, **135**, 17699–17702.
176 R. Miao, B. Dutta, S. Sahoo, J. He, W. Zhong, S. A. Cetegen, T. Jiang, S. P. Alpay and S. L. Suib, *J. Am. Chem. Soc.*, 2017, **139**, 13604–13607.
177 D. Merki, H. Vrubel, L. Rovelli, S. Fierro and X. Hu, *Chem. Sci.*, 2012, **3**, 2515–2525.
178 N. Jiang, B. You, M. Sheng and Y. Sun, *Angew. Chem.*, 2015, **127**, 6349–6352.
179 C. Liu, J. Tang, H. M. Chen, B. Liu and P. Yang, *Nano Lett.*, 2013, **13**, 2989–2992.
180 S. Cobo, J. Heidkamp, P.-A. Jacques, J. Fize, V. Fourmond, L. Guetaz, B. Jousselme, V. Ivanova, H. Dau and S. Palacin, *Nat. Mater.*, 2012, **11**, 802–807.
181 Y. Yang, H. Fei, G. Ruan and J. M. Tour, *Adv. Mater.*, 2015, **27**, 3175–3180.
182 B. You and Y. Sun, *Adv. Energy Mater.*, 2016, **6**, 1502333.
183 H. Jin, J. Wang, D. Su, Z. Wei, Z. Pang and Y. Wang, *J. Am. Chem. Soc.*, 2015, **137**, 2688–2694.
184 Q. Ye, X. Hou, H. Lee, H. Liu, L. Lu, X. Wu and L. Sun, *ChemPlusChem*, 2020, **85**, 1339–1346.
185 A. R. Kucernak and V. N. N. Sundaram, *J. Mater. Chem. A*, 2014, **2**, 17435–17445.
186 M. Ledendecker, J. S. Mondschein, O. Kasian, S. Geiger, D. Göhl, M. Schalenbach, A. Zeradjanin, S. Cherevko, R. E. Schaak and K. Mayrhofer, *Angew. Chem., Int. Ed.*, 2017, **56**, 9767–9771.
187 J. Kim, J. Kim, H. Kim and S. H. Ahn, *ACS Appl. Mater. Interfaces*, 2019, **11**, 30774–30785.
188 Y. Tan, H. Wang, P. Liu, Y. Shen, C. Cheng, A. Hirata, T. Fujita, Z. Tang and M. Chen, *Energy Environ. Sci.*, 2016, **9**, 2257–2261.
189 K. Yeon, J. Kim, H. Kim, W. Guo, G. H. Han, S. Hong and S. H. Ahn, *Korean J. Chem. Eng.*, 2020, **37**, 1379–1386.
190 M. Mirzaee and C. Dehghanian, *J. Iran. Chem. Soc.*, 2019, **16**, 283–292.
191 L. Xue, Z. Fu, Y. Yao, T. Huang and A. Yu, *Electrochim. Acta*, 2010, **55**, 7310–7314.
192 A. Abdelfatah, Y. Reda, R. Abdel-Karim, S. El-Raghy and K. M. Zohdy, *Front. Mech. Eng.*, 2020, **6**, 35.
193 K.-N. Kang, I.-H. Kim, A. Ramadoss, S.-I. Kim, J.-C. Yoon and J.-H. Jang, *Phys. Chem. Chem. Phys.*, 2018, **20**, 719–727.
194 H. N. Umh, J. Park, J. Yeo, S. Jung, I. Nam and J. Yi, *Electrochem. Commun.*, 2019, **99**, 27–31.
195 S. Eugénio, T. Silva, M. Carmezim, R. Duarte and M. Montemor, *J. Appl. Electrochem.*, 2014, **44**, 455–465.
196 G. Lange, S. Eugénio, R. Duarte, T. Silva, M. Carmezim and M. d. F. Montemor, *J. Electroanal. Chem.*, 2015, **737**, 85–92.
197 J. Xu, L. Gao, J. Cao, W. Wang and Z. Chen, *Electrochim. Acta*, 2010, **56**, 732–736.
198 Y. Lei, B. Daffos, P.-L. Taberna, P. Simon and F. Favier, *Electrochim. Acta*, 2010, **55**, 7454–7459.
199 X. Liu, T. A. Huber, M. C. Kopac and P. G. Pickup, *Electrochim. Acta*, 2009, **54**, 7141–7147.
200 I. Barauskienė and E. Valatka, *Cent. Eur. J. Chem.*, 2014, **12**, 1206–1211.
201 H. Wang, Z. Jusys and R. J. Behm, *Electrochim. Acta*, 2009, **54**, 6484–6498.
202 Y. Li, S. Chang, X. Liu, J. Huang, J. Yin, G. Wang and D. Cao, *Electrochim. Acta*, 2012, **85**, 393–398.
203 M.-G. Jeong, K. Zhuo, S. Cherevko, W.-J. Kim and C.-H. Chung, *J. Power Sources*, 2013, **244**, 806–811.
204 H. C. Shin and M. Liu, *Adv. Funct. Mater.*, 2005, **15**, 582–586.
205 C. Tan, G. Qi, Y. Li, J. Guo, X. Wang, D. Kong, H. Wang and S. Zhang, *Int. J. Electrochem. Sci.*, 2012, **7**, 10303–10312.
206 D. H. Nam, R. H. Kim, D. W. Han and H. S. Kwon, *Electrochim. Acta*, 2012, **66**, 126–132.
207 J. Suk, D. W. Kim and Y. Kang, *J. Mater. Chem. A*, 2014, **2**, 2478–2481.
208 H. Qiu, T. Tang, M. Asif, X. Huang and Y. Hou, *Adv. Funct. Mater.*, 2019, **29**, 1808468.
209 X.-Y. Fan, F.-S. Ke, G.-Z. Wei, L. Huang and S.-G. Sun, *J. Alloys Compd.*, 2009, **476**, 70–73.
210 D.-H. Nam, K.-S. Hong, S.-J. Lim and H.-S. Kwon, *J. Power Sources*, 2014, **247**, 423–427.
211 S. W. Kim, Y. Son, K. Choi, S. I. Kim, Y. Son, J. Park, J. H. Lee and J. H. Jang, *ChemSusChem*, 2018, **11**, 4203–4208.
212 R. N. Mutlu, *J. Solid State Electrochem.*, 2019, **23**, 529–541.
213 Y. Guan, N. Li, Y. Li, L. Sun, Y. Gao, Q. Zhang, C. He, J. Liu and X. Ren, *Nanoscale*, 2020, **12**, 14259–14266.
214 Z. Chufeng, C. Zhewei, L. Yuebin, C. Yujie, L. Qin, G. Yindong, L. Yongtao, D. Zhao and P. Yang, *Acta Phys.-Chim. Sin.*, 2019, **35**, 1404–1411.
215 H. Wang, Y. Min, P. Li, J. Yang and J. Li, *Electrochim. Acta*, 2018, **283**, 54–62.
216 Y. Jin and F. Chen, *Electrochim. Acta*, 2015, **158**, 437–445.
217 M. Acosta, A. Ač, M. Pavelka, K. Havránková, H. W. Loescher, J. H. Butler, D. Janouš and M. V. Marek, *Environments*, 2020, **7**, 19.
218 B. Ekwurzel, J. Boneham, M. W. Dalton, R. Heede, R. J. Mera, M. R. Allen and P. C. Frumhoff, *Clim. Change*, 2017, **144**, 579–590.
219 V. Tripkovic, M. Vanin, M. Karamad, M. r. E. Björketun, K. W. Jacobsen, K. S. Thygesen and J. Rossmeisl, *J. Phys. Chem. C*, 2013, **117**, 9187–9195.
220 M. McKinnon, V. Belkina, K. T. Ngo, M. Z. Ertem, D. C. Grills and J. Rochford, *Front. Chem.*, 2019, **7**, 628.
221 S. Vesztergom, A. Dutta, M. Rahaman, K. Kiran, I. Z. Montiel and P. Broekmann, *ChemCatChem*, 2021, **13**, 1039–1058.
222 J. Guan, S. A. Berlinger, X. Li, Z. Chao, V. S. e Silva, S. Banta and A. C. West, *J. Biotechnol.*, 2017, **245**, 21–27.
223 J. Wu, R. M. Yadav, M. Liu, P. P. Sharma, C. S. Tiwary, L. Ma, X. Zou, X.-D. Zhou, B. I. Yakobson and J. Lou, *ACS Nano*, 2015, **9**, 5364–5371.
224 K. Teramura, S. Iguchi, Y. Mizuno, T. Shishido and T. Tanaka, *Angew. Chem., Int. Ed.*, 2012, **51**, 8008–8011.
225 K. Atsonios, K. D. Panopoulos and E. Kakaras, *Int. J. Hydrogen Energy*, 2016, **41**, 792–806.
226 B. M. Tackett, E. Gomez and J. G. Chen, *Nat. Catal.*, 2019, **2**, 381–386.
227 S. Hernández, M. A. Farkhondehfal, F. Sastre, M. Makkee, G. Saracco and N. Russo, *Green Chem.*, 2017, **19**, 2326–2346.

228 Y. Chen, C. W. Li and M. W. Kanan, *J. Am. Chem. Soc.*, 2012, **134**, 19969–19972.
229 W. Zhu, R. Michalsky, O. n. Metin, H. Lv, S. Guo, C. J. Wright, X. Sun, A. A. Peterson and S. Sun, *J. Am. Chem. Soc.*, 2013, **135**, 16833–16836.
230 R. Wang, H. Haspel, A. Pustovarenko, A. Dikhtiarenko, A. Russkikh, G. Shterk, D. Osadchii, S. Ould-Chikh, M. Ma and W. A. Smith, *ACS Energy Lett.*, 2019, **4**, 2024–2031.
231 K. Sun, L. Wu, W. Qin, J. Zhou, Y. Hu, Z. Jiang, B. Shen and Z. Wang, *J. Mater. Chem. A*, 2016, **4**, 12616–12623.
232 M. Umeda, Y. Niitsuma, T. Horikawa, S. Matsuda and M. Osawa, *ACS Appl. Energy Mater.*, 2019, **3**, 1119–1127.
233 A. Klinkova, P. De Luna, C.-T. Dinh, O. Voznyy, E. M. Larin, E. Kumacheva and E. H. Sargent, *ACS Catal.*, 2016, **6**, 8115–8120.
234 W. Luo, J. Zhang, M. Li and A. Züttel, *ACS Catal.*, 2019, **9**, 3783–3791.
235 D. Ren, N. T. Wong, A. D. Handoko, Y. Huang and B. S. Yeo, *J. Phys. Chem. Lett.*, 2016, **7**, 20–24.
236 J. Chung, J. Koh, E.-H. Kim and S. I. Woo, *Phys. Chem. Chem. Phys.*, 2016, **18**, 6252–6258.
237 R. Reske, H. Mistry, F. Behafarid, B. R. Cuenya and P. Strasser, *J. Am. Chem. Soc.*, 2014, **136**, 6978–6986.
238 D. Raciti, K. J. Livi and C. Wang, *Nano Lett.*, 2015, **15**, 6829–6835.
239 H. S. Jeon, S. Kunze, F. Scholten and B. R. Cuenya, *ACS Catal.*, 2018, **8**, 531–535.
240 G. B. Damas, C. R. Miranda, R. Sgarbi, J. M. Portela, M. R. Camilo, F. H. Lima and C. M. Araujo, *Catalysts*, 2019, **9**, 636.
241 Z. Gu, H. Shen, L. Shang, X. Lv, L. Qian and G. Zheng, *Small Methods*, 2018, **2**, 1800121.
242 A. Bagger, W. Ju, A. S. Varela, P. Strasser and J. Rossmeisl, *ChemPhysChem*, 2017, **18**, 3266–3273.
243 D. Kim, C. S. Kley, Y. Li and P. Yang, *Proc. Natl. Acad. Sci. U. S. A.*, 2017, **114**, 10560–10565.
244 F. S. Roberts, K. P. Kuhl and A. Nilsson, *Angew. Chem.*, 2015, **127**, 5268–5271.
245 S. Min, X. Yang, A.-Y. Lu, C.-C. Tseng, M. N. Hedhili, L.-J. Li and K.-W. Huang, *Nano Energy*, 2016, **27**, 121–129.
246 J. Rudd, E. Kazimierska, L. B. Hamdy, O. Bain, S. Ahn, A. R. Barron and E. Andreoli, *Catalysis*, 2021, DOI: 10.26434/chemrxiv.12022623.v1.
247 A. Dutta, M. Rahaman, N. C. Luedi, M. Mohos and P. Broekmann, *ACS Catal.*, 2016, **6**, 3804–3814.
248 M. F. Alqahtani, K. P. Katuri, S. Bajracharya, Y. Yu, Z. Lai and P. E. Saikaly, *Adv. Funct. Mater.*, 2018, **28**, 1804860.
249 R. Schlögl, *Angew. Chem., Int. Ed.*, 2015, **54**, 3465–3520.
250 C. Costentin, M. Robert and J.-M. Savéant, *Chem. Soc. Rev.*, 2013, **42**, 2423–2436.
251 E. L. Clark, S. Ringe, M. Tang, A. Walton, C. Hahn, T. F. Jaramillo, K. Chan and A. T. Bell, *ACS Catal.*, 2019, **9**, 4006–4014.
252 H. Fujiwara, H. Hosokawa, K. Murakoshi, Y. Wada, S. Yanagida, T. Okada and H. Kobayashi, *J. Phys. Chem. B*, 1997, **101**, 8270–8278.
253 K. Klingan, T. Kottakkat, Z. P. Jovanov, S. Jiang, C. Pasquini, F. Scholten, P. Kubella, A. Bergmann, B. R. Cuenya and C. Roth, *ChemSusChem*, 2018, **11**, 3449–3459.
254 Y. Wang, J. Zhou, W. Lv, H. Fang and W. Wang, *Appl. Surf. Sci.*, 2016, **362**, 394–398.
255 J. Zeng, K. Bejtka, W. Ju, M. Castellino, A. Chiodoni, A. Sacco, M. A. Farkhondehfal, S. Hernández, D. Rentsch and C. Battaglia, *Appl. Catal., B*, 2018, **236**, 475–482.
256 Y. Gu, J. Li, L. Wang, M. Xie, X. Wu, F. Xie and M. P. Ryan, *ChemistrySelect*, 2019, **4**, 10995–11001.
257 R. F. Zarandi, B. Rezaei, H. S. Ghaziaskar and A. A. Ensafi, *J. Environ. Chem. Eng.*, 2019, **7**, 103141.
258 A. Dutta, M. Rahaman, M. Mohos, A. Zanetti and P. Broekmann, *ACS Catal.*, 2017, **7**, 5431–5437.
259 A. Dutta, M. Rahaman, B. Hecker, J. Drnec, K. Kiran, I. Z. Montiel, D. J. Weber, A. Zanetti, A. C. López and I. Martens, *J. Catal.*, 2020, **389**, 592–603.
260 B. C. Marepally, C. Ampelli, C. Genovese, F. Tavella, E. A. Quadrelli, S. Perathoner and G. Centi, *J. CO2 Util.*, 2020, **35**, 194–204.
261 J. Wang, J. Zou, X. Hu, S. Ning, X. Wang, X. Kang and S. Chen, *J. Mater. Chem. A*, 2019, **7**, 27514–27521.
262 X. Hou, Y. Cai, D. Zhang, L. Li, X. Zhang, Z. Zhu, L. Peng, Y. Liu and J. Qiao, *J. Mater. Chem. A*, 2019, **7**, 3197–3205.
263 Q. Li, M. Li, S. Zhang, X. Liu, X. Zhu, Q. Ge and H. Wang, *Catalysts*, 2019, **9**, 476.
264 X. Zhang, X. Sun, S.-X. Guo, A. M. Bond and J. Zhang, *Energy Environ. Sci.*, 2019, **12**, 1334–1340.
265 F. l. Urbain, P. Tang, N. M. Carretero, T. Andreu, J. Arbiol and J. R. Morante, *ACS Appl. Mater. Interfaces*, 2018, **10**, 43650–43660.
266 M. Rahaman, K. Kiran, I. Z. Montiel, V. Grozovski, A. Dutta and P. Broekmann, *Green Chem.*, 2020, **22**, 6497–6509.
267 T. Kottakkat, K. Klingan, S. Jiang, Z. P. Jovanov, V. H. Davies, G. A. El-Nagar, H. Dau and C. Roth, *ACS Appl. Mater. Interfaces*, 2019, **11**, 14734–14744.
268 H. Lee, S.-K. Kim and S. H. Ahn, *J. Ind. Eng. Chem.*, 2017, **54**, 218–225.
269 S. Ahn, K. Klyukin, R. J. Wakeham, J. A. Rudd, A. R. Lewis, S. Alexander, F. Carla, V. Alexandrov and E. Andreoli, *ACS Catal.*, 2018, **8**, 4132–4142.
270 J. Banhart, *Adv. Eng. Mater.*, 2013, **15**, 82–111.
271 J.-H. Han, M. Wang, P. Bai, F. R. Brushett and M. Z. Bazant, *Sci. Rep.*, 2016, **6**, 1–12.
272 A. Abdelfatah, Y. Reda, R. Abdel-Karim, S. M. El-Raghy and K. M. Zohdy, *Front. Mech. Eng.*, 2020, **6**, 35.
273 R. Mohammadi, L. Naderi and S. Shahrokhian, *J. Alloys Compd.*, 2019, **811**, 152016.
274 Y. Shi, L. Zhang, Y. Zhang, J. Li, Q. Fu, X. Zhu and Q. Liao, *Chem. Eng. J.*, 2021, **423**, 130339.
275 M. Rahaman, K. Kiran, I. Z. Montiel, A. Dutta and P. Broekmann, *ACS Appl. Mater. Interfaces*, 2021, **13**, 35677–35688.
276 M. Rahaman, V. Andrei, C. Pornrungroj, D. Wright, J. J. Baumberg and E. Reisner, *Energy Environ. Sci.*, 2020, **13**, 3536–3543.

